Potential for High Temperature-Aquifer Thermal Energy Storage(HT-ATES) in the Dutch subsurface

Using 2,5D subsurface models of the Netherlands to calculate recovery efficiency and visualise the spatial distribution of the economic potential for HT-ATES in specific aquifers

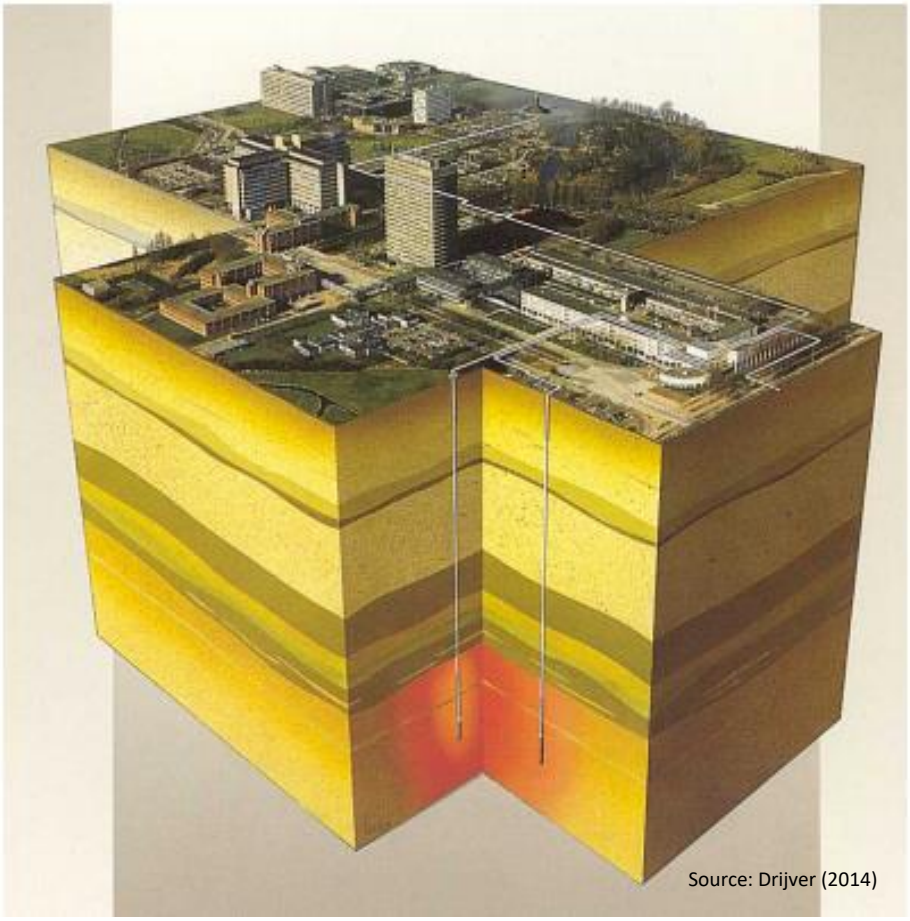

Source: Drijver (2014)

Master Thesis
Joris Tholen
Utrecht University,
Master Earth Structure and Dynamics
Student number: 3709876
24 October 2017

Supervisor UU: Fred Beekman
Supervisors TNO: Jan Diederik van Wees
Hans Veldkamp

Utrecht University

TNO innovation for life

ABSTRACT

High-temperature aquifer thermal energy storage (HT-ATES) involves seasonal storage of residual heat and is an important instrument in building an energy efficient future. HT-ATES could prove to be a better alternative than the lower enthalpy aquifer thermal energy storage (ATES), because it can be directly applied to a district heating network without using heat pumps. There is however a knowledge gap of the potential of HT-ATES in the Netherlands. This study aims to give a first-order approximation of the spatial distribution of this potential in specific aquifers, using a Java workflow. Using recently developed subsurface models of the Netherlands, it was possible to make probability maps of the economic potential of HT-ATES. A previous study by Pluymaekers et al. (2013) indicated certain shallow reservoirs within the North Sea super group to be of interest for HT-ATES. This study therefore assesses the potential in these aquifers, together with certain deeper aquifers.

By assuming a log-normal distribution and by generating a transmissivity distribution through Monte Carlo sampling, transmissivity maps with P10, P30, P50, P70 and P90 confidence levels are generated. To identify key parameters that influence the recovery efficiency and to find a computationally fast method for the approximation of these efficiencies, two faster analytical methods are compared with the numerical model DoubletCalc3D. The results indicated that the Rayleigh-based method (Schout et al., 2014) is the most accurate and computationally fast method, whereas the Radial Dupuit Interface Flow method (Bakker, 2009) delivered inadequate results.

The Rayleigh-based method is then implemented into the Java workflow to calculate the Coefficient of Performance (COP) of the HT-ATES system. The Excel workflow that was developed by Pluymaekers et al. (2013) is used to calculate the Levelised Cost of Energy (LCOE), where a LCOE <6 EUR/GJ marks an economic potential for HT-ATES, and higher values have less potential. The results indicated that the deeper aquifers (Delft Sandstone member, Rijnland group and Lower/Middle North Sea groups) have no potential, with some local exceptions, due to the low transmissivities and depth of the aquifers. The shallower reservoirs (Breda, Oosterhout and Maassluis formations) showed a high potential for HT-ATES, confirming the assessment done by Pluymeakers et al. (2013).

TABLE OF CONTENTS

List of Abbreviations

Symbol	Name	Unit
Capex	Capital expenditures	Euro
$C_{p,r}$	Specific heat capacity of rock	J kg^{-1} K^{-1}
$C_{p,w}$	Specific heat capacity of water	J kg^{-1} K^{-1}
$C_{v,r}$	Volumetric heat capacity of rock	J m^{-3} K^{-1}
$C_{v,w}$	Volumetric heat capacity of water	J m^{-3} K^{-1}
D	Dimensionless parameter in Bakker(2009) calculations	-
d_{well}	Well diameter	m or inch
f	Friction coefficient well	-
g	Gravitational acceleration	m s^{-2}
H	Thickness	m
k_h	Horizontal permeability	m^2 or D
K_h	Horizontal hydraulic conductivity	m s^{-1}
kH	Transmissivity	m^3 or Dm
k_v	Vertical permeability	m^2 or D
K_v	Vertical hydraulic conductivity	m s^{-1}
L_{well}	Distance between wells	m
Opex	Operational expenditures	Euro
P	Pressure	Pa or bar
Q	Flow rate	m^3 s^{-1}
Ra	Rayleigh number	-
Ra*	Modified Rayleigh number	-
Ra_c	Critical Rayleigh number	-
S	Salinity of the water	kg kg^{-1}
T	Temperature	°C
v	Stream velocity in well	m s^{-1}
V	Volume of water stored	m^3
v_{tip} and v_{toe}	Dimensionless radial velocities of tip and toe of the interface	-
z	Depth (positive w.r.t. the surface)	m
α	Thermal expansion coefficient	-
ε	Roughness inner tubing well	-
ε_{pump}	Efficiency of the pumps	%
ζ	Dimensionless vertical position of interface	-
μ	Viscosity	Pa s
μ_{eff}	Recovery efficiency HT-ATES	%
ρ_{fw}	Density of water at surface temperature and pressure	kg m^{-3}
ρ_r	Density of the rock	kg m^{-3}
$\rho_{w,ground}$	Density of the in situ groundwater at reservoir level	kg m^{-3}
$\rho_{w,inj}$	Density of injected water	kg m^{-3}
$\rho_{w,prod}$	Density of produced water	kg m^{-3}
σ	Dimensionless horizontal position of interface	-
φ	Porosity	-

1. INTRODUCTION

While there is a rising demand for sustainable energy sources and CO_2 emission reduction, the Dutch energy system still highly depends on fossil fuels (coal, oil and natural gas). With the goal set of reducing yearly greenhouse gas emissions with 20% by the year 2020 with respect to the emissions in 1990 (Paris Agreement, 2015), a transition to more sustainable and renewable energy sources needs to be made. CO_2 equivalent emissions in the Netherlands in 1990 are measured at 162.9 Mton, while the emissions in 2015 where 165.4 Mton (Central Bureau for Statistics, 2017). These numbers are based upon international guidelines for calculating global emissions (IPCC). It is globally recognized that there is a high urgency to mitigate the emission of greenhouse gases. Moreover, natural gas reserves in the Netherlands are decreasing (Central Bureau for Statistics, 2016) and societal issues arise from the earthquakes that are induced by the gas production in Groningen. The Netherlands is trying to make the transition to a more sustainable solution. In the past few years, major investments have been made in wind and solar power. Geothermal energy has also obtained more interest. Geothermal energy is obtained by drilling into a deep (hot) permeable aquifer and use the heat of the aquifer to warm up water to temperatures between 100 and 200°C. This hot water can then be used to be directly applied to district heating networks using heat exchangers. The Dutch Institute for Applied Geosciences (TNO) has developed a software (ThermoGIS, available on http://thermogis.nl/thermogis.html) which enables companies or individuals that have an interest in geothermal energy to make a first order approximation of the potential of a geothermal doublet for their specific business case.

The demand of energy can change on an hourly basis, a weekly basis and on a monthly basis. The reasons for these changes differ when a different timescale is applied. An hourly change could be caused by night time and day time, a weekly change could be caused by a change in weather and a monthly change is mostly caused by the change of season and the intensity of this change. Due to the higher average atmospheric temperatures in the summer the demand of heating is quite low, while in the winter the cold temperatures cause a household to use more energy for heating. An example of this is given in Fig. 1, where the supply of energy from a geothermal doublet exceeds the demand in the summer and is far below the demand during the winter weeks. This study assumes a constant supply of energy from a geothermal well to describe the base load from which the residual energy is extracted. The residual energy that is not used in the summer is partially emitted into the atmosphere. In order to improve the energy efficiency, an energy storage system can be used for this emitted residual energy

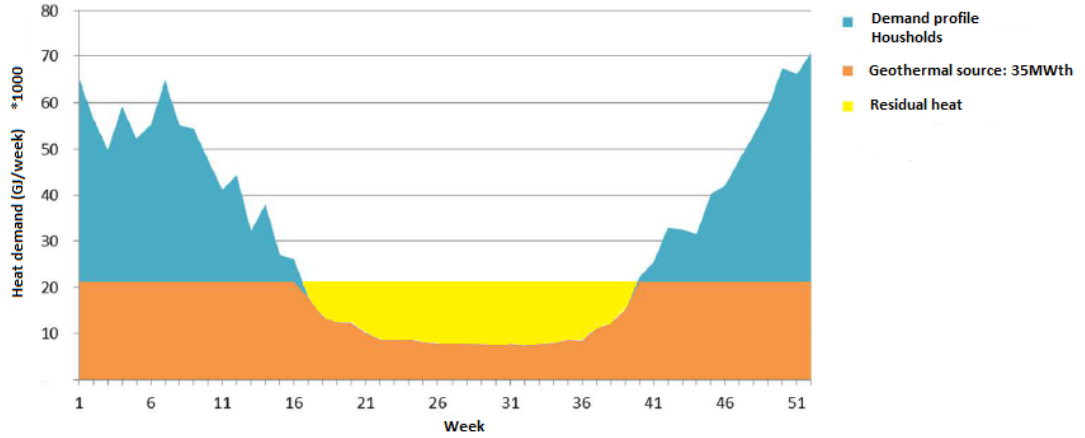

Fig. 1: Example of a demand supply profile with a constant base load production of energy from a geothermal doublet. The yellow color indicates the residual heat that can be stored during the summer weeks (Kalkman et al., 2016).

The number of underground thermal energy storage (UTES) systems has increased rapidly over the last decade (Bonte et al., 2011). UTES systems are used for cooling and heating purposes, where in the Netherlands two types are used: open and closed systems. The closed system is called Borehole Thermal Energy storage (BTES), where water is pumped through plastic conductor pipes. The open system is called Aquifer Thermal Energy Storage (ATES), where groundwater is used to store heat in aquifers. Heat is extracted from the atmosphere in the summer and injected into the aquifer while cold water is extracted to cool buildings. The stored heat is then produced from the reservoir during winter while cold water is injected. These systems mostly use one or more extraction and injection wells to circulate the groundwater. The net volume flow through the aquifer is therefore zero. The Netherlands as a delta system has many large sandstone reservoirs that could be used for such an open storage system.

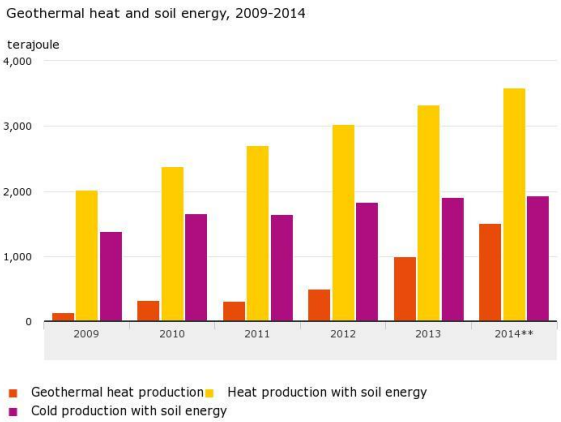

Fig. 2: Geothermal heat production and shallow ATES cold/heat production from 2009-2014 (CBS, 2015).

Fig. 2 from the Central Bureau of Statistics (2015) shows that there has been a large increase in those ATES systems in the recent years and heat production by geothermal energy has doubled in the period from the year 2009 to 2014. The efficiency of those ATES systems is relatively high. Sommer et al. (2012) showed in a study that if the ATES system is influenced by groundwater flow, the recovery efficiency could be below 50%. Another study by Bakr et al. (2013) shows that if the ATES is in a homogeneous aquifer, the recovery efficiency is between 68% and 87%, for year 1 and year 10 of production respectively. The amount of heat that can be stored in those systems is however small, because the injection temperatures for warm and cold storage are 13 °C–25 °C or cool water 6 °C–12 °C (Bakr et al., 2013). To be able to use this heat for e.g. heating a household, a heat exchanger is needed that increases the water temperature from 25 °C to at least 45 °C. This heat exchanger does need electricity to work, resulting in high capital and maintenance costs.

A solution is to inject water of higher temperatures, where the production temperatures after storage are still high enough to be directly applicable for heating of households (>60 °C). This storage system is called High Temperature Aquifer Thermal Energy Storage(HT-ATES). HT-ATES systems are however not widely implemented due to the many operational problems that exists (Drijver, 2011), including: large heat losses, clogging of the wells by dissolution of minerals and corrosion of several components in the entire ground water system (Sanner et al., 1999; Drijver, 2011). The effects of clogging and corrosion are not examined in this study, because Drijver (2011) demonstrated that the effects of clogging are relatively low on the efficiency of the system and the impact of corrosion of the reservoir is relatively small. Major problems can be avoided when monitoring of the trace elements, used for monitoring clogging, in the aquifer is done correctly. However the largest problems are the effects of heat losses due to conduction, convection and diffusion in the aquifer. Due to the larger differences in density within a HT-ATES system, hot water flows to the top of the

reservoir and through conductive heat loss into the confining layers the recovery efficiency decreases.

A previous study on the potential of HT-ATES in the Netherlands, done by Pluymaekers et al. (2013), highlighted certain reservoirs and areas of interest for HT-ATES. These reservoirs are expected to indicate a high potential for HT-ATES. In this report the results of a study are presented in which:

- Three different methods, for calculating recovery efficiency, are used in a sensitivity study on the influence of several reservoir properties and engineering parameters.
- The three methods are compared and the most accurate method is used in the Java workflow.
- A first order assessment of the potential for HT-ATES in the Netherlands is done, by rewriting an Excel workflow, made by Pluymaekers et al. (2013) for ATES systems, into Java to calculate the economic performance from subsurface models of the Netherlands.

2. GEOLOGICAL SETTING

2.1 BRIEF GEOLOGICAL HISTORY OF THE NETHERLANDS

De Jager (2007) describes three main plate-tectonic events which had the most influence on the structure of the subsurface of the Netherlands:

1. The assembly of the supercontinent Pangea during the Paleozoic (~335 Ma) that resulted in the Caledonian and Variscan orogens .
2. The break-up of Pangea during the Mesozoic (~175 Ma) that resulted in the formation of rift basins.
3. The Alpine collision of Europe and Africa during the Late Cretaceous to Early Cenozoic (100.5-23.03 Ma) that accompanied the inversion of rift basins and reactivation of pre-existing extensional faults.

Fig. 3 shows the lithostratigraphy of the Netherlands that is described below.

The geological history of the Netherlands starts during the Silurian age (443.8-419.2 Ma). These rocks are Caledonian metamorphic basement, situated at roughly 10 km depth (de Jager, 2007; Geluk et al., 2007). The location of basins, platforms and highs changed over time, due to the tectonic processes that followed the interaction of lithospheric plates. During the Caledonian Orogeny, the resulting horst and graben topography controlled deposition of fluvial and basinal deposits. Early Carboniferous (358.9 Ma) a widespread carbonate platform formed in the middle and southern Netherlands (Geluk et al., 2007). On top of these Carboniferous rocks lies a 5500 m thick sequence of Silesian (326.4-299.0 Ma) rocks. This sequence comprises mainly siliclastic sediments that range from claystone, siltstone and sandstone up to conglomerate. During Early and Middle Silesian, peat was deeply buried, resulting in coal layers (Van Buggenum & Den Hartog Jager, 2007). The Permian (289.9-252.17 Ma) deposits in the Netherlands consist of the Lower Rotliegend, Upper Rotliegend and Zechstein groups, where the Lower Rotliegend group consists of volcanic and clastic rocks. The Upper Rotliegend group consists of predominantly sandstones in the onshore of the Netherlands. The Zechstein group consists of marine evaporates and carbonates (Geluk , 2007a).

The Triassic (252.17-201.3 Ma) rocks are separated by two unconformities that are a result of the rift tectonics, initiated due to the break-up of Pangea. The Lower Germanic Trias group consists of fine-

grained siliclastic deposits with sandstone and oolites. The Upper Germanic Trias group consists of lacustrine, brackish-water and marine, fine-grained siliciclastics, carbonates and evaporates (Geluk, 2007a). During the beginning of the Jurassic (201.3-163.5 Ma), the Netherlands was in a pre-rift phase where mostly clay stones and marine sediments were deposited. During Upper Jurassic (163.5-145 Ma) three different stratigraphic groups were formed, representing syn-rift deposits in three different basins: one marine, one continental and one continental that was restricted to marine (Wong, 2007). During Lower Cretaceous (145-100.5 Ma) the rifting tectonics that controlled deposition during Jurassic was followed by post-rift into regional subsidence, creating mainly marine conditions throughout the Cretaceous period. The Lower Cretaceous Rijnland group comprises of mainly clayish formations with sandstone beds at the base of the formations. The Upper Cretaceous Chalk group consists of limestones and marls that were deposited during a calm period of sedimentation (Herngreen & Wong, 2007).

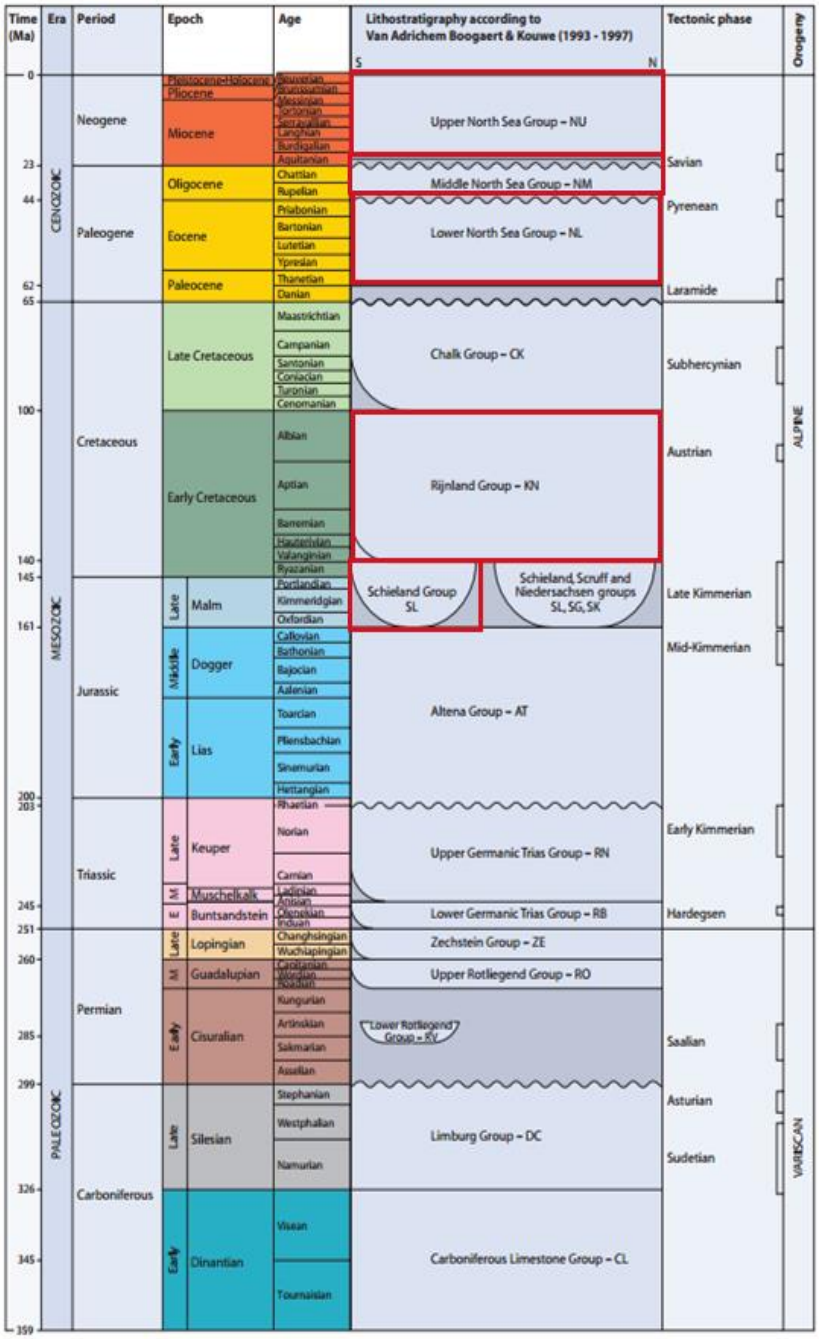

Fig. 3: Figure of the lithostratigraphy of the Netherlands with the corresponding tectonic events by Duin et al. (2006). Red indicates the potential reservoirs that are evaluated in this study.

Since Late Cretaceous the compression from the Alpine orogeny caused uplift followed by the development of a major rift zone (Rhine Graben system). Wong et al. (2007) describes that during Paleocene and Eocene times (66-33.9 Ma) sandstones, marls and clays where deposited. This sequence is called the Lower North Sea group. Due to tectonic movements and erosion, in the Early Oligocene (33.9 Ma), an unconformity was formed that marks the boundary between the Lower and Middle North Sea groups. The Middle North Sea group mainly comprises sand-, silt- and clay stones of Oligocene age. A tectonic event caused by the continuing Alpine Orogeny during the Early Miocene (23.03 Ma) resulted in another unconformity that marks the boundary between the Middle and Upper North Sea groups. The Upper North Sea group is comprised of clay stones, fine to coarse-grained sandstones, gravel and coal seams and is of Neogene to Quarternary age (23.03 Ma-present).

2.2 STRATIGRAPHY OF POTENTIAL HT-ATES RESERVOIRS

For the selection of potential reservoirs that can be used for HT-ATES, several criteria are assumed. First the aquifer must exist within the depth interval of 0-1500 m, because drilling cost will be too high for deeper aquifers. Secondly the aquifer needs to be at least 20 m thick and the transmissivity of the aquifer needs to be at least 100 Dm. The reasoning for these specific values is arbitrary, however the main purpose is to reduce computational time and to prevent calculations to be done on reservoirs with little prospect.

ThermoGIS v1.1 gives hydrogeological information on the subdivisions of the North Sea supergroup as a whole (including the Middle and Lower North Sea groups). The Rijnland group and the Delft Sandstone member are also partly present in the shallow subsurface and are therefore presented below together with the North Sea group, in the evaluation of potential reservoirs. Pluymaekers et al. (2013) suggests the following aquifers to be most suited in the shallow depth interval for HT-ATES: Maassluis, Oosterhout and Breda formations (see Fig. 4). These formations are all part of the Upper North Sea group and consist mainly of marine deposits of Miocene to Lower Pleistocene age (23.03-0.781 Ma). It is also suggested that the Voort member, which is a Middle North Sea group member, has a good potential. Because of lack of data on the hydrogeology of the Voort member and the other deeper members that are indicated in Fig. 4, these are not evaluated individually in this study.

The nomenclature of all the reservoirs are listed in Appendix C. Appendix D shows a map that lists the structural elements that describe the distribution of the members in the sections below. The permeability values that are mentioned in the sections below are retrieved from the REGISII v2.2 and ThermoGIS databases. The mean values are calculated with ArcMap 10.

2.2.1 Delft Sandstone Member (Jurassic)

The Delft Sandstone Member (SLDND) is part of the Nieuwerkerk Formation in the Schieland group. It is a massive fining upward sandstone sequence that is overlain by the clay stones of the Rodenrijs Member (Boogaert & Kouwe, 1993-1997). It is the deepest reservoir that is considered in this study with depth ranging between 600 and 2700 m and thickness ranging between 0 and 276 m. Groenenberg et al. (2010) describes the lower part of the SLDND to consist of poorly lateral and vertical connected fluvial sandstone bodies, while in the upper part connectivity is high with an porosity of 30% and permeabilities between 725 and 1130 mD.

2.2.2 Rijnland Group (Lower Cretaceous)

The Rijnland group (KN) is subdivided in three different formations: the Vlieland Sandstone Formation, the Vlieland Claystone Formation and the Holland Formation. The Vlieland Claystone Formation is not suited as a reservoir and is therefore not evaluated further. The Vlieland Sandstone Formation mainly consists of several sandstone members with some sand-claystone members and overlies sediments of the Schieland and Scruff groups (Boogaert & Kouwe, 1993). The Holland Formation overlies the Vlieland Claystone Formation and is mainly a sequence of marls and marly claystones, however some incursions of greensands can be found. The lithology of the individual potential sandstone members is described below.

Rijswijk Member (KNNSR)
The Rijswijk member consists of sandstones with a very fine to medium grain size, with locally occurring mica beds, lignitic claystone beds and siderite concretions (NAM and RGD, 1980). It is distributed over the West Netherlands Basin with depths ranging between 487-2620 m and thicknesses between 1-231 m. The permeabilities in the reservoir are on average around 455 mD.

Berkel Sandstone Member (KNNSB)
The Berkel Sandstone Member is a very fine to fine and medium to coarse grained sandstone sequence, with locally occurring calcareous cemented beds and claystone beds. It shows high and low angle cross bedding and horizontal bedding. It is distributed mainly over the southern margin of the West Netherlands Basin (Nam and RGD, 1980). The sequence has depths ranging between 504-2562 m and thicknesses between 1-220 m. The mean permeability is 256 mD.

IJsselmonde Sandstone Member(KNNSY)
The IJsselmonde Sandstone member contains very fine to medium grained sandstone beds, with locally occurring calcareous cemented beds and thin intercalated claystone beds. It can be found in the south eastern West Netherlands Basin, near Rotterdam(Nam and RGD, 1980). The sequence has depths ranging between 558-2476 m and thicknesses between 1-144 m. The average permeability is 246 mD.

De Lier Member (KNNSL)
The De Lier member is an sequence with an alternation of thin-bedded, very fine to fine grained argillaceous sandstones and sandy clay stones. It is distributed over the southern margin of the West Netherlands Basin (Nam and RGD, 1980). The sequence depth ranges between 561-2374 m with thicknesses between 1-167 m. The mean permeability of the reservoir is 75 mD.

Bentheim Sandstone Member (KNNSP)
The Bentheim Sandstone member is a sequence fine to medium grained calcareous sandstone beds. It can be found in the Dutch Lower Saxony Basin in the eastern parts of the provinces Drenthe and Overrijssel (Boogaert & Kouwe, 1993-1997). Its depth ranges between 42-2209 m and thickness between 1-69 m. It has a mean permeability of around 185 mD.

Gildehaus Sandstone Member (KNNSG)
The Gildehaus Sandstone Member sequence consists mainly of coarse-grained conglomeratic sandstones with pebbles of quartz, sandstone and limestone. It can contain clay flakes, clay-ironstones and coals and in some localities it has a high content of calcareous cement. It is distribution is restricted to the southern Dutch Lower Saxony Basin (Boogaert & Kouwe, 1993-1997). The depth of the sequence ranges between 37-2098 m and thickness between 1-112 m. The mean permeability of this sequence is around 36 mD.

Friesland Member (KNNSF)

The Friesland member contains fine to medium grained sandstones that can locally grade into conglomeratic sandstones. It can be found in several basins in the Netherlands: Vlieland Basin, southern Dutch Central Graben, Terschelling Basin, edges of the Lower Saxony Basin, Friesland Platform, Groningen High, Noord-Holland Platform/ Central Netherlands Basin and the Texel-IJsselmeer High (Boogaert & Kouwe, 1993-1997). The depth of the sequence range between 215-2778 m with thicknesses between 1-191 m. The mean permeability of the entire sequence is 7 mD.

Holland Greensand Member (KNGLG)
The Holland Greensand member consists of very fine to fine grained sandstones with locally siltstones and clay stones. Its distribution is restricted to the southern West Netherlands Basin and eastern Broad Fourteen Basin (Boogaert & Kouwe, 1993-1997). The depth of the sequence ranges between 35-2958 m with thicknesses between 1-123 m. The mean permeability is 23 mD.

2.2.3 Lower North Sea Group

The Lower North Sea group consists of alternating sandstone and clay members, which lie on top of the Upper Cretaceous Chalk group. The group was formed in a marine environment. It is divided into two formations: the Dongen Formation and the Landen Formation. See Fig. 4 for an overview of the lithostratigraphy of the Lower, Middle and Upper North Sea groups.

Swalmen Member (NLLFL)
The Swalmen Member contains an alternation of thin sand layers, clay layers and in the upper parts coal beds. It can be found in the province of Limburg and the very eastern part of Noord-Brabant, as well as in south eastern Flevoland and northern Gelderland (Boogaert & Kouwe, 1993-1997). The depth of the sequence ranges between 231-1841 m and thicknesses between 1-59 m. The mean permeability of the sequence is 381 mD.

Heers Member (NLLFS)
The Heers member consists of very fine grained calcareous sandstones with intercalated clay stone beds. It can be found in the Roer Valley Graben extending into the provinces Noord-Brabant, Limburg and Gelderland. It can also be found in northern Gelderland, the IJsselmeer, northern Noord-Holland and the western parts of the Waddenzee and Friesland (Boogaert & Kouwe, 1993-1997). Its depth ranges between 195-1830 m with thicknesses between 1-44 m. The mean permeability is around 393 mD.

Reusel Member (NLLFR)
The Reusel member consists of up to three coarsening up-ward sequences. While the basal sequence contains an alternation of siltstone and shale layers, the upper sequences have more sandier layers with clean sandstone at the top. The member is only present in and near the Roer Valley Graben in Noord-Brabant and Limburg (Boogaert & Kouwe, 1993-1997). The depth of the sequences range between 311-1704 m and thickness between 1-84 m. The mean permeability of the sequence is 332 mD.

Basal Dongen Sand Member (NLFFD)
The Basal Dongen Sand member is mainly defined as a thin fining-upward sandstone, while in some parts sand bodies are separated by clay stone beds. The member is distributed over the southern and central parts of the Netherlands, mainly in Noord-Brabant, Zuid-Holland and Zeeland (Boogaert & Kouwe, 1993-1997). Its depth ranges between 239-1308 m and thickness between 1-102 m. The mean permeability of the member is very high at 700 mD.

2.2.4 Middle North Sea Group

The group mainly consists of sands, silts and clays of a marine origin. The group is divided into three different formations. Only certain members from the Veldhoven Formation and the Rupel Formation are evaluated, because there is not enough data on the Tongeren Formation.

Vessem Member (NMRFV)
The Vessem member consists of mainly thick sandstone deposits with some intercalated claystone beds. It is distributed mainly in and around the Roer Valley Graben (Boogaert & Kouwe, 1993-1997). The depth of the member ranges between 98-1650 m with thicknesses between 1-139 m. The mean permeability of the member is around 615 mD.

Steensel Member (NMRFT)
The Steensel member comprises an alternation of (silty) clay stones with thin sandstone layers. The distribution of this member is restricted to the Roer Valley Graben and the south eastern part of the Zuiderzee Low. Its depth ranges between 282-1642 m and thickness between 1-92 m. The mean permeability is low, with respect to the Vessem member, at a value of 280 mD.

Voort Member (NMVFV)
The Voort member comprises a thick stack of coarsening upward sequences of sandstones with small portions of clays in between. The member is centred around the Roer Valley Graben in the south eastern part of the Netherlands. The depth ranges between 228-1514 m and thickness between 1-295 m. The mean permeability of the member is 532 mD.

2.2.5 Upper North Sea Group

The Upper North Sea group comprises clay stones, fine to coarse grained sandstones and locally some gravel and peat or brown coal seams (Wong et al., 2007). From the many lithostratigraphic formations that are defined by Boogaert and Kouwe (1993-1997), only the Breda Formation, Oosterhout Formation and Maassluis Formation are considered potential reservoirs (Pluymaekers et al., 2013). The formations are all subdivided into smaller units by Vernes et al. (2005). For these smaller units the following nomenclature is used: the z stands for sandstone, the k stands for clay stone and the c stands for complex unit (see Appendix C). The description of a complex unit is used when a frequent complex alternation of thin sand- and clay stone beds makes it too difficult to map. Note that in every sandstone member insignificantly small claystone beds can be found.

Breda Formation (BR)
The Breda formation is a marine deposition that contains a complex alternation of glauconitic very fine to fine grained sandstones and sandy to silty clay stones (Wong et al, 2007; Westerhoff, 2003). From top to bottom the individual units of the formation are: BRZ1, BRK1, BRZ2, BRZ3 and BRZ4. While the BRZ1 unit is distributed over a large area that covers Zeeland, Noord-Brabant, northern Limburg, Gelderland and eastern Utrecht; the BRZ2 to BRZ4 units on the other hand can only be found locally in the central part of Limburg. The BRZ1 can reach thicknesses of 900 m in the Roer Valley Graben.

Oosterhout Formation (OO)
The Oosterhout Formation consists of alternations of very fine to very coarse sandstones and sandy to silty clay stones. It is also characterised by the occurrence of sandstone beds rich with mollusc shells and bryozoans (Wong et al., 2007; Ebbing & De Lang, 2003). The individual units that are defined by Vernes et al. (2005) are from top to bottom: OOZ1, OOZ2 and OOC. The Oosterhout Formation is distributed over the most of the onshore Netherlands, except for the south east, south west and the most eastern parts of the Netherlands. The thickest unit is the OOC, which reaches a thickness of 283 m in the Waddenzee.

Maassluis Formation (MS)

The Maassluis Formation contains very fine to coarse-grained shell bearing sandstones and sandy to silty clay stones (De Gans, 2007; Huizer & Weerts, 2003). The individual units are from top to bottom: MSZ1, MSK1, MSZ2, MSK2, MSZ3, MSC and MSZ4. Its distribution covers the entire western and central part of the Netherlands. The thickness of all units strongly variates over it distribution area, where MSC reaches the largest thickness of 142 near the island Terschelling.

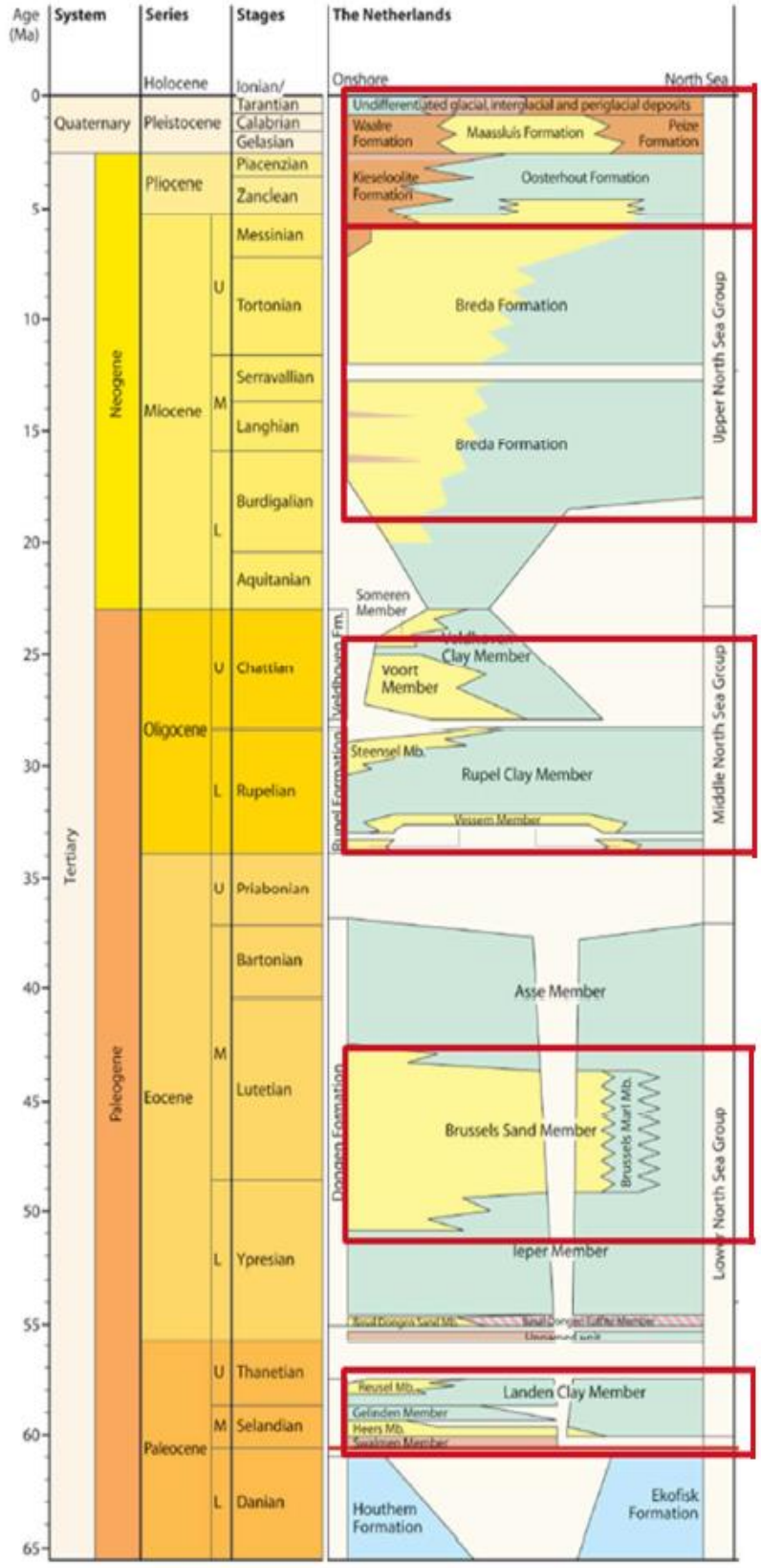

Fig. 4: Figure of the Lithostratigraphy of the North Sea super Group, from Pluymaekers et al. (2013). The red squares indicate the potential aquifers that are suggested by Pluymaekers et al. (2013).

3 METHODS

3.1 JAVA MODEL SETUP

The setup of the proposed automated Java workflow is as follows(see Fig. 5). The first step is uploading the 2.5D subsurface models of the aquifers into grids in the Java code. From these grids the permeability, depth, thickness and standard deviations are iterated over the coordinate points and read. For different probabilities the transmissivity is then calculated (see section 3.3.3). For every coordinate in the grid of a certain reservoir, using transmissivity, depth and thickness, the efficiency and economic feasibility of a possible HT-ATES system are calculated (see section 3.5). The results from these calculations in the Java code are then written in 2D ASCII grids that can be visualized in a viewing software, e.g. ArcMap.

In order to simplify the calculations in the Java workflow, it is assumed that the input values for each specified reservoir are spatially homogeneous.

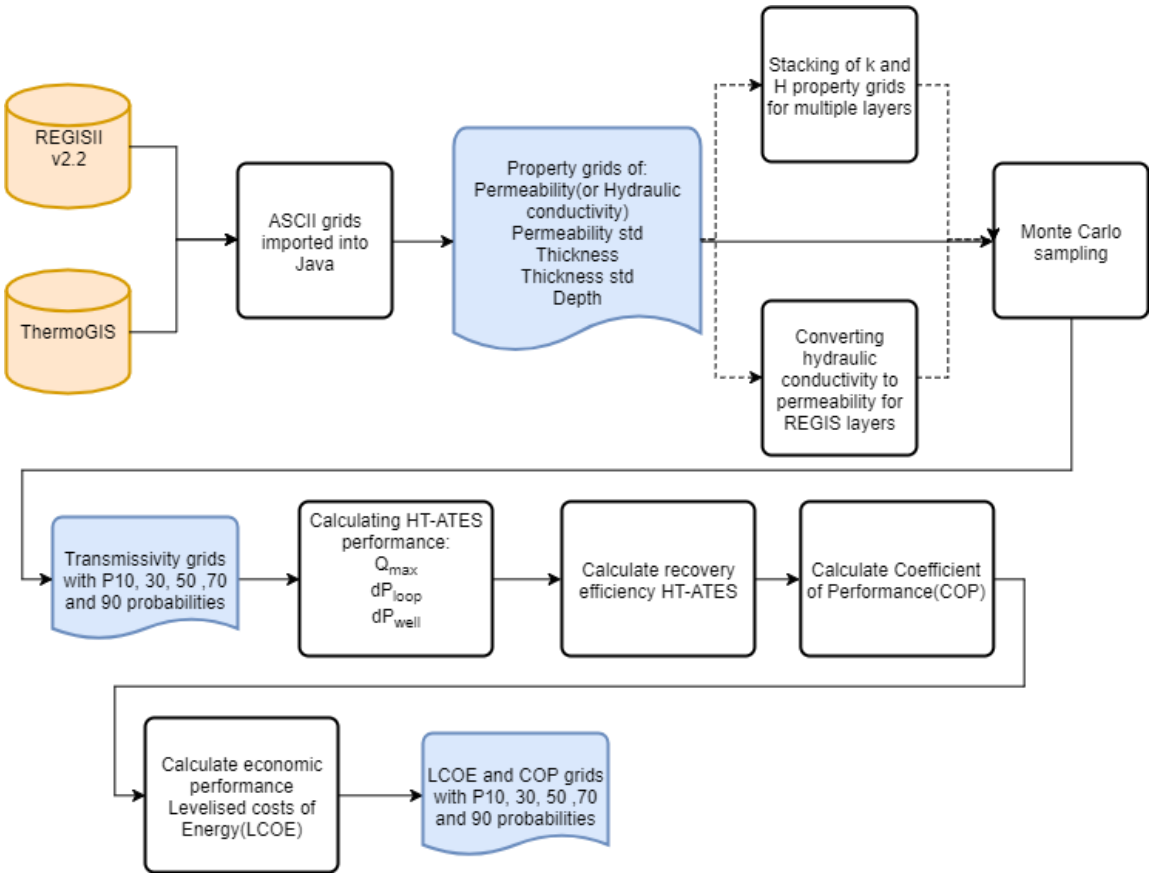

Fig. 5: Workflow diagram showing the input, processes and output of the Java model setup. The orange bins at the start represent the input databases, The white boxes represent processes and calculations done in Java and the blue boxes represent output grids. The dashed lines represent two possible scenarios where stacking is done ore when an intermediate step has to be made to convert to permeability(only for REGIS layers).

3.2 SUBSURFACE MODELS OF THE NETHERLANDS

There are a number of subsurface models of the Netherlands such as: the digital geological model (DGM) , the Regional Geohydrological Information System (REGIS), the hydrogeological model (GeoTOP) and the digital geological model (DGMdeep). These models mostly are made for a specific

depth interval of the subsurface. DGM, REGIS and GeoTOP are high resolution models of the shallow subsurface (0-500m depth), whereas DGMdiep is a low(er) resolution model that includes the deeper subsurface (0-5000m). All data is publicly accessible on the portal of Digital Information of the Dutch Subsurface (www.dinoloket.nl) and the portal of Dutch Oil and Gas Data (www.nlog.nl). For the purpose of this study, subsurface data from REGIS II v2.2 (based upon DGM) and ThermoGIS (based upon DGMdeep) databases are used to calculate the potential of HT-ATES in the Netherlands.

REGIS II v2.2 is the most recent hydrogeological model of the shallow subsurface. Approximately 16,500 onshore boreholes, seismic data of fault structures and additional data from hydrogeological data such as groundwater heads and pumping tests are used to create REGIS II v2.2 from the DGM model (Gunnink et al., 2013). This data is then interpolated, using a block-kriging technique (Isaaks & Srivastava, 1989; Goovaerts, 1997) to obtain the best surface fitting the data from the seismic and borehole data. The interpolation procedure was adapted for each different lithological unit. Gunnink et al. (2013) interpolated the base of the unit, rather than the top, because the top can be a result of more recent geological processes while the base is assumed to represent the circumstances at time of deposition. They also incorporated fault surfaces, because they define units that need to be handled separately. Uncertainties in the trend surfaces that are caused by inconstancies in the interpolation technique, are quantified by using a cross-validation to estimate the difference between the true value of the unit surface at each borehole and the estimated value that results from the interpolation. A moving window is then applied to expand the uncertainties from the borehole locations to the entire area of the unit (Gunnink et al., 2010).

The REGIS II v2.2 database contains ASCII grids (2,5D), with a grid cell size of 100x100 m, for different layers of the subsurface. These ASCII grids contain values for the depth of the top and base of the layer (z_{top} and z_{base}), thickness (H), horizontal and vertical hydraulic conductivity (K_h and K_v), standard deviations for the measurements of the hydraulic conductivities ($K_{h,\,std}$ and $K_{v,\,std}$) and hydraulic resistance. Vernes et al. (2005) describe the methods used to create the hydrogeological units in REGIS II v2.2. They used interpreted core sample descriptions, hydraulic conductivity measurements from undisturbed samples and statistics for hydraulic conductivities [m/s] and porosities of sediments to interpolate the values onto the entire area of the unit. The standard deviations of the hydraulic conductivities were measured at drilling locations and interpolated over the unit area. The thicknesses of the layers are assumed to have a neglectable uncertainty. The hydraulic conductivities (K) in m/s are converted to permeabilities (k) in m^2 or D by using Eq. 1, because the calculations that are used by this study describe permeability in mD or in m^2. In this equation μ is the viscosity of the injected water [Pa·s], ρ is the density of the injected water [$kg \cdot m^{-3}$] and g is the gravitational acceleration [$m \cdot s^{-2}$].

$$k = K\frac{\mu}{\rho g} \qquad \text{Eq. 1}$$

ThermoGIS v1.1 (2012) is the most recent model of geothermal potential in the deeper subsurface. The database contains ASCII grids with a grid cell size of 250x250 m. It is originally designed for the potential assessment of geothermal energy in the Netherlands. The model is geometrically based upon 3D models of the subsurface made by TNO with data from approximately 5,000 wells, 72,000 km of seismic data and 150,000 core plug measurements of permeability (van Wees et al., 2010; Pluymaekers et al., 2012). An overview of this data is shown in Fig. 6.

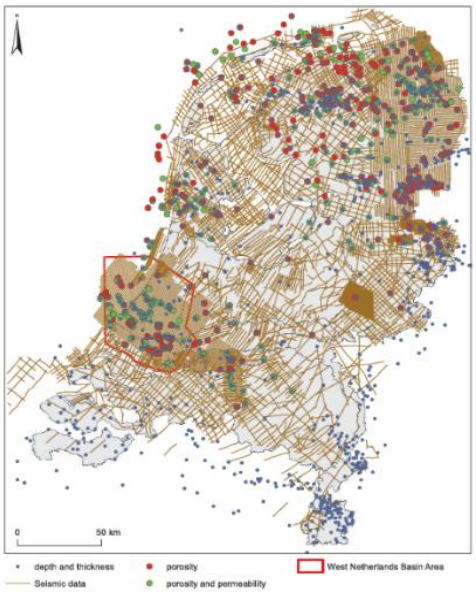

Fig. 6: Seismic coverage and wells used for the reservoir characterisation in ThermoGIS (Pluymaekers et al., 2012).

The depth of the horizons mostly defined from seismic data. The horizons that are not visible on the seismic data and the properties of the layers are calibrated at well locations and the areas that surround the well location, by using a kriged correction grid that is based upon the misfit between well core information on depth of aquifers and the horizons that are interpolated using a Kriging method(Pluymaekers et al., 2012). Kriging is an interpolation method where a distance-weighted average of known data points is used to interpolate values between the known data points (Knotters et al., 1995; Wu et al., 2005). Uncertainty has not been taken into account in the mapping of the depth of the reservoirs, while uncertainty in thickness has been calculated from geostatistical analyses of the thicknesses in the wells.

Pluymaekers et al. (2012) describe the workflow, as can be seen in Fig. 7, that is used in the model ThermoGIS for mapping transmissivity. The first step is using petrophysical analyses from well porosity logs and neutron logs to calculate the average porosities and permeabilities of the specific aquifers from core plug measurements. The second step is to use collocated co-kriging to interpolate porosity values between data points using maximum burial depth. The third step utilizes a linear regression relationship between the logarithmic average permeability and the porosity to create a permeability trend map (Eq. 2). The constants *a* and *b* represent the intercept and slope of the trend line and the porosity is denoted by φ and permeability in Darcy units is by *k*.

$$\ln k_{average} = a + b \cdot \varphi_{average} \qquad \text{Eq. 2}$$

Because there is a misfit between the trend permeability map and the $k_{average}$ values that are obtained from well data, a second permeability map is created in the fourth step. A trend kriging method is used by Pluymaekers et al. (2012) to interpolate the residual values of the well data and the predicted values from the permeability trend map to honour the data points and follow the trend when no data is available. The resulting permeability map (showing k) also contains uncertainties in the form of standard deviations from the plotted values that are obtained during the trend kriging method, assuming a lognormal distribution of k and the error on k.

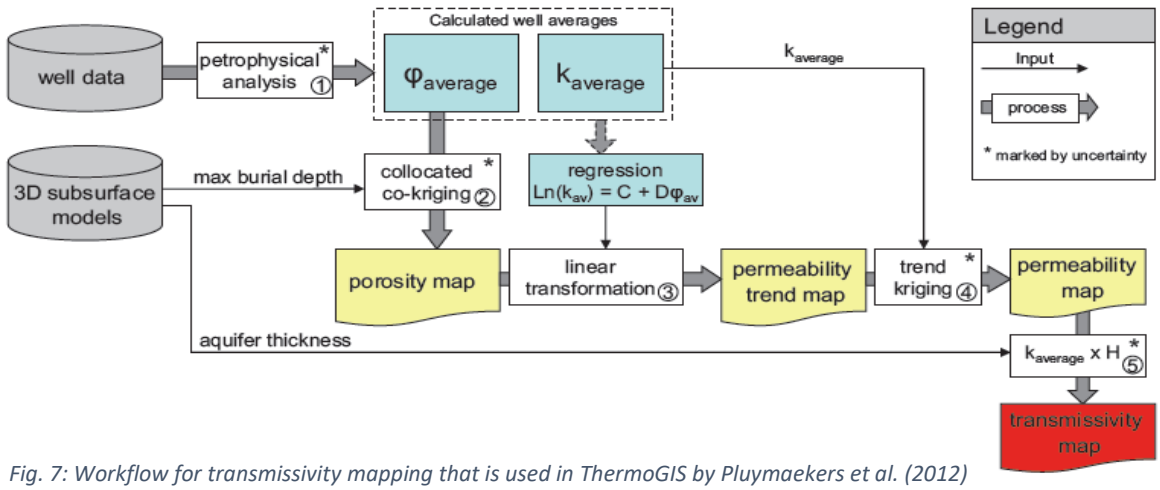

Fig. 7: Workflow for transmissivity mapping that is used in ThermoGIS by Pluymaekers et al. (2012)

3.3 THEORETICAL FRAMEWORK

3.3.1 Geophysical assumptions

In order to limit the runtime of the Java workflow, certain assumptions are made. The first assumption is that there is a constant thermal gradient in the Netherlands. Bonte et al. (2012) used a dataset of 1293 values from 454 wells to model the spatial variability of temperature in the subsurface of the Netherlands. The average thermal gradient of this model is 31.3 °C km^{-1} with a surface temperature of 10.1 °C. A similar thermal gradient is adopted in this study where temperature with depth is 31°C km^{-1} with a surface temperature of 10°C.

The second assumption is that the salinity of the injected water and the in-situ groundwater is constant at 10,000 ppm (0.01 kg/kg respectively). The third assumption of the model is that the rock density (ρ_r), used to calculate recovery efficiency, is constant with depth and temperature variations. It is assumed to be 2,500 kg m^{-3} for a sandstone reservoir with a porosity (φ) of 0.3. The third assumption is that the pressure increases linearly with depth. The pressure gradient is therefore defined at 0.01 MPa/m. All the parameters that are used in the model are listed in Table 2.

3.3.2 Temperature dependent viscosity, density and heat capacity

Viscosity is a measure of the internal resistance to deformation of fluids by external shear stress or tensile stress and is used in this study to calculate flow in a porous medium. While viscosity of fluids decreases rapidly with temperature, it is minimally effected by pressure. Salinity increases the viscosity of the fluid. Batzle and Wang (1992) approximated viscosities of a fluid in a porous reservoir, whilst neglecting pressure effects (see Eq. 3). Where *S* [kg/kg] is the salinity of the fluid in and *T* [°C] is the temperature of the fluid.

The density of the injected water and ambient groundwater is assumed to be temperature and pressure dependent. A fluid when heated undergoes a volumetric expansion, which is proportional to a density decrease. The inverse happens when the pressure is increased. Batzle and Wang (1992) also derived an equation to calculate the density of sodium chloride solutions with variations in salinity, temperature and pressure (see Eq. 4 & Eq. 5). These equations are implemented by van Wees et al. (2012) in the ThermoGIS model.

Because the enthalpy of a thermodynamic system changes with pressure and volume, the heat capacity also decreases with increasing pressure. Van Wees et al. (2012) implemented a calculation of heat capacity of water that depends on *P*, *T* and *S*. This equation (Eq. 6) is derived from heat capacity experiments of water with variations in *P, T* and *S*.

List of technical input Parameters

Variables	Value	Unit
$T_{surface}$	10	C
T_{inj}	80	C
S	0.01	kg/kg
Ra_c	39.47842	-
dT/dz	0.031	C/m
Direct heat efficiency	100	%
$C_{p,rock}$	1000	J/kg K
ρ_{rock}	2500	kg/m3
g	9.81	m/s2
dP/dz(hydrostatic)	0.01	MPa/m
Well distance	200	m
d_{well}	9.625	inch
Pipe roughness	1.38	milli inch
Well skin	0	-
Minimum COP	15	-
T_{prod} for geothermal well	30	C
$P_{applied}$	110	%
φ	0.3	-

Table 1: This table lists all the technical input parameters of the Java model.

$$\mu = 0.1 + 0.333S + (1.65 + 91.9S^3)\exp(-(0.42(S^{0.8} - 0.17)^2 + 0.045)T^{0.8}) \quad \text{Eq. 3}$$

$$\rho_{fw} = 1 + 10^{-6}(-80T - 3.3T^2 + 0.00175T^3 + 489P - 2TP + 0.016T^2P - 1.3 \cdot 10^{-5}T^3P - 0.333P^2 - 0.002TP^2) \quad \text{Eq. 4}$$

$$\rho_w = \rho_{fw} + S\{0.668 + 0.44S + 10^{-6}[300P - 2400PS + T(80 + 3T - 3300S - 13P + 47PS)]\} \quad \text{Eq. 5}$$

$$C_p = (5.328 - 9.76 \cdot 10^{-2} + 4.04 \cdot 10^{-4}S^2) + (-6.913 \cdot 10^{-3} + 7.351 \cdot 10^{-4}S - 3.15 \cdot 10^{-6}S^2)T + (9.6 \cdot 10^{-6} - 1.927 \cdot 10^{-6}S + 8.23 \cdot 10^{-9}S^2)T^2 + (2.5 \cdot 10^{-9} + 1.66 \cdot 10^{-9}S - 7.125 \cdot 10^{-12}S^2)T^3 \quad \text{Eq. 6}$$

3.3.3 Transmissivity mapping with probabilities

From the permeability and thickness values that are obtained from the subsurface models at location (x,y), the horizontal transmissivity (*kH*) of the reservoirs is calculated. Transmissivity is a measure of how much water can flow through a reservoir per unit of time and has a direct relationship with reservoir permeability and thickness (Eq. 7). Transmissivity has therefore a large impact on the maximum applied flow rate that can be exerted on the reservoir.

$$kH = k \cdot H \quad \text{Eq. 7}$$

$$\ln kH = \ln k + \ln H \quad \text{Eq. 8}$$

ThermoGIS and REGIS both have data on uncertainties in their model for values of *k* and ThermoGIS also has uncertainty estimations of *H* of their layers. In order to estimate probabilities for transmissivities in different reservoir units, a transmissivity distribution has been generated through Monte Carlo sampling, as is done in the simulation of probabilities by Kramers et al (2012). Assuming that there is a lognormal distribution for *k* and a normal distribution for *H*, Monte Carlo sampling generates a new distribution of *kH* by multiplying random picked samples from the *k* and *H* distributions, which are generated from the standard deviation measurements. The procedure of multiplication is repeated 1000 times to generate a new transmissivity distribution and from this distribution new probability confidence levels are extracted and used to map transmissivities for each unit with confidences of: P10, P30, P50, P70 and P90 (Pluymaekers et al., 2012; Kramers et al., 2012). The P-values correspond to the probability (in %), e.g. P10 indicates a probability of 10% and so on. The impact of uncertainty in permeability on transmissivity is large. An example of this is shown in Fig. 8 where the probability curve of transmissivity for the Rotliegend aquifer is calculated by Pluymaekers et al. (2012).

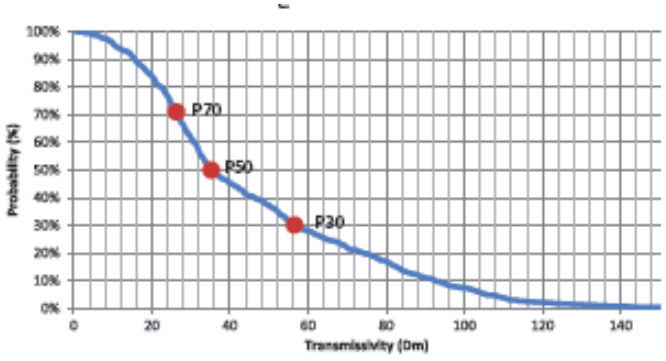

Fig. 8: The curve shows the probability distribution of the transmissivity in the Rotliegend aquifer at a certain location in the north of the Netherlands. It for example shows a 70% chance of obtaining kH values of 23 Dm. (Pluymaekers et al., 2012).

Because the vertical distance between some individual aquifers is limited, a system with a multiple point injection well can be considered. This system would jointly perforate multiple aquifers of the

same formation to increase the transmissivity and the total storage capacity. This vertical assimilation of aquifers could identify plausible areas, where in contrast to a insufficient single aquifer perforation system, it can now produce flow rates that are sufficient enough.

By using Eq. 7 and assuming that the permeability of a stacked reservoir is the weighted average of all reservoirs in the stack, the transmissivity of the stacked reservoirs is calculated using Eq. 9-7. In these equations the permeability and thickness of the sand layers within the formation are multiplied and summed. The sum is then divided by the summed thickness of the layers to get the weighted permeability. Finally the same method using Monte Carlo simulations is applied to calculate transmissivity of the stacked unit for different confidence levels.

$$sumkH = \sum_{i=0}^{n} k_i \cdot H_i \quad \text{Eq. 9}$$

$$\text{sumH} = \sum_{i=0}^{n} H_i \quad \text{Eq. 10}$$

$$k_{stacked} = \frac{sumkH}{sumH} \quad \text{Eq. 11}$$

$$k_{stacked\ STD} = \frac{sumkH_{STD}}{sumH_{STD}} \quad \text{Eq. 12}$$

3.3.4 Maximum flow rate

The power that can be extracted from heat storage depends largely on the flow rate that can be achieved in the well. If the flow rate in the injector is increased and the transmissivity of the reservoir is low, a pressure build up can be observed. In order to prevent overpressure of the system, a maximum applied overburden pressure ($P_{applied}$) on the reservoir of 10% of the hydrostatic pressure is adopted. This value is based on previous regulations defined by TNO for geothermal production (Paalvast & Thienen-Visser, 2014). This means that the maximum pressure in the reservoir is 110% hydrostatic pressure, deeming the pressure loop in the reservoir unsafe when they exceed this threshold.

The hydraulic resistivity of the reservoir is a measure of the reservoirs resistance against flow and is inversely proportional to the transmissivity, in association with the viscosity of the injected water. When fluid flows from the injector well to the producer well, the hydraulic resistivity causes a pressure loss between the injector and producer. The friction of the injected water with the well casing also causes a pressure loss. Verruijt (1970) and Van Wees et al. (2012) defined the pressure loss in the loop as an product of the flow rate (Q), the viscosity (μ), the transmissivity (kH), the distance between the wells (L_{wells}), the skin factor due to potential clogging (s) and the well diameter (d_{well}). The skin factor is a measurement of the pressure loss where a positive s increases the pressure loss (clogging) and a negative skin factor decreases the pressure loss (stimulation). If it is assumed that $P_{applied}$ is equal to the pressure loss with a constant flow rate, the maximum flow rate that can be applied in the HT-ATES system can be calculated(Eq. 13), by using the calculations from Verruijt (1970) and Van Wees et al. (2012).

$$Q_{max} = P_{applied} \frac{2\pi kH}{(\mu_{inj} + \mu_{prod})[ln\left(\frac{L_{wells}}{0.5d_{well}}\right) + s]} \quad \text{Eq. 13}$$

3.3.5 Pressure difference to drive loop

The pressure evolution in the pipes of the well depends on three different forces: gravitational forces, friction and inertial forces (Van Wees et al, 2012). Water is almost incompressible, therefore the inertial force is neglected. The pressure effects in the surface installations are also neglected, due to the assumption that the surface installations are close to the well locations and therefore the length of the pipes at the surface are small. The pipes at the surface usually have large diameters and this also results in small pressure losses. Gravitational forces are also neglected, because the net gravitational force in the loop between the injector and producer well equals zero.

$$dP_{well} = \frac{fL_{well}\rho_w v^2}{2d_{well}} \quad \text{Eq. 14}$$

$$dP_{loop} = dP_{well,inj} + dP_{well,prod} + P_{applied} \quad \text{Eq. 15}$$

The pressure evolution of the injected and produced water in a pipe is derived by the Darcy Weissbach or Fanning equation (Eq. 14) for pressure losses due to friction in pipes (Beggs & Brill, 1973; Romeo et al., 2001; Van Wees et al., 2012). The pressure loss depends on the friction coefficient (*f*), the diameter average stream velocity (*v*), the well diameter (d_{well}) and the density of the water injected or produced ($\rho_{w,inj}$ *or* $\rho_{w,prod}$). The friction coefficient depends on the ratio of inertial forces to viscous forces, the pipe roughness and the well diameter (see Eq. 18). The ratio between the inertial forces and viscous forces can be related by the Reynolds number, where a higher number represents a more turbulent flow due to a lower viscosity (see Eq. 16). The calculation for v is given in Eq. 17, where v mainly depends on the geometry of the well**.** The total pressure in the loop is therefore a summation of the pressure loss in the injector, in the producer and the maximum pressure difference at reservoir level (see Eq. 15).

3.4 SENSITIVITY STUDY OF THE EFFICIENCY OF A HT-ATES SYSTEM

$$Re = \frac{\rho v d_{well}}{\mu} \quad \text{Eq. 16}$$

$$v = \frac{4Q}{\pi d_{well}^2} \quad \text{Eq. 17}$$

$$f = \left[1.14 - 2\log\left(\frac{\varepsilon}{d_{well}} + \frac{21.25}{Re^{0.9}}\right)\right]^{-2} \quad \text{Eq. 18}$$

The recovery efficiency of the HT-ATES system is related to energy losses in the aquifer. When high temperature water is injected into a reservoir, which has a lower initial temperature than the injected water, the energy balance will result in an energy loss of the injected water to the reservoir. The stored high temperature water will lose energy to the rock matrix in which it is stored and the confining aquitards by conduction and it loses energy by convection. This convection is caused by a density difference buoyancy flow. This consists of a density difference between the lower density injected water with a higher temperature T_{inj} and the higher density initial in-situ groundwater with a lower temperature T_{situ}. The temperature loss of the water in the wells is neglected in this study, due to small diameters of the wells. This assumes that the wells have a small surface area with the

surrounding rock and therefore do not lose energy via conduction. The pressure loss defined in Section 3.3.5 is therefore assumed to be the largest contributor to energy losses in wells, because a pressure loss results in a decrease in flowrate and thus a loss of energy. This pressure loss is not considered in the calculation of efficiency. However, it is implemented in the Java code to calculate the performance of the HT-ATES system.

Several studies have been done to approximate the efficiency of HT-ATES systems (Bakker, 2009; Schuit et al., 2014; Van Lopik et al., 2016). Three different methods, which include numerical or analytical approaches, are tested in this study and 9 test cases are compared using those different methods (see sections 3.4.2-3.4.4).

3.4.1 Benchmark for sensitivity study

The 9 test cases that are used as a benchmark for comparing the three different methods are described in Table 3 below. The base case is derived from observed values in the REGIS II v2.2 model. Every variable is increased and decreased by 50% except for the permeability. This is because a 50% change in permeability will not result in significant change (derived from personal communication with the TNO supervisors J. G. Veldkamp and J. D. A. M Van Wees).

Constants	Value	Unit
ρ_{rock}	2500	kg m^{-3}
λ	4	W m^{-1} K^{-1}
t_{inj}	152	days
t_{prod}	152	days
$t_{lifetime}$	15	years
S	0.01	kg kg^{-1}
$T_{cuttoff}$	T_{res}	°C
T_{inj}	80	°C
dT/dz	0.031	°C m^{-1}

Table 2: Shows the constants that are used for the sensitivity analyses

All the methods described in the following sections assume a single confined aquifer, where the set depth(z) of the aquifer is in the middle of the aquifer. The methods also assume that there is no increase in pressure due to injection, because simultaneously colder water is produced at a well near the injector well and vice versa during production. This set up assumes that the distance between the two wells is large enough to prevent the second well from influencing the efficiency of the primary well during injection, storage and recovery. It also assumes that the pressure difference in the injector and producer wells are equal.

Testcase nr	1	2	3	4	5	6	7	8	9
	Base case	Q +50%	Q -50%	k +100%	k -99%	z +50%	z -50%	H +50%	H -50%
Q [m3/s]	150	225	75	150	150	150	150	150	150
k [D]	5	5	5	10	0.05	5	5	5	5
z [m]	300	300	300	300	300	450	150	300	300
H [m]	100	100	100	100	100	100	100	150	50

Table 3: Shows the varying parameters that are used in the different test cases.

3.4.2 Radial Dupuit Interface Flow efficiency analyses

A TNO report from Pluymaekers et al. (2013) used a spatially and temporally constant efficiency of 75% in their potential assessment of HT-ATES systems. This constant was based upon a research done by Bakker (2009) where the recovery efficiency of fresh water storage in saline aquifers was calculated. Their study calculates the position of the interface between the less dense fresh water and the denser saline water over time, incorporating the injection, storage and production phases of the storage system. The change in position of the interface with time depends, according to their calculations, on a dimensionless number D (Eq. 19). Their study uses the density contrast between the fresh and saline water, where in this study the density difference depends on temperature instead of salinity and thus assumes the dimensionless density difference to be $\rho^* = (\rho_{w,ground} - \rho_{w,inj})/\rho_{w,inj}$. Note that D is negative for injection and positive for production, because the flow direction changes. The position of the interface is then calculated, assuming radial homogeneous flow, in a 2D section dimensionless numerical simulation of the interface, where $\sigma = x/H$ denotes the horizontal

position of the interface and ζ = z/H denotes the vertical position of the interface (see Fig. 9). The dimensionless radial velocities of the tip and toe of the interface are given by Eq. 20 and Eq. 21.

$$D = \frac{Q}{k\rho^* H^2} \quad \text{Eq. 19}$$

$$v_{tip} = \frac{-D}{2\pi}\frac{1}{\sigma} + \left(\frac{\partial\sigma}{\partial\zeta}\right)^{-1} \quad \text{Eq. 20}$$

$$v_{toe} = \frac{-D}{2\pi}\frac{1}{\sigma} - \left(\frac{\partial\sigma}{\partial\zeta}\right)^{-1} \quad \text{Eq. 21}$$

The interface movement is computed using an implicit finite difference scheme in combination with a Runge-Kutta predictor-corrector procedure, specifically the Cash-Karp method (Cash & Karp, 1990), in order to estimate accurate values of the radial velocity during a time step. For the *i*-th iteration the position of the interface is calculated by σ(i) = σ(i-1) + dτ(i)·v_{toe}(i), where dτ(i) is the dimensionless time step taken at the *i*-th iteration. To reduce the errors in the predictor-corrector procedure, an adaptive step size control is used. This adaptive step size control is explained by Press et al. (1988) and decreases the step size of the Runge-Kutta method if the difference between the predictor and corrector is larger than 10^{-5}.

In order to calculate the efficiency, an injection period t_{inj} and a production period t_{prod} are assumed, where the flow rate during injection and production is constant. A boundary condition is set during the production period, where production stops when the toe of the interface reaches the well. This is assumed to prevent cold water from being produced. The volume that is produced (V_{prod}) is then calculated by multiplying Q with t_{prod}, where t_{prod} is calculated by summing the iterative time steps until the boundary condition of the toe is met. The main assumption that is made in this calculation considers that energy loss due to conduction or diffusion of the injected water is neglectable. The production temperature is equal to the injection temperature. There is only a volumetric loss due to density driven flow.

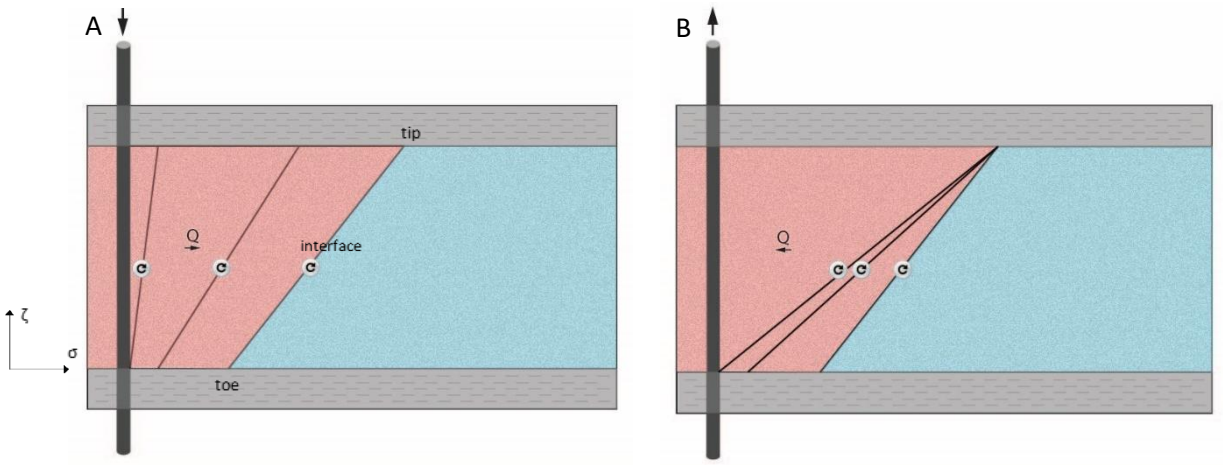

Fig. 9: A schematic drawing of the effects of density driven flow during injection and production in a confined aquifer. The arrows indicate the flow direction. The black lines indicate the position of the interface between the warmer(red) injected water and the colder(blue) ground water over time. Figure A represents the injection phase and figure B represents the production phase.

The remaining volume is then added to the time loop of the following year and this continues for a lifetime ($t_{lifetime}$) of 15 years. For each year the efficiency is calculated using Eq. 22, followed by calculating the average efficiency over the HT-ATES systems lifetime with Eq. 23.

$$\mu_{eff,i} = \frac{V_{prod}}{V_{inj}} \cdot 100\% \quad \text{Eq. 22}$$

$$\mu_{eff} = \frac{\sum_{i=1}^{t_{lifetime}} \mu_{eff,i}}{t_{lifetime}} \quad \text{Eq. 23}$$

3.4.3 Rayleigh based efficiency analyses

Schout et al. (2014) numerically evaluated prime factors influencing the recovery system of HT-ATES systems using HstWin-2D, which is a numerical code that is developed for heat and solute transport in porous media. Their numerical simulation consisted of testing 78 different model scenarios. They tried to find a relationship between the recovery efficiency of HT-ATES systems with the Rayleigh number (Ra). The Rayleigh number is a measure of heat transfer through conduction and convection (Hewitt et al., 2014; Schout et al., 2014). The onset of free convection in a porous medium occurs when the Ra is higher than the critical Rayleigh number Ra_c, which is approximately equal to $4\pi^2$. The recovery efficiency is defined in their research as the ratio between the recovered amount of energy and the stored amount of energy with respect to the ambient groundwater temperature. Schout et al. (2014) found an exponential relationship by plotting Ra of the 78 model scenarios using Eq. 24 against the numerically calculated efficiencies. In this relation the temperature dependent density and viscosity are assessed at the average system temperature T_m, assuming that there is no change in density or viscosity between the top and bottom of the reservoir and between the injected and in-situ groundwater (see Eq. 25).

This relationship did not comply for a number of parameters that do not affect the Ra. These parameters included the k_h and the V_{inj}. In order to improve the exponential relation, an adjusted version of the Rayleigh number was made (Ra^*). This adjustment replaces k_v by $\sqrt{k_v k_h}$, which is in accordance with the formula to calculate the characteristic tilting time of a thermal front due to density driven flow that is defined by Hellström and Tsang (1988). Schout et al. (2014) shows that V_{inj} is inversely proportional to the aspect ratio H/R_{th}, where R_{th} is replaced by $\sqrt{V_{inj}C_{v,w}/\pi H C_{v,a}}$. Taking these two adjustments into account, the Ra^* is calculated using Eq. 26.

$$Ra = \frac{\alpha \rho g H C_{v,w} k_v \Delta T}{\mu \lambda} \quad \text{Eq. 24}$$

$$T_m = \frac{T_{inj} + T_{situ}}{2} \quad \text{Eq. 25}$$

$$Ra^* = \frac{\alpha \rho g H^2 C_{v,a} \sqrt{k_v k_h} \Delta T}{\mu \lambda \sqrt{\frac{V_{inj} C_{v,w}}{\pi H C_{v,a}}}} \quad \text{Eq. 26}$$

The resulting relationship of the Ra^* with the efficiency scatter plots of Schout et al. (2014) took the general form of an exponential function(Eq. 27). It was found that for every set of scenarios where the aquifer thicknesses are the same value, A and B are constant, suggesting a variable relationship of the A and B parameters in Eq. 27 which depends on aquifer thickness (Fig. 10).

Through curve fitting methods the functions Eq. 28, Eq. 29 and Eq. 30 were found to give the best fit for the efficiency curve. The B parameter differs for different ranges of H, where Eq. 29 is valid when the aquifer thickness ranges between 10 and 60 m and Eq. 30 is valid in ranges between 60 and 200 m (Schout et al., 2014). Because the thickness of certain aquifers in the Netherlands are larger than 200 m, it is assumed in this sensitivity analyses that Eq. 30 is also valid for H >200 m.

$$\mu_{eff} = Ae^{B_{1,2}Ra^*} \quad \text{Eq. 27}$$

$$A = 0.82 - \frac{1.70}{H^{1.2}} \quad \text{Eq. 28}$$

When 10<H<60 [m]: $B_1 = -\frac{1.2}{H^{1.35}} + 2.2 \cdot 10^{-3}$ Eq. 29

When H≥60 [m]: $B_2 = -\frac{2.7}{H^{1.7}}$ Eq. 30

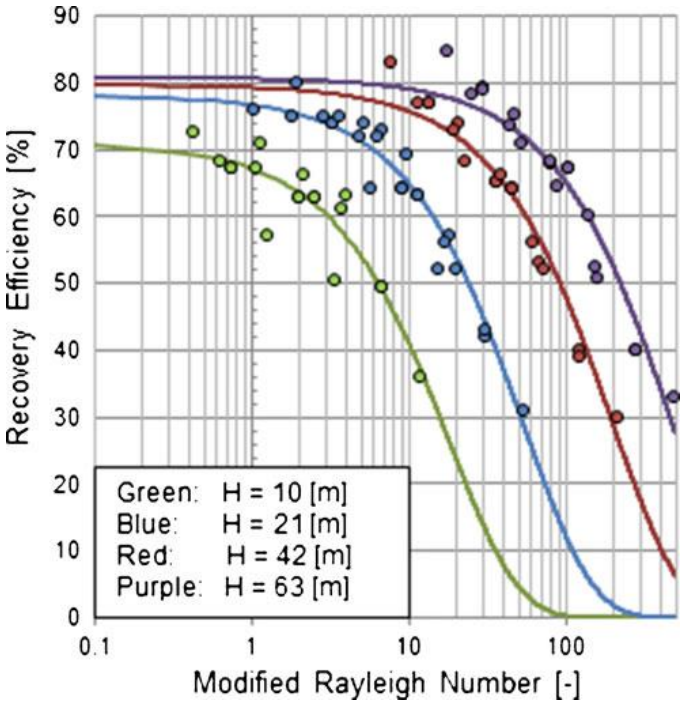

Fig. 10: The correlation between Ra^* and the recovery efficiency in the fourth year for all modeled scenarios in the study done by Schout et al. (2014). Green, blue, red and purple circles are the data points and the exponential trend lines corresponding with aquifer thicknesses of respectively 10, 21, 42 and 63 m.

3.4.4 DoubletCalc3D efficiency analyses

DoubletCalc3D v1.0 (2015) is a software tool that is developed by the research institute TNO for the subsurface simulation of geothermal wells. It enables the user to calculate the temperature and pressure development around two or more wells in three dimensions over time (Veldkamp et al., 2015). The software can be downloaded for free on the website www.nlog.nl under the GNU Lesser General Public License.

Instead of using it for the simulation of geothermal wells, it can also be applied for the subsurface simulation of HT-ATES systems. DoubletCalc3D needs a prior defined grid of the subsurface to do the subsurface calculations on. Therefore a 3D grid was designed with the Petrel E&P software. This grid consists of 4 different layers with different properties (Fig. 12). The other two methods in the sensitivity analyses of this study do not incorporate well design in the calculation of efficiency, whereas DoubletCalc3D can only be used with a double well model input. The problem with DoubletCalc3D is that it needs a double well design. In order to prevent well2 from influencing well1, a grid design is chosen where one well perforates the first sand layer (Z1) and the second well perforates the second sand layer (Z2), by inactivating cells in the wells where it is not supposed to perforate the layer (right figure in Fig. 12). The property grid that defines this inactivation of cells in the well design is called actum. Other property grids are also defined including: horizontal permeability, vertical permeability(10% of the horizontal permeability), temperature and depth.

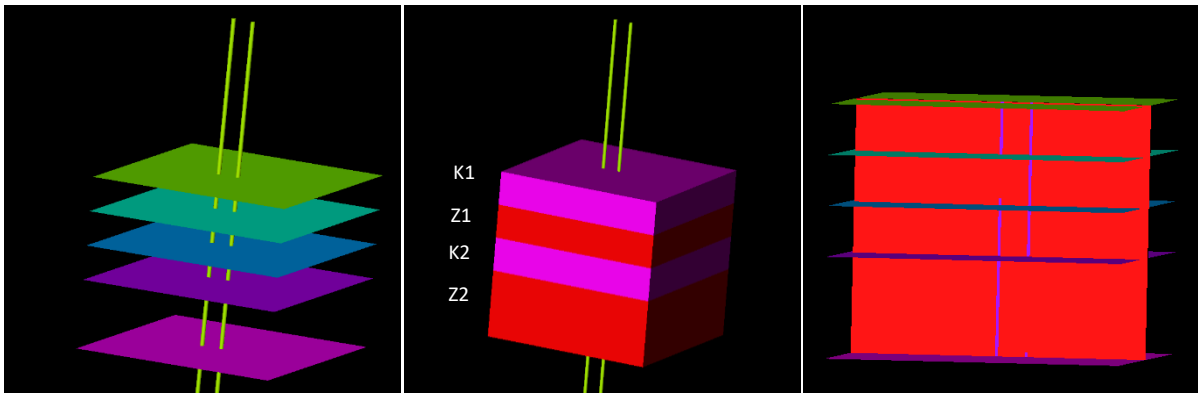

Fig. 12: The left figure shows the defined horizons in petrel. The middle figure shows the property k_h that is given to the different layers, where purple indicates a low k_h and red a high k_h. The right figure shows the well settings active cells in the grid (actnum), where red indicates active cells and blue indicates inactive cells.

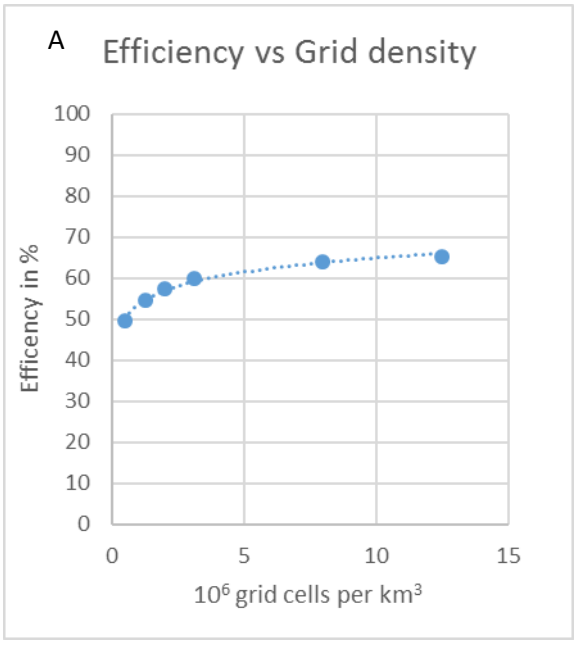

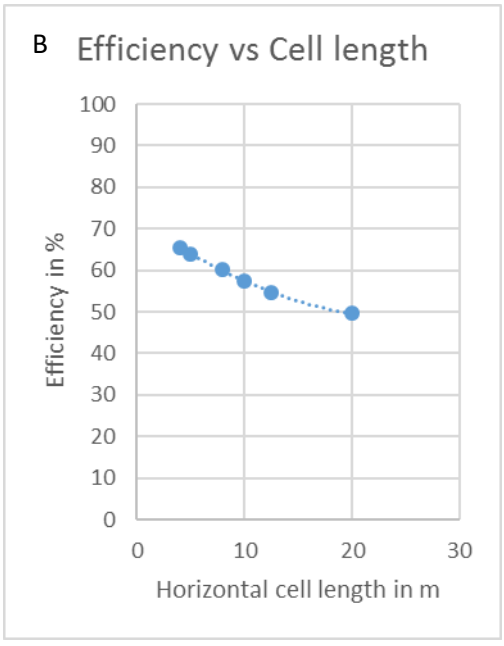

Fig. 11: These values are calculated with DoubletCalc3D with the parameters for the base case. Graph A shows the grid density per km^3 versus the corresponding efficiency and graph B shows the uniaxial horizontal length of one individual cell versus the efficiency. For example a 5x5x5 m grid has a grid density of 8·10^6 grid cells per km^3 and has an uniaxial horizontal length of 5 m.

The boundary conditions of flow at the boundary of the grid are set to enable flow in and out of the grid within the layer. This is necessary to prevent an enormous increase of pressure in the reservoir. The confining clay layers (K1&2) are set to be almost impermeable with $k_{h,\,clay}$ and $k_{v,\,clay}$ set at 0.01 mD. This model setup will minimize the influence of the second well on the first one. For every test case, different grids are designed with the horizon settings defined in Table 4 below. A small sensitivity analysis was also done for obtaining the most accurate grid density setting with the least amount of computational time. A grid with cells of 5x5x5 m was chosen as the most suitable, considering a high accuracy while limiting the computational time needed by DoubletCalc3D (Fig. 11).

Petrel settings horizon depths									
Test case	**1**	**2**	**3**	**4**	**5**	**6**	**7**	**8**	**9**
Top k1	200	200	200	200	200	350	50	175	225
Top z1	250	250	250	250	250	400	100	225	275
Top k2	350	350	350	350	350	500	200	375	325
Top z2	400	400	400	400	400	550	250	425	375
Base z2	500	500	500	500	500	650	350	525	475

Table 4: This table shows the horizon depths used for the different test cases. The depth is given in m.

The grid is then uploaded into DoubletCalc3D including the property grids for: k_h, k_v, T_{res} and actnum. The benchmark parameters in Table 2 & Table 3 are then inserted in the advanced settings tab. A correction for the well coordinates is also made because DoubletCalc3D stretches the grid, which displaces the wells in the horizontal plane. The location of the wells are then changed within DoubletCalc3D to correct for this displacement that is caused by the stretching. The time step is set in months for a duration of 180 months (15 years). By using an input Excel sheet, the injection time is set to be 5 months, followed by a storage period where there is no in- or outflow for 1 month. Next the production iterates for 5 months and then also stops for 1 month. This process is repeated for a total of 180 months. The injection temperature in Z2 is set at 17 °C, which is almost equal to T_{situ}, in order to reduce the effect it has on the efficiency of the storage in Z1 (i.e. energy loss).

DoubletCalc3D then writes a table that gives the: $C_{p,j}$, $\rho_{w,j}$, T_{inj} and $T_{prod,j}$ per month *j* that is modelled. From this we can calculate the annual efficiency of the HT-ATES system at year *i* using Eq. 31, assuming that the efficiency equals the ratio between the energy produced and the energy injected minus the heat already in place of the reservoir, where the heat during production ($7 \leq j \leq 11$) is summed and divided by the sum of the heat injected during injection ($1 \leq j \leq 5$). The average efficiency over the lifetime of the HT-ATES system is then calculated using Eq. 23.

$$\mu_{eff,i} = \frac{\sum_{j=7}^{11} Q_{month} C_{p,j} \rho_{w,j} (T_{prod,j} - T_{situ})}{\sum_{j=1}^{5} Q_{month} C_{p,j} \rho_{w,j} (T_{inj,j} - T_{situ})} \cdot 100\% \qquad \text{Eq. 31}$$

3.5 ECONOMIC FRAMEWORK

This study utilizes the framework of the Excel sheet workflow for calculation of the economic feasibility for HT-ATES systems, that was created by Pluymaekers et al. (2013). All the calculations that are implemented in the Excel workflow, are translated into Java code. The precision of the Java code with respect to the Excel workflow has been tested, giving identical results.

3.5.1 Benchmark for the economic framework

In order to compare the results from the economic model, the following parameters show in Table 5 are taken as constant throughout the Netherlands. The business case that corresponds with those constants is as follows. The economic framework is shaped for a system where a geothermal doublet is coupled to a HT-ATES system in order to efficiently store the residual heat of the heat production from the geothermal well. The hot water produced from the HT-ATES system is then directly connected to a district heating network. The constants listed in the table below are assumed to represent a realistic business case. These constants are hard-coded into the Java model, but could be changed to assess different business cases.

List of economic input Parameters		
Variables	**Value**	**Unit**
Well costs	1000	eur/m depth
Stimulation costs	0	eur
Pump investment	100000	eur/pump
Pump Efficiency	63	%
Economic Lifetime	15	yr
Electricity price for driving pumps	140	eur/MWh
Heat plant investment costs	150	euro/MWth
Direct heat fixed O&M rate	3	%
Inflation	2	%
Loan rate	6	%
Required return on equity	15	%
Equity share in investment	20	%
Taxrate	25.5	%
Term loan	15	yr
Depreciation period	15	yr
Gas price	0.25	Euro/m3
Calories Gas	31.65	GJ/m3
Maximum LCOE	6	Euro/GJ
Number of wells	2	-
Load hours	3000	hours

Table 5: This table lists the constants that are hard-coded into the Java workflow. These constants are partially derived from previous work that is done by Pluymaekers et al. (2013) and partially approximated with help from Joris Koorneef.The fixed O&M rate stands for fixed Operation and Maintenance cost. Note that the load hours represent the injection time in hours.

3.5.2 Coefficient of Performance

The coefficient of performance (COP) is a measure of the overall efficiency for heat storage in the subsurface, taking into account: the pressure difference in the loop, the HT-ATES efficiency, the pump efficiency (ε_{pump}), the reinjection temperature into the geothermal well and the injection temperature of the HT-ATES, the heat capacity of the water that is injected and the density of the injected water. The COP is the ratio (Eq. 32) between the energy that is stored (E_{stored}) and the gross pump power required to drive the pumps (E_{pump}). In order to reduce the runtime of the Java calculations a minimum COP of 15 is adopted, assuming that in practice COP values below 15 do not provide much (see section 3.5.3 below). Additionally, this cut-off limitation reduces the amount of grid cells that is considered for calculation of the economic potential, lowering the computational time needed to run the model. This is because grid cells with a COP<15 are given a NO-DATA value.

$$COP = \frac{E_{stored}}{E_{pump}} = \frac{\rho_w C_p (T_{reinj} - T_{inj})}{dP_{loop}\left(1 + \frac{1}{\mu_{eff}}\right)(\frac{1}{\varepsilon_{pump}})} \quad \text{Eq. 32}$$

3.5.3 Levelised Costs of Energy

For the assessment of the economic feasibility of a HT-ATES system, a calculation of the costs per unit energy needs to be done. Limburger et al. (2014) and van Wees et al. (2012) both used the Levelised Cost of Energy (LCOE) to assess the potential of a geothermal doublet, which is the ratio of the equity share minus the accumulated discounted net revenue of the operation with the accumulated discounted energy, measured in EUR/GJ (Eq. 33).

$$LCOE = \frac{Equity\ share - Cumulative\ discounted\ net\ revenue}{Cumulative\ discounted\ energy\ sales} \quad \text{Eq. 33}$$

$$\begin{aligned} Equity\ share &= Equity\ share\ in\ investment \cdot Total\ investment \\ &= Equity\ share\ in\ investment \cdot (Capex_{subsurface} \\ &+ Capex_{power} + Capex_{heat}) \end{aligned} \quad \text{Eq. 34}$$

$$\begin{aligned} &Cumulative\ discounted\ revenue \\ &= \sum_{t=1}^{lifetime} \frac{Net\ revenue\ after\ taxes_t}{(1 + Equity\ return)^t} \\ &= \sum_{t=1}^{lifetime} \frac{(Gross\ revenue_t + Tax_t + Total\ loan\ charges_t)}{(1 + Equity\ return)^t} \end{aligned} \quad \text{Eq. 35}$$

$$\begin{aligned} &Cumulative\ discounted\ energy\ sales \\ &= \sum_{t=1}^{lifetime} \frac{Energy\ sales\ after\ taxes_t}{(1 + Equity\ return)^t} \\ &= \sum_{t=1}^{lifetime} \frac{E_{prod,t}(1 - Taxrate)}{(1 + Equity\ return)^t} \end{aligned} \quad \text{Eq. 36}$$

The equity share represents the users share in the total investment. The equity share is the product of the equity share in the investment with the total investment (Eq. 34). The total investment is the sum of all capital expenditure (Capex). The cumulative discounted net revenue is the Net Present Value (NPV) of all net revenue, after applying taxes, over the lifetime of the HT-ATES system (Eq. 35). The NPV is the total present value of the time series of revenue or energy sales, using the equity return on the investment (Van Wees et al., 2012). The cumulative discounted energy sales is therefore the NPV of all energy sales after applying taxes (Eq. 36).

LCOE	Potential
LCOE<0.01	Not plausible
0.01<LCOE<1	Exceptionally high
1<LCOE<2	Very high
2<LCOE<3	High
3<LCOE<4	Very good
4<LCOE<5	Good
5<LCOE<6	Moderate
6<LCOE<15	Low
15<LCOE<30	Very low
30<LCOE	None

Table 6: Correlation of the LCOE in EUR/GJ with the potential of the HT-ATES system.

The costs of the energy that is imported from an external energy supplier (in this case the geothermal doublet) are not incorporated in this economic framework, because these costs can differ greatly depending on the energy source, supply route and location. Considering this, it is assumed that a LCOE of higher than 6 EUR/GJ is not cost effective. The resulting LCOE ASCII grids are therefore categorized into 10 different groups shown in Table 6.

These calculations are not discussed in detail in the main part of this report, because only one business case is tested and no detailed analyses on these assumptions is done. It could however be interesting for investors to see how the economic framework is done. A more detailed listing of the calculations done for the economic framework is therefore given in Appendix A.

4 RESULTS

This research produced a large amount of results consisting of 12591 files, which comprises of different grids for different probabilities in multiple file formats. This large amount of data is too large to be presented as a whole. Therefore only the results of the stacked layers are shown in the Results section. Some of the results of the individual layers that are of interest are shown in Appendix B. The remaining data are stored on the TNO server and can be accessed.

The results of the Java workflow in sections 4.2 to 4.7 and in Appendix B are visualized as maps in the Amersfoort/RD new coordinate reference system, where the coordinate axes give the position in meters. Note that the data from the ThermoGIS database is originally given in the WGS 84/UTM Zone N31 coordinate reference system. A coordinate transformation in ArcMap is therefore used to visualise this data in the Amersfoort/RD new coordinate reference system.

4.1 SENSITIVITY ANALYSES ON RECOVERY EFFICIENCY

The results of the sensitivity analyses for the three different methods, used to calculate the recovery system of HT-ATES, are shown in Fig. 13(A-E). The efficiencies for the different test cases that are calculated with DoubletCalc3D and with the analytical method from Schout et al. (2014) appear to have similar trends, while the results of the analytical method from Bakker (2009) are on average much lower with two extreme exceptions(Fig. 13A). For test cases 5 and 9, the results from the Radial Dupuit Interface Flow calculations show exceptionally large efficiencies.

Fig. 13B generally shows a declining trend in efficiency with increasing permeability of the reservoir. The Bakker (2009) results show that at lower permeabilities the efficiency decreases more rapidly than at higher permeabilities. The trendline that best fits the data is an exponential function. The results from the DoubletCalc3D and Schout et al. (2014) are more similar to one another and show a less steep exponential trend.

The relationship between efficiency and thickness of the reservoir is shown in Fig. 13C. The data points from the Bakker (2009) calculations indicate that thickness has a large contribution to the recovery efficiency, where efficiency decreases with increasing thickness and the rate of change decreases with increasing thickness, showing a quadratic relationship with thickness. The results from the Schout et al. (2014) calculations show a less step linear decrease of efficiency with thickness, with respect to the Bakker (2009) results. On the contrary, the results from DoubletCalc3D show a slight linear increase of efficiency with thickness.

The influence of change in depth on the recovery efficiency does not seem to be that large (Fig. 13D). Both the results from the DoubletCalc3D and Bakker (2009) calculations show that the recovery efficiency slightly increases linearly with depth, whereas the results from Schout et al. (2014) barely change with depth and could be considered to remain constant with depth.

Fig. 13E shows the relationship between the recovery efficiency and the flow rate that is used during injection and production. The results from the Bakker (2009) and the Schout et al. (2014)

calculations indicate an logarithmic increase of efficiency with flow rate, while the DoubletCalc3D results show an insignificant change in efficiency with varying flow rates.

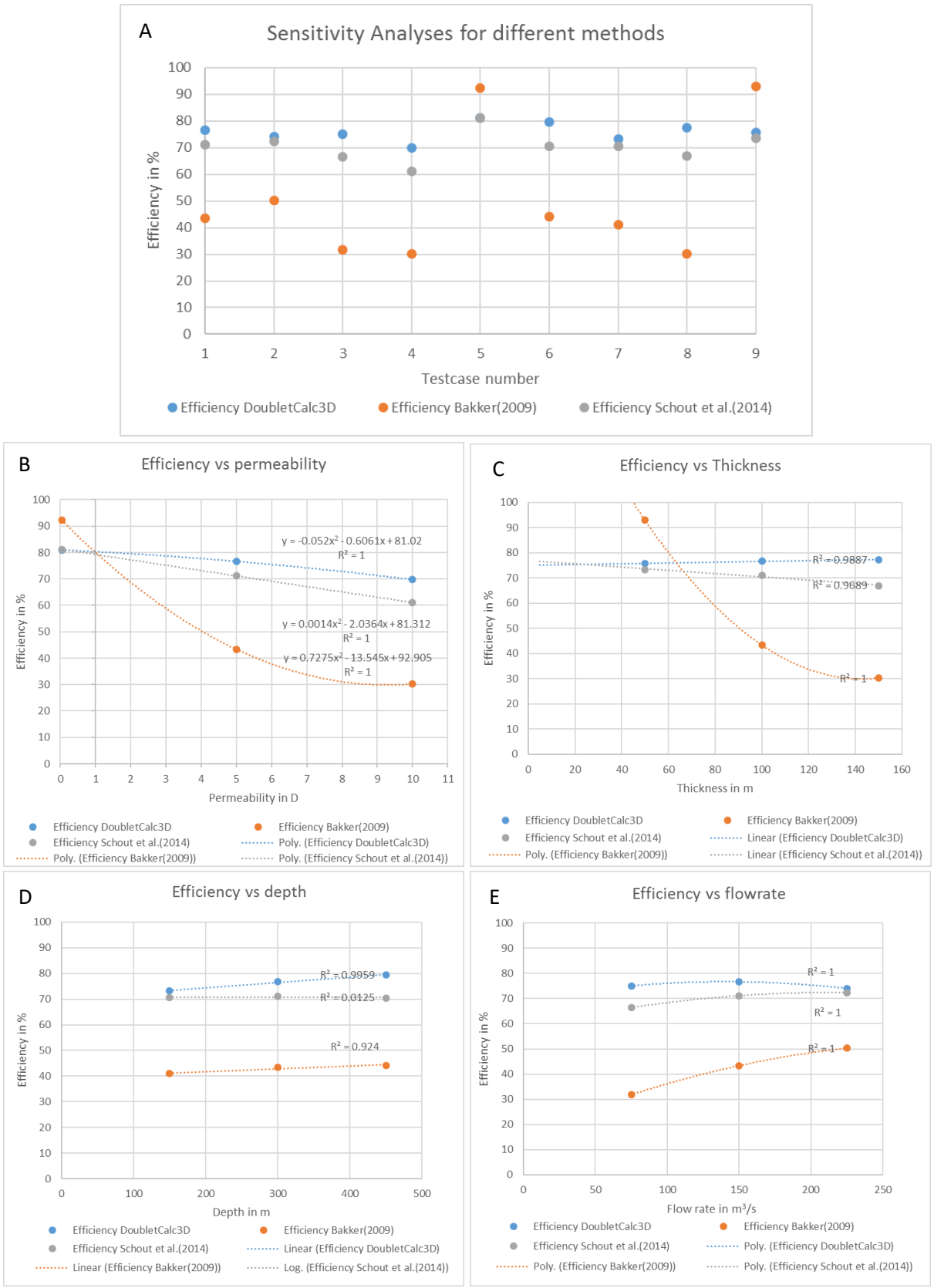

Fig. 13: These figures show the results from 9 test cases of the three different methods to approximate the recovery efficiency of a HT-ATES system. An overview of the results from the different test cases is given in (A). The relationship of recovery efficiency in % with permeability(B), thickness(C), depth(D) and flow rate(E) for the three methods are given with trend lines that fit the data points. The blue dots represent the data that is obtained by the DoubletCalc3D simulations, the grey dots represent the data that is obtained by the Rayleigh-based analytical calculations from Schout et al.(2014) and the orange dots represent the data that is obtained from the numerical calculations that use Radial-Dupuit Interface flow by Bakker (2009).

4.2 TRANSMISSIVITY

The Delft Sandstone Member has on average very low transmissivities (<15 Dm), with exceptions in some parts of the reservoir (e.g. near the city of Leiden) where it locally increases to approximately 45 Dm. The stacked reservoirs of the Rijnland Group exhibits on average the same low transmissivity as in the Delft Sandstone Member, while the area extent and amount of increase in transmissivity in some local areas is larger. In the western and southern parts of Zuid-Holland transmissivities of up to 150 Dm can be found in the Rijnland Group, and in the south eastern part of Drenthe transmissivity increases to >100 Dm. The transmissivity in the North Sea Group is on average a little higher (~17Dm). The North Sea group reservoirs in the north of the Netherlands have a low transmissivity, while reservoirs in the south eastern part of the Netherlands have values up to 150 Dm.

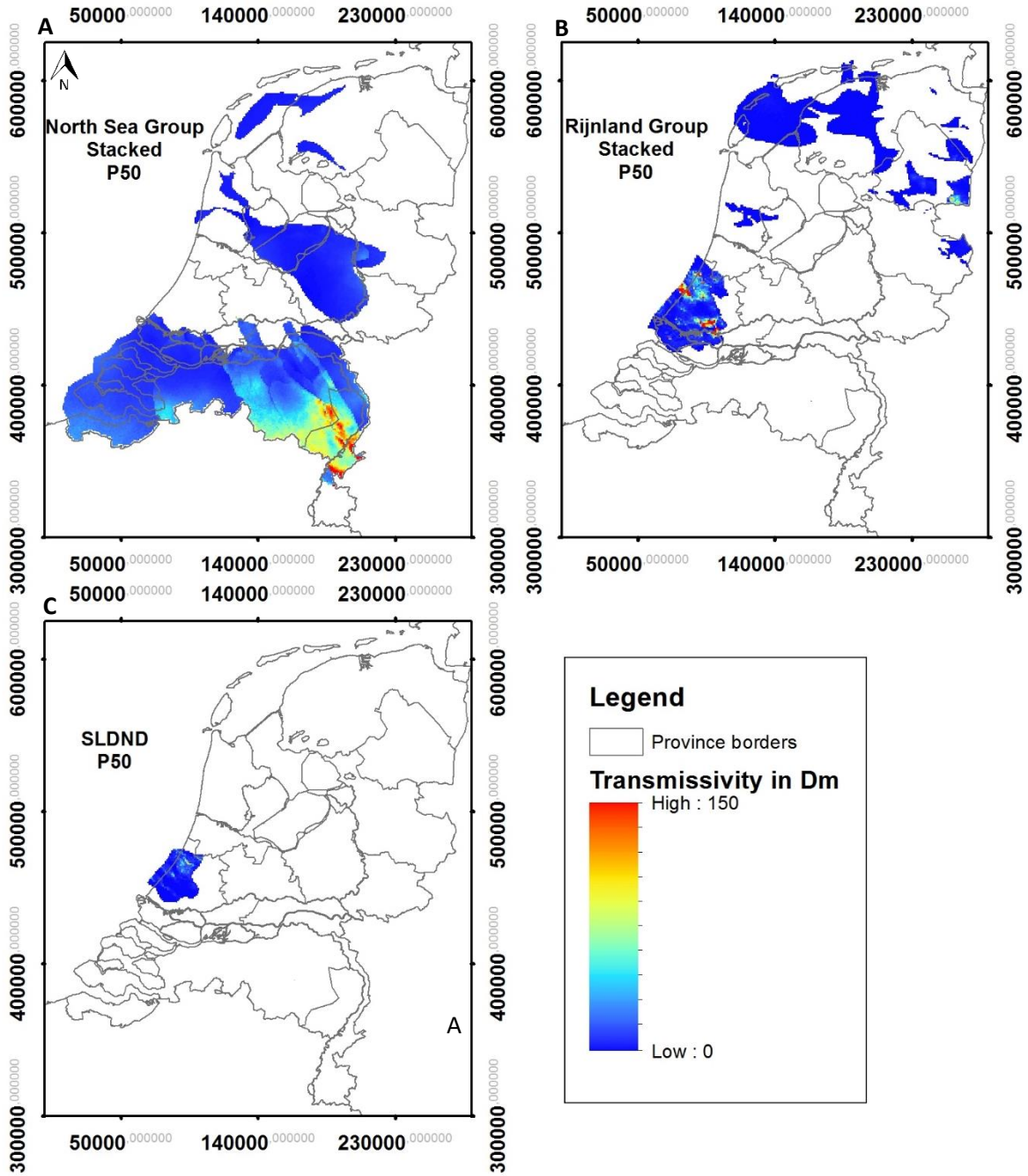

Fig. 14: The top two figures show P50 transmissivity maps for the stacked reservoirs of the North Sea Group and the Rijnland Group. The figure on the bottom left is the P50 transmissivity map of the Delft Sandstone Member. Note that this transmissivity scale is smaller than in Fig. 15.

The results from the stacked reservoirs of the Breda, Oosterhout and Maassluis formations in the Upper North Sea Group show significantly higher transmissivities. The stacked Breda formation has an average transmissivity of around 680 Dm. The average transmissivity of the stacked Oosterhout Formation is around 520 Dm and the average of the stacked Maassluis Formation is around 580 Dm. The resulting transmissivity maps that are presented in Fig. 15 are therefore presented with a different scale, in order to better visualize the higher range of transmissivity values.

The Breda Formation appears to have a lower transmissivity (~250 Dm) in the areas around Gelderland, western Noord-Brabant and Zeeland; whilst increasing up to 2500 Dm in the central part of Limburg and eastern part of Noord-Brabant. The Oosterhout formation shows very high values (>2500 Dm) in the western part of Noord-Brabant, whereas it generally decreases more toward the north of the Netherlands. The Maassluis Formation shows a distribution of relatively high values, between 750 and 1500 Dm, covering most of Zuid-Holland and the western part of Utrecht. Increase of transmissivity in the Maassluis Formation can also be found in northern Gelderland and the Waddenzee.

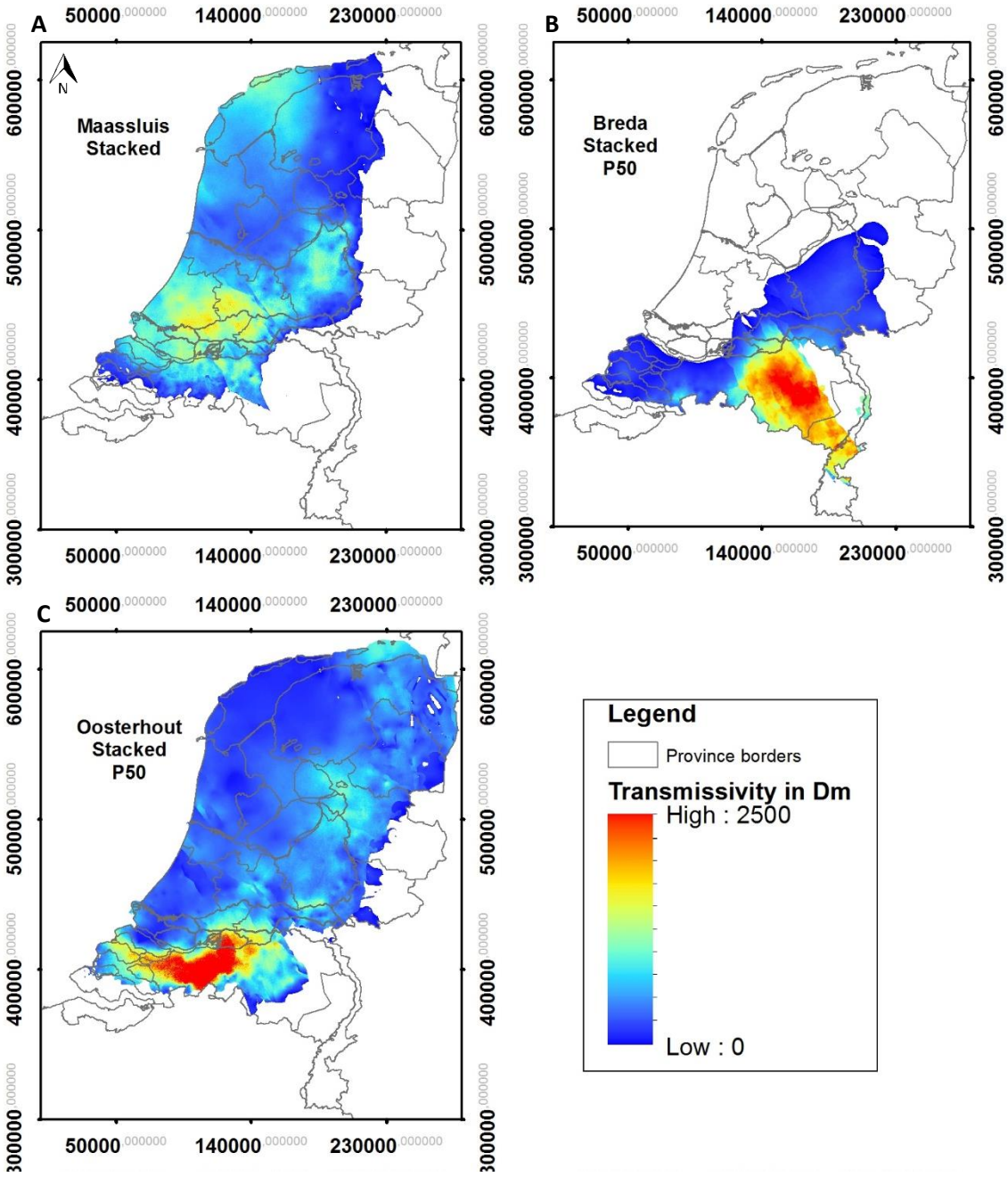

Fig. 15: These figures show P50 transmissivity maps for the stacked reservoirs of the Maassluis Formation, the Breda Formation and the Oosterhout Formation.

4.3 LEVELISED COSTS OF ENERGY

The maps that are shown in the following sections can be read in the following way. E.g. a P50 map shows that there is a 50% chance at a certain location that the investments for HT-ATES will be balanced when the energy is sold at a price of 3-4 EUR/GJ (LCOE). A P10 map then shows a lower LCOE, which is more favourable, while the chances of getting such a low LCOE is only 10%. The maps of the following section should therefore be interpreted in a similar way.

4.3.1 Delft Sandstone Member

The results from the LCOE calculations for P10 and P50 probabilities in the Delft Sandstone member (SLDND) are shown in Fig. 16. The LCOE distribution in the P10 map of the SLDND member is barely visible. In central Zuid-Holland a small area shows a LCOE between 3 and 5 EUR/GJ. The P50 map shows that the output LCOE grid incorporated values over a larger area, while generating higher LCOE values (>6 EUR/GJ). The area of the P50 map that does contain values appears to be similarly distributed to the values that can be seen in the map in Appendix B.3, which shows the depth of the SLDND aquifer up to 1500 m (Fig. 29).

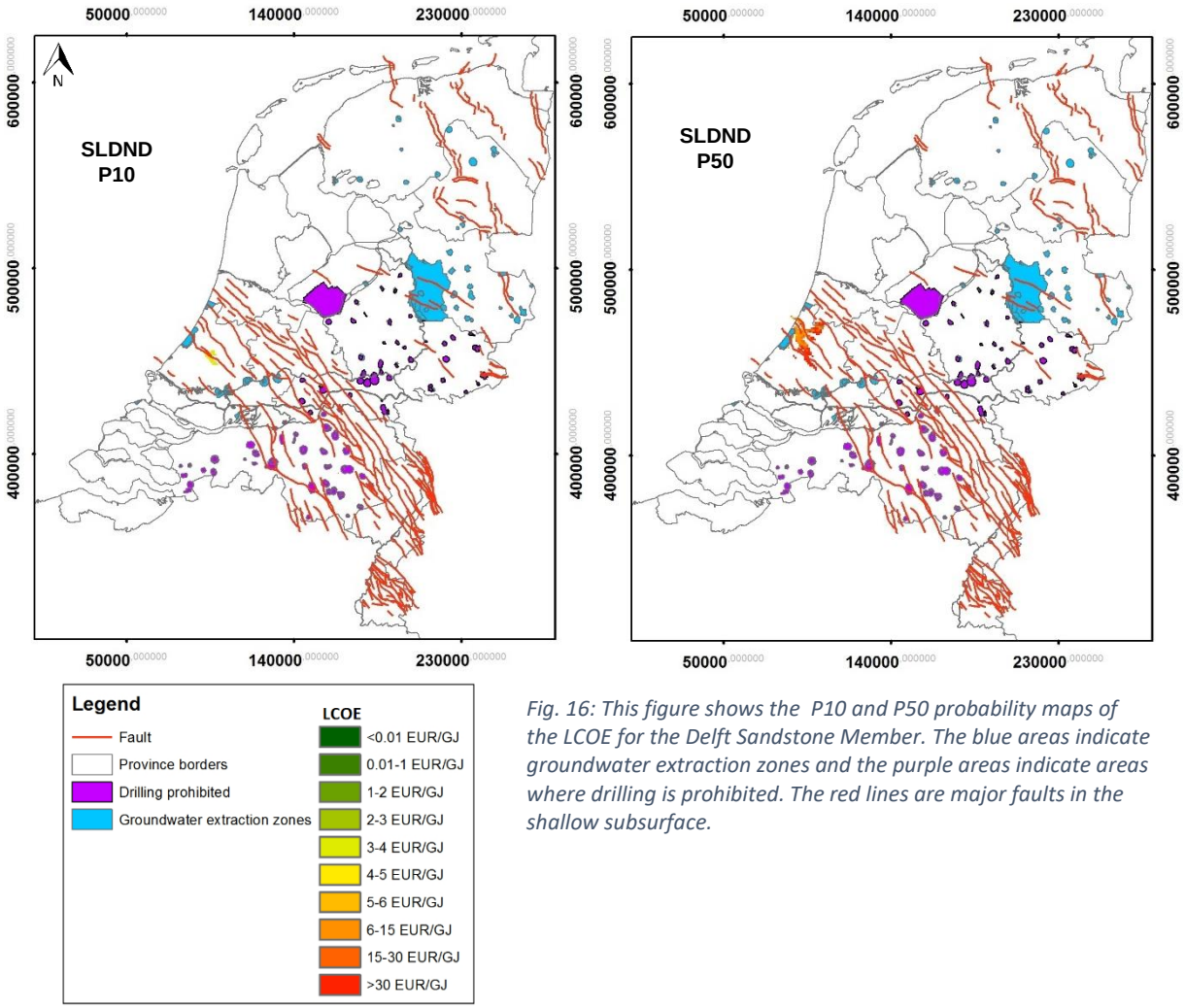

Fig. 16: This figure shows the P10 and P50 probability maps of the LCOE for the Delft Sandstone Member. The blue areas indicate groundwater extraction zones and the purple areas indicate areas where drilling is prohibited. The red lines are major faults in the shallow subsurface.

4.3.2 Rijnland Group

The LCOE maps of the Rijnland Group (Fig. 17) show lower values than the SLDND member. The P10 map indicates that, in parts of Zuid-Holland and southern Drenthe, there is a 10% probability that HT-ATES would need to cost between 3 and 5 EUR/GJ to balance the expenditures. The P50 map shows that there are more areas of interest for HT-ATES in the Rijnland Group. The LCOE however would be higher, with values ranging from 4 EUR/GJ to values higher than 30 EUR/GJ.

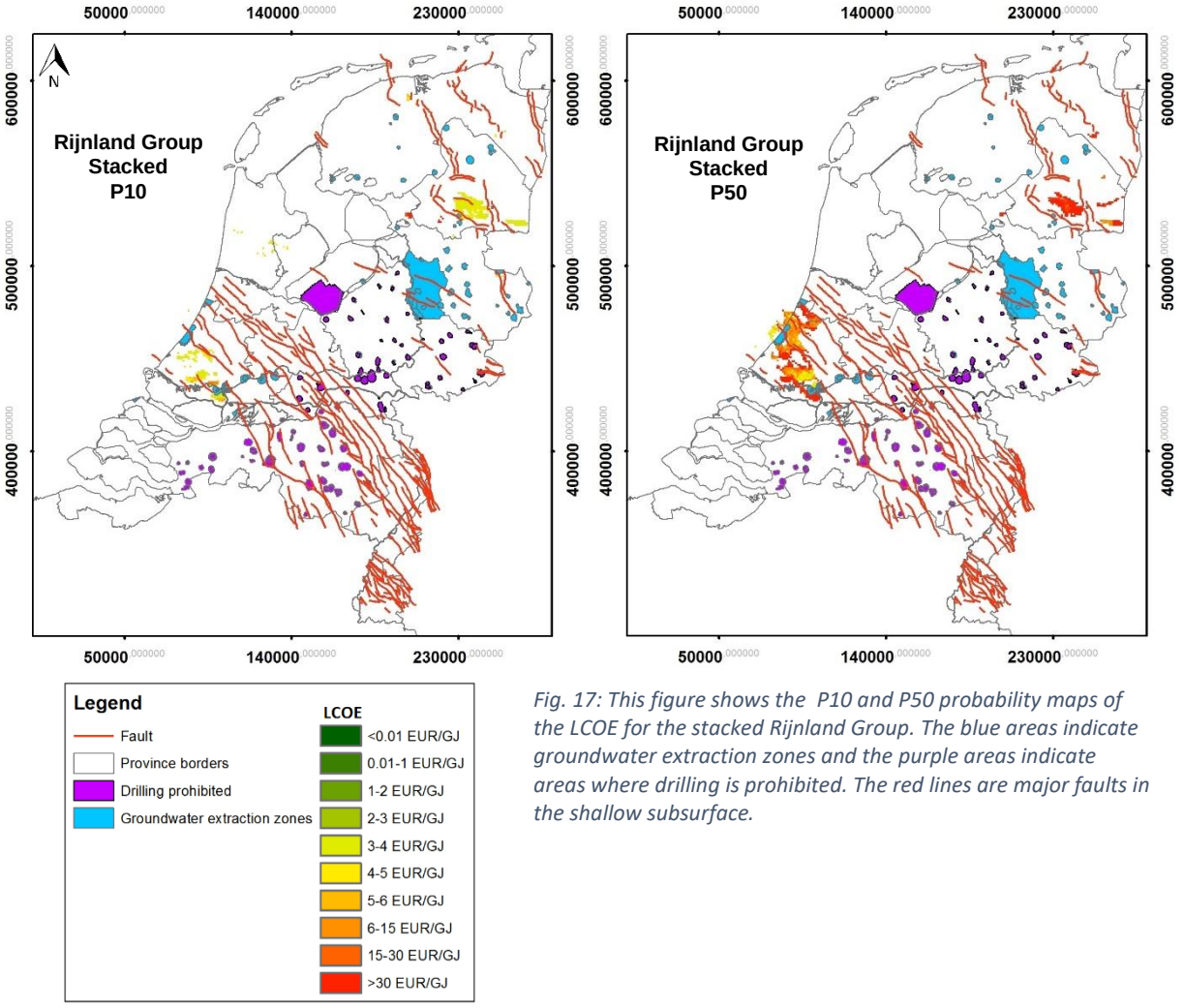

Fig. 17: This figure shows the P10 and P50 probability maps of the LCOE for the stacked Rijnland Group. The blue areas indicate groundwater extraction zones and the purple areas indicate areas where drilling is prohibited. The red lines are major faults in the shallow subsurface.

4.3.3 Lower and Middle North Sea Group

Fig. 18 shows the LCOE maps for the stacked Lower and Middle North Sea groups. The P10 map indicates there is a small probability that the LCOE for HT-ATES in the North Sea Group is between 3 and 6 EUR/GJ in parts of eastern Noord-Brabant and central Limburg. Higher values (>6 EUR/GJ) are given for certain parts of Flevoland, Friesland and the Waddenzee. A higher probability would be that HT-ATES in the North Sea Group would cost more than 6 EUR/GJ (see P50 map of Fig. 18) .

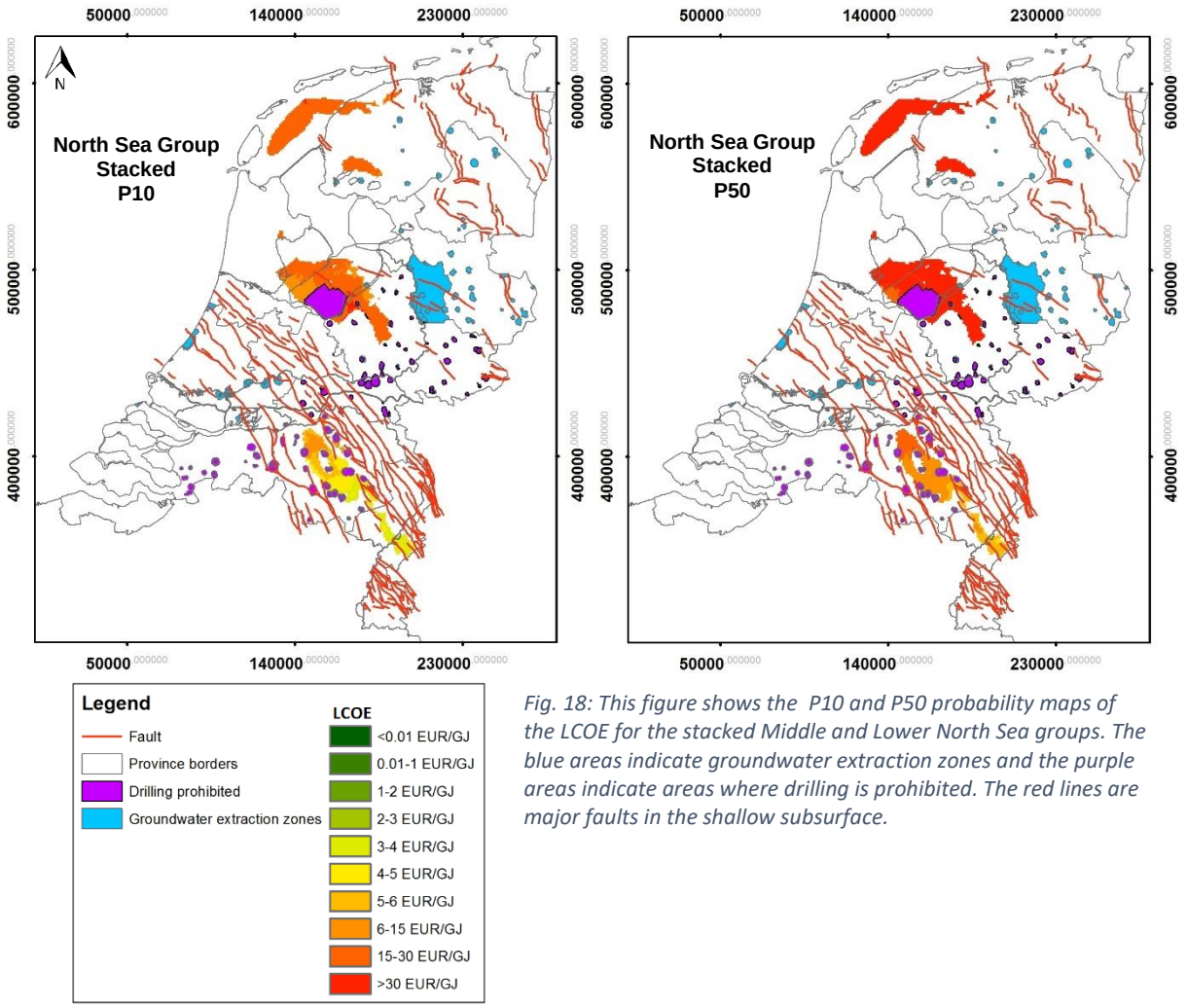

Fig. 18: This figure shows the P10 and P50 probability maps of the LCOE for the stacked Middle and Lower North Sea groups. The blue areas indicate groundwater extraction zones and the purple areas indicate areas where drilling is prohibited. The red lines are major faults in the shallow subsurface.

4.3.4 Breda Formation

In contrast with the deeper layers, HT-ATES in the Breda Formation would not cost as much (Fig. 19). The P10 map shows that the mean LCOE for HT-ATES in the Breda Formation lies between 2 and 3 EUR/GJ. The LCOE gradually increases toward the north eastern border of the Breda Formation. The northern part of Gelderland indicates LCOE values up to 15 EUR/GJ. The P50 map shows that the LCOE in and around the Roer Valley Graben remains low with values between 2 and 3 EUR/GJ, while it increases more in the areas that lie in Gelderland, eastern Utrecht, western Noord-Brabant and Zeeland. Sharp transitions in LCOE occur across faults, where reservoir properties abruptly change or thickness of reservoir and depth changes.

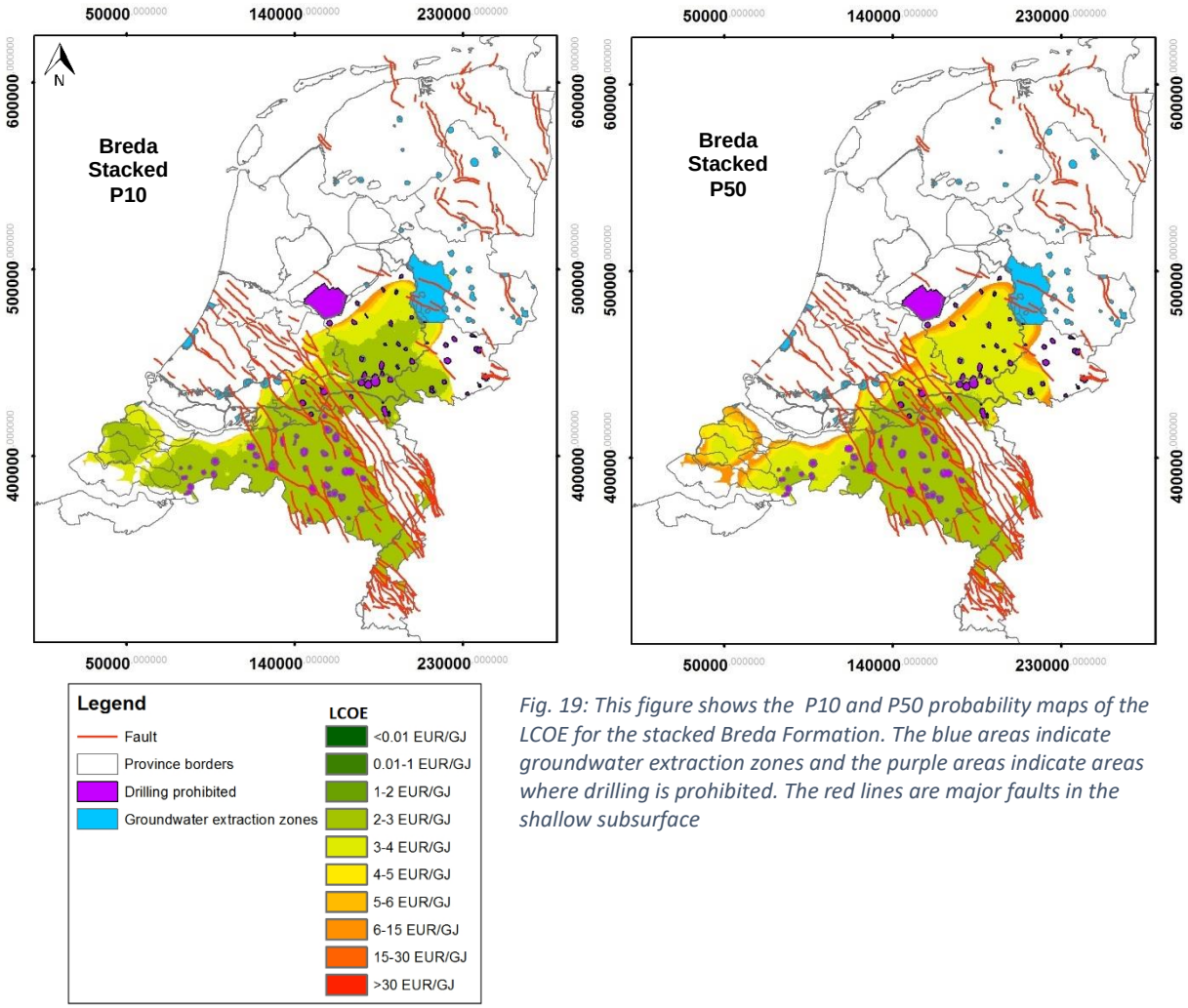

Fig. 19: This figure shows the P10 and P50 probability maps of the LCOE for the stacked Breda Formation. The blue areas indicate groundwater extraction zones and the purple areas indicate areas where drilling is prohibited. The red lines are major faults in the shallow subsurface

4.3.5 Oosterhout Formation

The LCOE for HT-ATES in the Oosterhout Formation are shown in Fig. 20. The P10 map shows a very favourable LCOE, with average values between 2 and 3 EUR/GJ. This map indicates that some areas in southern and northern Zuid-Holland, eastern Noord-Holland, the Waddenzee, north western Friesland and south eastern Drenthe have a higher LCOE (3-6 EUR/GJ). A higher possibility, but a less favourable outcome is shown in the P50 map. Here the LCOE in the western and eastern part of the Netherlands ranges between 3 and 6 EUR/GJ with some local exceptions where values reach 15 EUR/GJ. The central strip in the Netherlands that reaches from Groningen to Noord-Brabant is still very likely to get a low LCOE of 2 to 3 EUR/GJ.

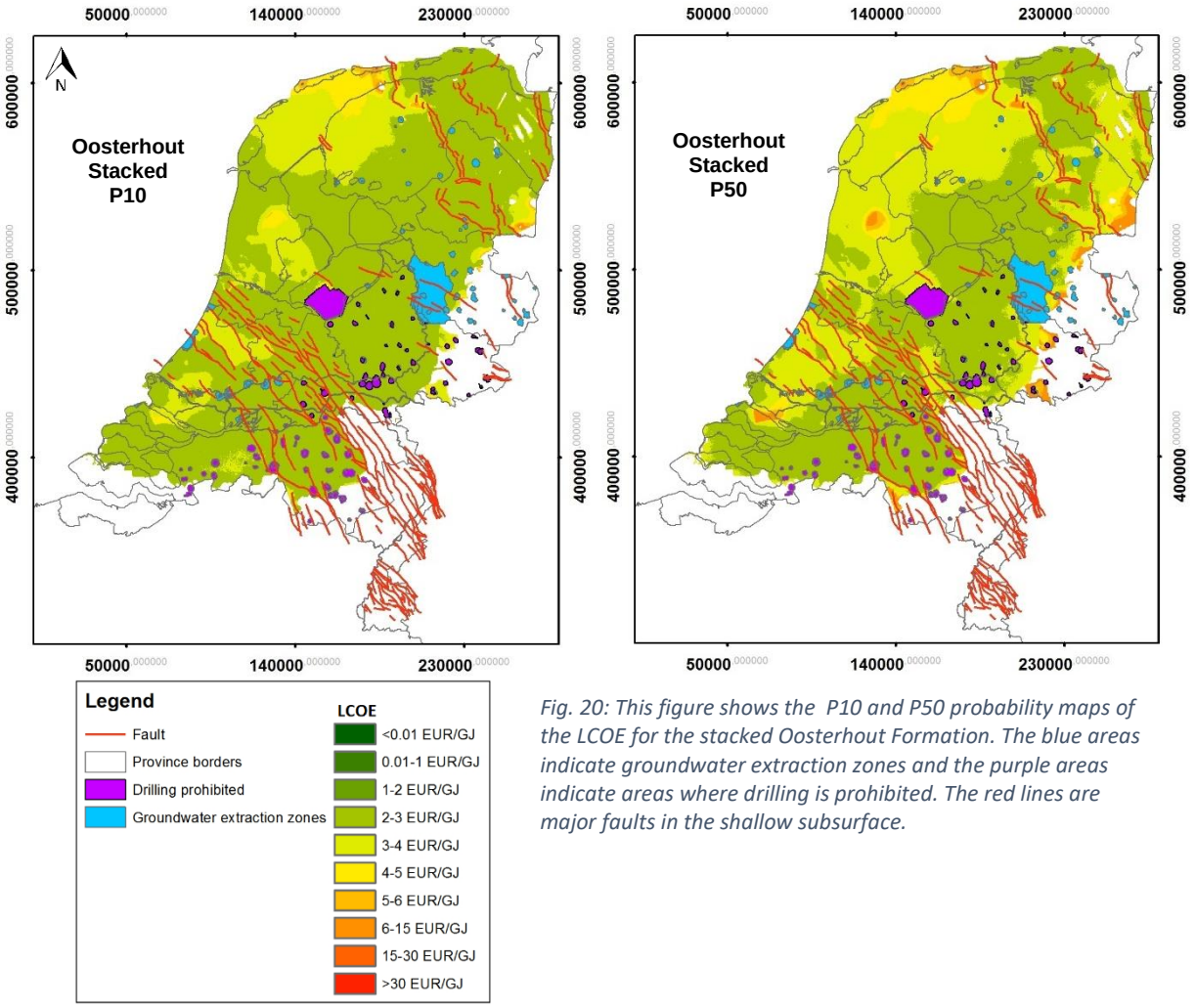

Fig. 20: This figure shows the P10 and P50 probability maps of the LCOE for the stacked Oosterhout Formation. The blue areas indicate groundwater extraction zones and the purple areas indicate areas where drilling is prohibited. The red lines are major faults in the shallow subsurface.

4.1.1 Maassluis Formation

The P10 LCOE map of the Maassluis Formation (shown in Fig. 21) indicates a favourable LCOE of 2-3 EUR/GJ for most of the area extent. An increase of LCOE up to 6 EUR/GJ can be found locally in the eastern part of Friesland. A more credible outcome would be the results shown in the P50 map in Fig. 21, where toward the southern and eastern borders of the Maassluis Formation the LCOE gradually increases up to 6 EUR/GJ. Parts in the north eastern part of the Maassluis Formation even show increases up to 15 EUR/GJ, which is a less favourable condition for HT-ATES.

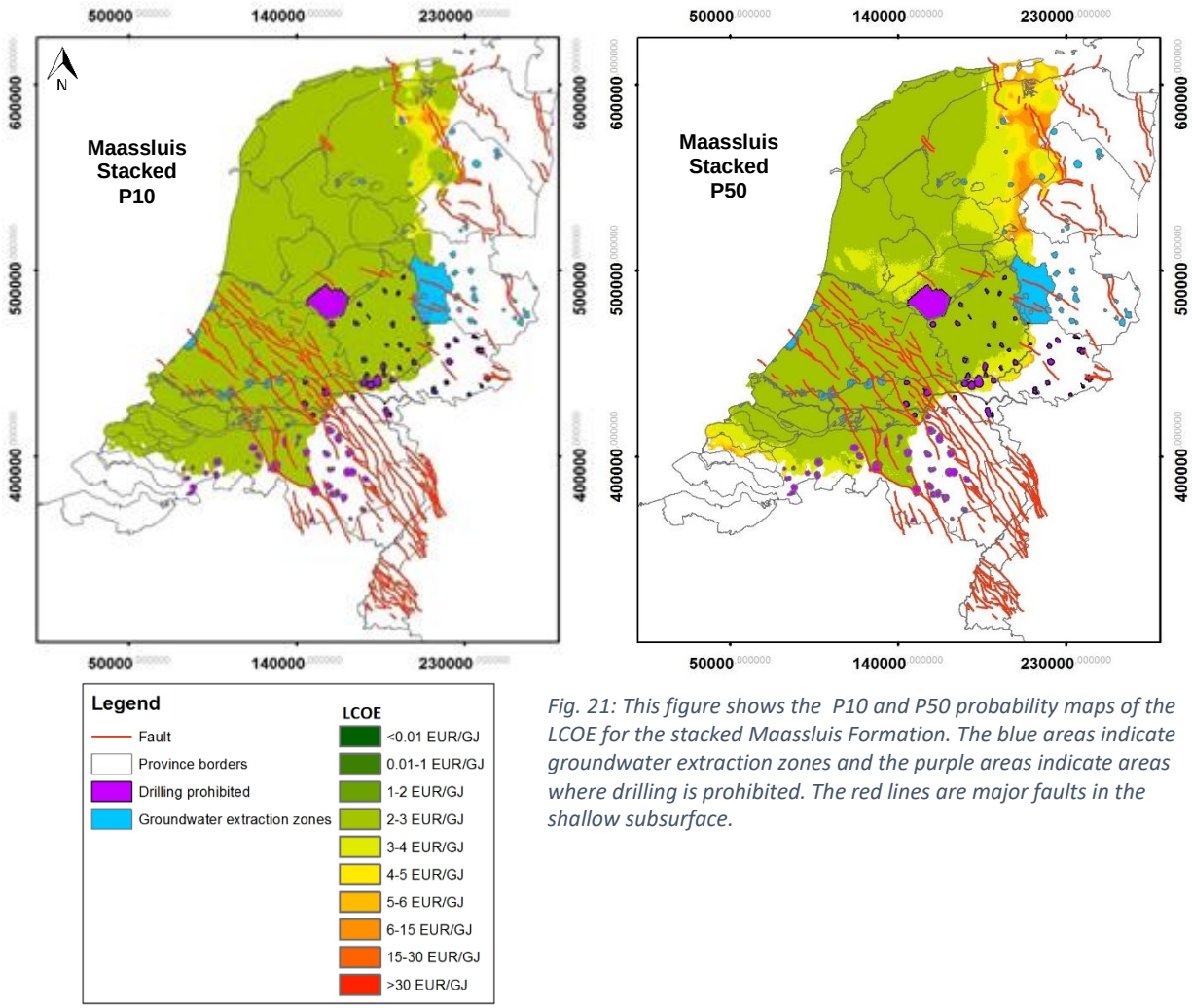

Fig. 21: This figure shows the P10 and P50 probability maps of the LCOE for the stacked Maassluis Formation. The blue areas indicate groundwater extraction zones and the purple areas indicate areas where drilling is prohibited. The red lines are major faults in the shallow subsurface.

5 DISCUSSION

With the global transition to a more sustainable and renewable future in mind, the Netherlands is investigating more ways to be more energy efficient. Although ATES has already proven to be a good method in providing energy storage, however it is not the most efficient way. HT-ATES could be a more efficient alternative, due to its higher enthalpy storage system. General lack of knowledge on the prospects of HT-ATES has refrained the government to move forward and invest in HT-ATES. This study aims to provide a first order insight into the potential of HT-ATES in the Netherlands by modelling the economic potential for HT-ATES in the Netherlands. In the following sections the major findings from the previous section are interpreted, the limitations of the study are discussed, and at last the recommendations for further research are made.

5.1 Sensitivity study on the recovery efficiency

As mentioned before, the recovery efficiency of HT-ATES is considered to be a major influence on the potential of such a system. The major processes that control the recovery efficiency are previously discussed by Schout et al. (2014) and Bakker (2009), and include thermal conduction, dispersion and density-driven flow (also referred to as “convection” or “buoyancy flow”). These processes are controlled by the following properties of the reservoir and parameters of the storage system: permeability, thickness, depth (which is relevant to the temperature and pressure, the flow

rate at which the stored water is injected and produced, thermal conductivity, thermal diffusivity and the time of injection, storage and production. Analysing the two methods that are used by Schout et al. (2014) and Bakker (2009), and comparing those results with the results from the numerical simulation with DoubletCalc3D, showed the magnitude of influence for the different properties and parameters.

5.1.1 Permeability

The results in section 4.1 showed that the recovery efficiency declines with increasing permeability. This is because flow increases with permeability and therefore making it easier for the buoyant (hot) injected water to flow to the top of the reservoir. This results in convection and thus energy losses. On the other hand, an increase in permeability is needed to decrease the pumping pressure needed to stimulate flow during the injection and production phase. This contradiction in the assessment of potential for HT-ATES makes it difficult to evaluate which range of permeability is best suited. The results from the sensitivity analyses could therefore be a guideline. The trends of the recovery efficiency of the reservoirs against the permeability are presented in Fig. 13B.

The Radial Dupuit Interface Flow calculations showed that the rate of change decreases with increasing permeability, similar to an exponential decay function. This is explained by the calculation for the D parameter that is shown in Eq. 19. Permeability is given to be inversely proportional to D, whereas a decrease in D also decreases the radial velocity of the interface (Eq. 20 & Eq. 21). This means that an increase in permeability deaccelerates the rotation of the interface, explaining the exponential decay of recovery efficiency with permeability.

The trend in Fig. 13B, from the Rayleigh-based method by Schout et al. (2014), shows a similar relation between the permeability and the recovery efficiency. Equations Eq. 24-Eq. 30 in section 3.4.3 show that the modified Rayleigh number increases with permeability. The recovery efficiency then relates to the permeability as an exponential decay function, where the B parameter is negative and A is positive (see Eq. 27). The same relation is also shown in the results from the DoubletCalc3D simulations. The difference between the three methods is therefore the rate of exponential decay of efficiency with permeability.

5.1.2 Thickness

The influence of thickness on the recovery efficiency for the different methods, which is given in Fig. 13C, appears to be almost non-existent for the Rayleigh-based method and the DoubletCalc3D simulation. While it shows that it has a large influence on the efficiency in the Radial Dupuit Interface Flow calculations. This large contribution can be explained by examining Eq. 19. Here the D parameter varies by the inverse square of the thickness, resulting in an even larger contribution than the permeability. The small variation of efficiency with thickness in the Rayleigh-based method, is due to the fact that the A and B parameters positively change the efficiency with increasing thickness. The contribution of Ra* is larger than the A and B parameters, however these parameters do significantly influence the rate at which the efficiency changes with thickness. From the results of the DoubletCalc3D simulations a similar trend can be identified, suggesting that the influence of thickness on recovery efficiency is not as drastic as the method of Bakker (2009) implies.

5.1.3 Depth

The variable depth is not significant on its own, with respect to calculating recovery efficiency of a HT-ATES system. It does however influence the reservoir temperature and pressure, resulting in changes in density, viscosity and heat capacity of the injected and in-situ groundwater. The influence of depth on these properties is however small, because all three methods show a small variation of efficiency with depth. The results from the DoubletCalc3D simulations show the largest changes,

while the Rayleigh-based results indicate a constant efficiency with varying depth. The calculations from Schout et al. (2014) assume an average temperature between that of the injected water and the in-situ water to calculate the density and viscosity. This causes the influence of temperature variations with depth of the in-situ water to decrease by half, explaining the lack of variation with depth from the Schout et al. (2014) results (see Fig. 13D).

5.1.4 Flow rate

The flow rate that is applied during injection and production phases of HT-ATES, has a positive influence on the recovery efficiency (see Fig. 13E). Higher flow rates, while maintaining the same injection and production periods, result in higher volumes to be injected into the reservoir. Van Lopik et al. (2016) suggests that the recovery efficiency of HT-ATES systems is proportional to the injected volume. Buoyancy flow would cause the volume of hot water to flow to the top of the reservoir. The ratio between outside contact area of the hot volume of water with the top confining layer and the thermal volume of hot water appeared to be smaller for larger volumes than for smaller volumes (Van Lopik et al, 2016). The heat loss by conduction into the overlying layer will therefore be proportionally larger for smaller volumes than for larger volumes. This effect can be seen with the DoubleCalc3D simulations and it is clear from the results of the other two methods that such a relationship between injected volume and efficiency could be considered.

5.1.5 Comparison of the different methods

Because the DoubletCalc3D software to simulate fluid flow in a 3D porous medium is validated to be quite accurate by Van Wees et al. (2012) and Buik (2014) , these results have been taken as an example to compare with the other methods. The simulations have a very long computational time and are therefore not suited to be incorporated directly in the Java model. The results from these simulations are therefore only used in comparison with the two faster methods that are derived from Bakker (2009) and Schout et al. (2014).

The method that is used by Bakker (2009) only focuses on the volumetric recovery efficiency, assuming that the thermal volume does not lose heat to the aquifer or confining layers. This method assumes energy loss by free convection to be the only controlling factor in HT-ATES system. The results from these calculations are generally lower than the efficiencies that result from the other two methods. This could be explained by the fact that the calculations that are defined by Bakker (2009) are designed to calculate the recovery efficiency of fresh water storage in brackish water reservoirs. In theory the buoyancy flow of a HT-ATES system works in a similar way. However it does not incorporate the heat loss of the injected thermal volume by conduction, changing the balance of the density difference between the injected and in-situ groundwater over time. In the finite difference scheme the production of the heated water also stops if the toe of the interface reaches the well (“cold water breakthrough”), resulting in a large body of hot water not being produced (see Fig. 9B). This could therefore explain the lower efficiencies, due to the large volume of hot water that remains in the reservoir during each cycle of storage.

The Rayleigh-based method from Schout et al. (2014) showed results that are very similar to the DoubletCalc3D simulations. Schout et al. (2014) assumed energy losses to be governed by thermal conduction and free convection. It gives a more accurate picture of the processes involved in the energy loss of HT-ATES, because the DoubletCalc3D simulations showed that heat loss to the confining layers and to the rock matrix is still significant. While the methods of Bakker (2009) and the DoubletCalc3D software do account for a HT-ATES system with a lifetime of 15 years, incorporating the influence of the injection periods, storage periods and production periods. Schout et al. (2014) came to the conclusion that varying the time of these periods has no significant influence on the

recovery efficiency. Doubling the injection/production period only resulted in a change of 2% in recovery efficiency, which is considered to be insignificant in contrast to the influence of the other parameters. The recovery efficiency that is calculated with this method represents the efficiency in the fourth year cycle, because their findings showed that the after more or less 4 years the recovery efficiencies appeared to stabilize and used this as a input/boundary condition for calculating recovery efficiency. This assumption differs from the methods used in the Radial Dupuit Interface Flow calculations and DoubletCalc3D to calculate the overall efficiency of a HT-ATES system, where the average efficiency over the lifetime of the HT-ATES system is calculated. This different method of calculating overall efficiency could therefore explain the small differences in efficiency between the resulting efficiencies of the Rayleigh-based method and DoubletCalc3D.

The Rayleigh-based method by Schout et al. (2014) showed the most promising results and gives a realistic picture of the physical processes involved with HT-ATES. Considering it requires the least amount of computational time, this method is thus implemented in the Java code that is used by this study to calculate the potential of HT-ATES in the Netherlands. Further research could be done through curve-fitting the calculations to the results of more test cases from DoubletCalc3D, in order to get the relation of average efficiency over the lifetime of a HT-ATES system.

5.2 POTENTIAL OF HT-ATES IN THE NETHERLANDS

The potential for HT-ATES is directly related to the LCOE, where a high LCOE makes it less attractive for developers to invest than a low LCOE. The categorization of the potential with respect to the LCOE is given in Table 6. The variation of the LCOE per reservoir in space mainly depends on three different subsurface properties of the reservoirs that include: the depth, the thickness and the permeability of the reservoir. The potential for HT-ATES is therefore directly linked to the spatial variations of these reservoir properties. The spatial variations in the potential for HT-ATES for the different reservoirs are discussed in the following sections (5.2.1-5.2.6).

The depth of the reservoirs has effect on a number of variables that include costs of production as well as efficiency of the HT-ATES system (as is discussed in the previous section 5.1). Deeper reservoirs have a negative influence on the Capex and Opex, because well costs are larger and more electricity is needed to drive the pumps. On the other hand, it increases the maximum allowable pressure, which results in a higher flow rate (injected volume). This increases efficiency, thus allowing more heat to be stored. This then increases the cumulative discounted energy sales and therefore increases the potential (decrease of LCOE). Furthermore, it decreases the temperature difference between the injected water and the ambient groundwater, resulting in smaller energy losses. Because most of the Lower and Middle North Sea groups, as well as the Delft Sandstone member and the Rijnland group, are located at depths greater than the cut-off depth at 1500m (see Appendix B.3), only small portions of these reservoirs are taken into account when plotting the LCOE maps. This cut-off depth has been proven to be an acceptable measure, because layers at depths greater than 1500 m give higher costs and lower flow rates due to the decrease in porosity and permeability. The assumption that there is no minimum cut-off depth is however not entirely correct. HT-ATES in very shallow reservoirs carry a higher risk of environmental interference. Because there is no spatial data available on what the minimum depth of an HT-ATES system should be, this study has not included this in the model restrictions. Depth maps are given in Appendix B.3 for further research on this minimum depth.

Variations in permeability and thickness mainly control the volume of water that can be stored and the pressures needed to drive flow. While higher permeabilities and thicknesses have a positive

effect on the amount of thermal energy that can be stored and on the pressures needed to drive this flow, they both have an negative effect on the recovery efficiency (see sections 5.1.1 and 5.1.2). As is shown in Eq. 7, the product of thickness and permeability is transmissivity. Transmissivity is a measure of how much water can be transmitted horizontally through a reservoir. Because variations in both the thickness and permeability have a similar relation to the changes in the LCOE, it is therefore useful to explain variations in LCOE with variations in terms of transmissivity.

5.2.1 Potential in the Delft Sandstone Member

The Delft Sandstone did not show a large potential for HT-ATES, this could be largely attributed to the large depths at which the reservoir is located and the very low permeability of the reservoir. The maximum cut-off depth at 1500 m that is taken in the Java model causes many grid points that are located at depths larger than 1500 m to not be considered in the calculations. The difference in area extent between the P10 and P50 LCOE maps can be explained by considering that the P10 map shows higher transmissivities than the P50 map. A higher transmissivity has a positive effect on the LCOE, as can be seen in Fig. 16. It also decreases the efficiency, which results in a lower COP. Less grid cells are then assigned values, due to the cut-off COP of values below 15. The P10 LCOE map therefore shows more potential (LCOE = 3-4 EUR/GJ) over a smaller area, while the P50 LCOE map shows less potential (LCOE > 6 EUR/GJ) over a larger area. The Delft Sandstone member is therefore not considered to be a feasible reservoir for implementing HT-ATES. It is however considered by different studies (Mottaghy et al., 2011; Salimi et al., 2011; Kramers et al., 2012) to be a potential reservoir for geothermal energy.

5.2.2 Potential in the Rijnland Group

The stacked Rijnland Group shows a better potential than the Delft Sandstone member. The Rijnland group reservoirs are less deep than the Delft Sandstone member, however still too deep for obtaining very low LCOE. The P10 map in Fig. 17 shows a very good potential for HT-ATES in certain parts of Noord-Holland and Drenthe, while the more probable P50 map shows moderate to very low potential over a larger area extent. This difference in area extent can be explained in the same way as has been done in the previous section (5.2.1), and is therefore contra-intuitively attributed to the higher transmissivities that are calculated by the Monte-Carlo sampling method with a P50 confidence level. The individual sandstone reservoirs that exist in the Rijnland group showed no potential and are therefore not presented in Appendix B. However, this indicates that a multiple point injection well will be needed to achieve the required transmissivities and thus a low LCOE. Even though it has a low potential for HT-ATES, it is considered by Kramers et al. (2012) to be a potential reservoir for geothermal energy production.

5.2.3 Potential in the Lower and Middle North Sea Group

The P10 LCOE map of the stacked Lower and North Sea groups (referred to in the map as the stacked North Sea group) showed very low potential in the northern reservoirs, while giving low to very good potential in the areas that lie in parts of Limburg and Noord-Holland. A part of southern Flevoland also shows a moderate potential, however it partially lies within an area that is restricted for drilling. The P50 map shows the same relations with small a uniformly increase of the LCOE. The LCOE P50 maps for individual layers, that are given in Appendix B.2 (Fig. 27), indicate a lower potential. The Voort member locally shows a low potential, while the other members of the Middle and Lower North Sea groups have very low potential. This indicates that stacking of individual layers needs to done in order to achieve moderate potentials.

5.2.4 Potential in the Breda Formation

The results of the Breda formation revealed a significantly higher potential for HT-ATES. This is mainly attributed to the shallower depth at which the reservoir can be found in combination with the high transmissivity values. The P10 map in Fig. 19 indicated that most of the stacked Breda formation showed a high potential, while the P50 map appeared to indicate high potentials in and around the Roer Valley Graben (parts of Limburg and Noord-Brabant), where the potential decreases to the west and north of the Roer Valley Graben.

The high potential in the Roer Valley Graben is due to the very thick depositions of the BRZ1 in this area (see Fig. 22). These thick depositions are the result of large amounts of subsidence in the Roer Valley Graben during the deposition of the BRZ1. The accommodation space for this thick deposition was created after the initial uplift of the Alpine Orogeny in a major rift zone. This thick deposition results in very high values of transmissivity and therefore a low LCOE. The sharp transitions in LCOE that can be seen at fault boundaries in Fig. 19, suggest that normal faulting created more accommodation space for deposition in certain areas than in others, resulting in sharp transitions in the thickness of the BRZ1 deposits. The decrease in potential toward the west and the north of the Roer Valley Graben can be explained by the decrease in thickness of the BRZ1 and decrease in depth, insinuating that a lower flow rate can be applied to a HT-ATES system in these regions. The BRZ1 has the largest contribution to the potential in the stacked Breda Formation, because this sand layer is distributed over a larger area than the remaining sand layers of the Breda Formation and would therefore be the most suited for HT-ATES.

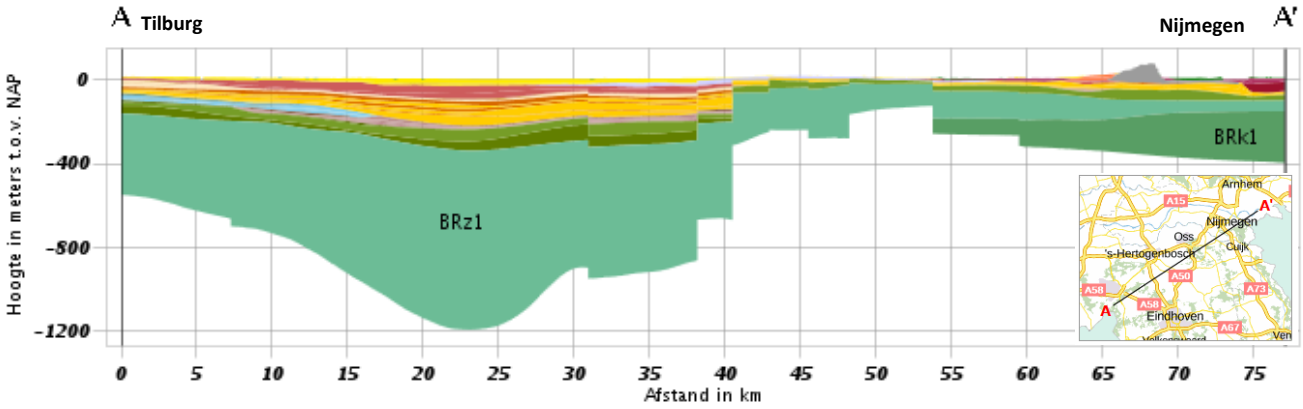

Fig. 22: This figure shows a cross section through the layers of the REGIS II v2.2 model, that extends from Tilburg to Nijmegen and crosscuts the Roer Valley Graben. The cross-section is retrieved from the website https://www.dinoloket.nl/ondergrondmodellen.

5.2.5 Potential in the Oosterhout Formation

The P10 LCOE map of the stacked Oosterhout Formation shows a very high potential for HT-ATES in the Netherlands. A higher probability would be that the western parts and the eastern border of the Oosterhout Formation would give higher LCOE's. A correlation can be made with the thickness of the OOZ2 layer and the decrease in potential in the western part, in the northern part (near Ameland) and at the eastern border of the stacked Oosterhout Formation(see Fig. 24 and Fig. 23). While the OOC layer increases in thickness in the western part of the cross section, it does not significantly influence the LCOE. This is likely because of the lower permeability of the complex layer. This complex layer consists of a strong alternation of less permeable clay stones and permeable sandstone, resulting in a lower average permeability than for example the OOZ2 (Ebbing & De Lang, 2003). The OOZ2 consists entirely of highly permeable sandstone. The OOZ2 layer can be considered a more feasible layer for HT-ATES than the OOC layer (see Appendix B1). However, the OOC layer is

distributed over a larger part of the Netherlands and it does display a moderate potential for HT-ATES. Both layers should therefore be considered for HT-ATES in further studies.

5.2.6 Potential in the Maassluis Formation

The stacked Maassluis Formation shows the most potential for HT-ATES. Both with a P10 and P50 confidence level, the results imply that there is a very high potential for HT-ATES in the Maassluis Formation. Its shallow depth and high permeability are the most logical explanation for this potential. The shallow depth decreases well costs, while the high transmissivity allows high flow rates to be exerted in the reservoir. The region of eastern Friesland shows an small decrease in potential, which is due to the decrease in thickness of the Maassluis sandstone layers towards the east of the formation (see Fig. 23). Each individual sandstone layer in the Maassluis Formation, except for the MSZ1 layer, gives a very high potential for HT-ATES (see Appendix B.1).This suggests that there is no need for a multiple point injection well. The MSC layer does give a lower potential in the eastern parts of Friesland, due to the decrease in thickness of this layer towards the east (see Fig. 24).

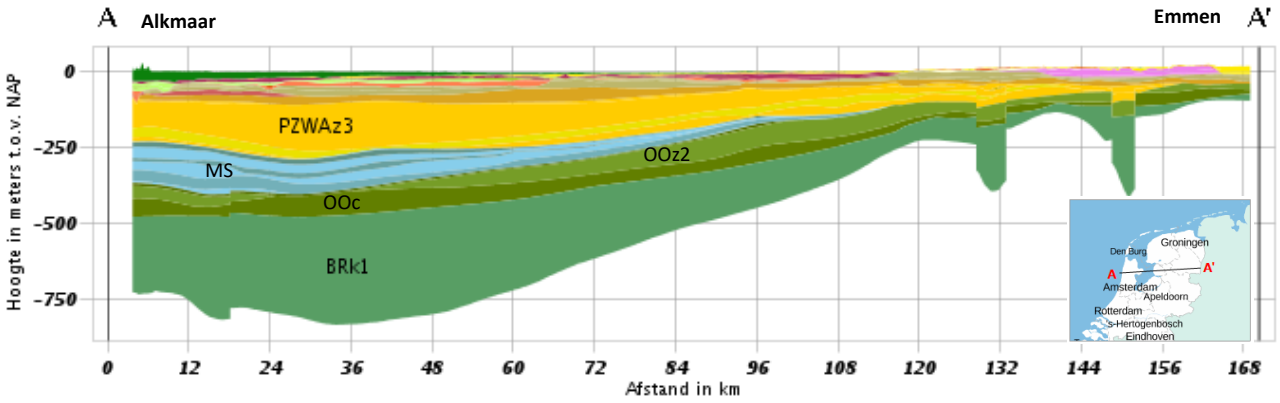

Fig. 24: This figure shows a cross section through the layers of the REGIS II v2.2 model, that extends west to east from Alkmaar to Emmen . It shows the thinning of the reservoirs toward the east. The cross-section is retrieved from the website https://www.dinoloket.nl/ondergrondmodellen

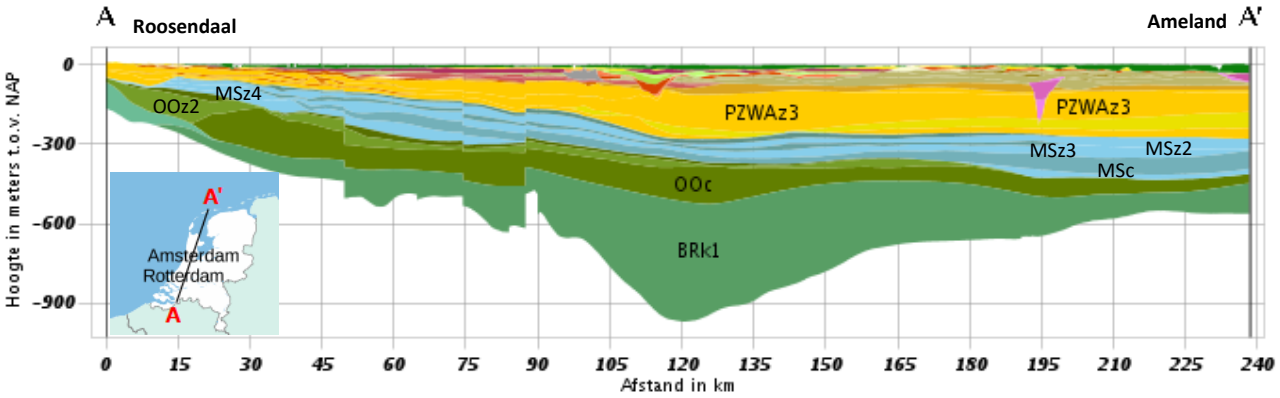

Fig. 23: This figure shows a cross section through the layers of the REGIS II v2.2 model, that extends from Roosendaal to Ameland and crosscuts the western part of the Netherlands. It shows the depth distribution of the Oosterhout and Maassluis formations. The cross-section is retrieved from the website https://www.dinoloket.nl/ondergrondmodellen

5.3 MODEL RESTRICTIONS

The Java model has produced promising results. There are however some restrictions in the model that have to be considered in the evaluation of the resulting potential maps for HT-ATES. Furthermore, the quality of the input data and the visualisation of the results are discussed here.

First a consideration needs to be made on the resolution of the data input. The ThermoGIS grids are lower with respect to the REGIS II v2.2 grids, where ThermoGIS has a horizontal resolution of 250x250 m and REGIS II v2.2. gives a resolution of 100x100 m. Considering the average area that is occupied by an HT-ATES system, the area of each grid cell roughly coincides with the approximate area that a HT-ATES system would occupy in the subsurface. This is based upon the general assumption that the average injection rate is 100 m^3/hour for an injection period of 3000 hours and a porosity of 0.3 and a reservoir thickness of 100 m. With the consideration of a homogeneous subsurface in every grid cell, the resolution of the ThermoGIS and REGIS II v2.2 grids is acceptable for the aims of this study. It is however necessary to study the subsurface with a higher resolution in order to confirm these results.

This study assumed that the reservoir temperature could be calculated, by considering that the subsurface of the Netherlands has a constant homogeneous thermal gradient. This assumption is based on a calculation by Bonte et al. (2012) of the average thermal gradient of the Netherlands. Bonté et al. (2012) also developed a 3D temperature model of the subsurface of the Netherlands. The results from their study showed large spatial variations in temperature at depths of 2000-4000 m, while the variations in temperature at shallow depths (1000 m) where relatively small. Due to the small spatial variations in temperature at depths suitable for HT-ATES, and considering the increase in computational time when a 3D temperature model is inserted into the Java model, the assumption of a constant thermal gradient is considered to be sufficient for a first approximation of the recovery efficiency of a HT-ATES system. If a certain location is being considered, an in-depth analysis of the thermal structure of the subsurface is needed. This is due to the large influence of heterogeneities in reservoir temperatures on the groundwater flow.

The assumption that the rock density and pressure gradient are constant is not entirely correct. The different lithologies that are described in the book of Wong et al. (2007) and in section 2.2, already give an impression that there is no homogeneous subsurface. Salinity of groundwater as well as rock porosity are not constant and need to be measured from borehole data and hydrogeological measurements. Drijver (2011) indicated the risks of clogging of wells due to carbonate precipitation. The clogging of wells can be included in the calculations of the Java model as the skin of the well, where it influences the maximum applicable flow rate that can be exerted on the reservoir. The assumption of this skin factor being zero is therefore not reasonable. While there are some methods that can prevent this process, these processes also have disadvantages. More research has to be done on the influences of clogging, in order to make an appropriate estimate on the pressure losses due to clogging.

5.4 RECOMMENDATIONS FOR HT-ATES AND FURTHER RESEARCH

The sensitivity study showed several relationships between certain reservoir properties and efficiency. The number of test cases is however too limited to fully grasp the influences that these properties have on the recovery efficiency of a HT-ATES system. Further research is therefore needed to get a better idea on these influences and in order to predict the behaviour of the water during storage. Further research on the recovery efficiencies of the HT-ATES system, by curve fitting

the Rayleigh-based analytical solutions to the DoubletCalc3D numerical simulations, will improve the accuracy of the assessment that has been done by the Java model.

This study provided the means for a first approximation of the potential of HT-ATES in the Netherlands, using a business case where a geothermal doublet provides energy in the form of hot water for storage and where the stored energy can be directly applied to a district heating network. The cost of this energy supply is not included and would need to be assessed independently from this study for every location that is considered. The results of this study showed that HT-ATES has more potential in the shallow subsurface than in the deeper subsurface. The Upper North Sea Group reservoirs that are considered in this study show the most potential, confirming previous assessments of HT-ATES in the Netherlands (Koornneef et al., 2015; Drijver, 2014; Pluymaekers et al., 2013). The aquifers in the Breda Formation, Oosterhout Formation and Maassluis Formation are most suited for HT-ATES, due to the shallow depths, thick depositions and high permeabilities that exist within these formations.

If the results from this study are used for further research on the possibility of HT-ATES in the Netherlands, it is recommended that an in-depth analysis is done on the reservoir. Further research on the specific properties and regional ground water flow conditions will be needed in order to make a second-order approximation of the potential. Effects of high temperature storage on the bio-chemical reactions in the ground water system and interferences with groundwater production need to be studied, in order to assess the risk of a HT-ATES system. The legal restrictions that are in place in the Netherlands at the moment only allow pilots to be done with respect to high temperature storage in the shallow subsurface(Koornneef et al., 2015). It is therefore crucial to do an exploratory drilling at potential locations to study the subsurface conditions and make a more accurate assessment of the potential for HT-ATES. The results of this study are therefore desired to help with the selection of the best aquifer and/or location for HT-ATES, so that such a location for exploration can be predetermined.

6 CONCLUSIONS

This study has successfully assessed the potential of HT-ATES in the Netherlands, using 3D subsurface models of the Netherlands to calculate the performance of the HT-ATES system. It then used a business case, where heat is supplied from a geothermal well, in order to assess the economic potential. These results are desired to give a clear view for potential investors into HT-ATES, where HT-ATES could be a promising solution for achieving a more energy efficient future.

The findings of the sensitivity study on recovery efficiency suggested that several variable reservoir properties have a profound effect on the recovery efficiency of HT-ATES. Permeability was found to be the largest contributor to the recovery efficiency, whereas flow rate, depth and thickness had relatively small effects on the recovery efficiency. Using the numerical simulation software for hydrogeological research on reservoirs DoubletCalc3D as a benchmark calculation for analysing two different methods, this study has found a computationally faster method for estimating the recovery efficiency. This method is called the Rayleigh-based method (developed by Schout et al., 2014), where a modified Rayleigh number showed an exponential relation to the recovery efficiency. It assumes energy losses due to convection, conduction and dispersion. The main disadvantage of this method is that it is not time-dependent, assuming that efficiency of the fourth year cycle is equivalent to the overall efficiency. The Radial Dupuit Interface Flow method estimated very low efficiencies with some exceptional highs. While the method did incorporated injection, storage and production times into the equation, it assumed convection to be a contributor to energy loss and production to stop when the interface between the cold and hot water reached the well. These assumptions led to a large body of hot water not being tapped, giving an explanation to the low efficiencies. The Rayleigh-based method was thus implemented in the Java code for calculating the economic potential.

The main results of the economic potential in the Netherlands showed that the deeper SLDND, KN and N group reservoirs are not desirable for HT-ATES with some local exceptions. The shallower reservoirs from the Breda, Oosterhout and Maassluis formations on the other hand showed very promising results. Within the Breda formation, the area in and around the Roer Valley Graben showed the highest potential due to the thick depositions, whereas it decreases towards the north and west of this area. The Maassluis and Oosterhout formations generally show a very good potential, where in some places there is no need for stacking to achieve sufficient transmissivities and therefore individual aquifers within the formation are satisfactory. It has to be denoted that the probability of these potential maps vary, with a higher probability indicating a less favourable outcome than a lower probability.

Some restrictions to the overall geophysical model were made, because either there was insufficient data or computational time would exceed a set limit when implemented. These assumptions were considered to be acceptable within the boundaries of this study. Further research on curve-fitting the Rayleigh-based method with other numerical models could improve the assessment of the recovery efficiency of a HT-ATES system. The first order approximation that is done by this study is intended to give investors a first look at the economic prospects of HT-ATES in the Netherlands. If an exploratory drilling is pursued, further research on the specific reservoir properties and ground water flow conditions will be needed to make a more precise estimate of the potential. The environmental risks of HT-ATES in the shallow subsurface would need to be assessed.

ACKNOWLEDGEMENTS

First I would like to thank Jan-Diederik van Wees for giving me the opportunity to do my Master Thesis research at TNO and for the supervision during my research. I would like to give special thanks to Hans Veldkamp for the support and help with the data acquisition and visualisations. I would like to thank Maarten Pluymaekers and Mark Vrijlandt for helping me understand the existing Java code and DoubletCalc3D software. I would also like to thank Joris Koornneef for the discussions we had on the economic framework of HT-ATES systems. Finally I would like to thank Fred Beekman for guiding me throughout my research.

LIST OF REFERENCES

Bakker, M. (2009). Radial Dupuit interface flow to assess the aquifer storage and recovery potential of saltwater aquifers. *Hydrogeology journal*, *18*(1), 107-115.

Bakr, M., van Oostrom, N., & Sommer, W. (2013). Efficiency of and interference among multiple Aquifer Thermal Energy Storage systems; A Dutch case study. *Renewable energy*, *60*, 53-62.

Beggs, D. H., & Brill, J. P. (1973). A study of two-phase flow in inclined pipes. *Journal of Petroleum technology*, *25*(05), 607-617.

Bonté, D., Van Wees, J. D., & Verweij, J. M. (2012). Subsurface temperature of the onshore Netherlands: new temperature dataset and modelling. *Netherlands Journal of Geosciences*, *91*(4), 491-515.

Bonte, M., Stuyfzand, P., Hulsmann, A., & Van Beelen, P. (2011). Underground thermal energy storage: environmental risks and policy developments in the Netherlands and European Union. *Ecology and Society*, *16*(1).

Buik, N. (2014, June). A Practical Method to Calculate the Productivity of a Horizontal Well for a Geothermal Project in the Netherlands. In *76th EAGE Conference and Exhibition 2014*.

Cash, J. R., & Karp, A. H. (1990). A variable order Runge-Kutta method for initial value problems with rapidly varying right-hand sides. *ACM Transactions on Mathematical Software (TOMS)*, *16*(3), 201-222.

Central Bureau for Statistics (2015, 9 October). *Use geothermal heat doubled in the past 5 years.* Retrieved from the CBS website: https://www.cbs.nl/en-gb/news/2015/41/use-geothermal-heat-doubled-in-the-past-5-years

Central Bureau for Statistics (2016, 16 September). *Aardgas voor bijna 80 procent op.* Retrieved from the CBS website: https://www.cbs.nl/nl-nl/nieuws/2016/37/aardgas-voor-bijna-80-procent-op

Central Bureau for Statistics. (2017, 9 March) *Emissies van broeikasgassen berekend volgens IPCC-voorschriften*. Retrieved from the CBS website: http://statline.cbs.nl/Statweb/publication/?VW=T&DM=SLNL&PA=70946ned&D1=0&D2=0&D3=a&HD=170703-1038&HDR=T&STB=G1,G2

De Gans, W. (2007). Quarternary. In: Wong, Th.E., Batjes,D.A.J. & De Jager, J. (eds): *Geology of the Netherlands*. Royal Netherlands Academy of Arts and Sciences (Amsterdam): 173-195.

De Jager, J. (2007). Geological development. In: Wong, Th.E., Batjes,D.A.J. & De Jager, J. (eds): *Geology of the Netherlands*. Royal Netherlands Academy of Arts and Sciences (Amsterdam): 5-26.

Drijver, B. (2011, October). High temperature aquifer thermal energy storage (HT-ATES): water treatment in practice. In *Nationaal Congres Bodemenergie Proceedings*.

Drijver, B. (2014). Thermisch rendement hoge & middelhoge temperatuur warmteopslag in de bodem. IF Technology. Retrieved from the website https://www.kasalsenergiebron.nl/content/user_upload/MTO_en_HTO.pdf.

Duin, E. J. T., Doornenbal, J. C., Rijkers, R. H. B., Verbeek, J. W., & Wong, T. E. (2006). Subsurface structure of the Netherlands-results of recent onshore and offshore mapping. *Netherlands Journal of Geosciences*, *85*(4), 245.

Ebbing, J. H. J, & De Lang, F. D., (2003). *Formatie van Oosterhout.* In: Lithostratigrafische Nomenclator van de Ondiepe Ondergrond. Retrieved from https://www.dinoloket.nl/formatie-van-oosterhout

Furui, K. (2004). *A comprehensive skin factor model for well completions based on finite element simulations* (Doctoral dissertation).

Geluk, M.C. (2007a). Permian. In: Wong, Th.E., Batjes,D.A.J. & De Jager, J. (eds): *Geology of the Netherlands*. Royal Netherlands Academy of Arts and Sciences (Amsterdam): 63-83.

Geluk, M.C. (2007b) Triassic. In: Wong, Th.E., Batjes,D.A.J. & De Jager, J. (eds): *Geology of the Netherlands*. Royal Netherlands Academy of Arts and Sciences (Amsterdam): 85-106.

Geluk, M.C., Dusar, M., & De Vos, W.(2007). Pre-Silesian. In: Wong, Th.E., Batjes,D.A.J. & De Jager, J. (eds): *Geology of the Netherlands*. Royal Netherlands Academy of Arts and Sciences (Amsterdam): 27-42.

Goovaerts, P. (1997). *Geostatistics for natural resources evaluation*. Oxford University Press on Demand.

Groenenberg, R. M., Gilding, D. T., Donselaar, M. E., Drost, G. I. A., Korenromp, M. H. A., Loerakker, M., ... & Wolf, K. A. A. (2010, June). Targeting for Geothermal Energy Production–Reservoir Characterization and Geothermal Potential of the Delft Sandstone. In *72nd EAGE Conference and Exhibition incorporating SPE EUROPEC 2010*.

Gunnink, J. J., Maljers, D., & Hummelman, J. (2010). Quantifying uncertainty of geological 3D layer models, constructed with a-priori geological expertise.

Gunnink, J. L., Maljers, D., Van Gessel, S. F., Menkovic, A., & Hummelman, H. J. (2013). Digital Geological Model (DGM): a 3D raster model of the subsurface of the Netherlands. *Netherlands Journal of Geosciences*, *92*(1), 33-46.

Hellström, G., Tsang, C. F., & Claesson, J. (1988). Buoyancy flow at a two-fluid interface in a porous medium: Analytical studies. *Water Resources Research*, *24*(4), 493-506.

Herngreen, G.F.W., & Wong, Th.E. (2007). Cretaceaous. In: Wong, Th.E., Batjes,D.A.J. & De Jager, J. (eds): *Geology of the Netherlands*. Royal Netherlands Academy of Arts and Sciences (Amsterdam): 127-150.

Hewitt, D. R., Neufeld, J. A., & Lister, J. R. (2014). High Rayleigh number convection in a three-dimensional porous medium. *Journal of Fluid Mechanics*, *748*, 879-895.

Huizer, J., & Weerts, H. J. T. (2003). *Formatie van Maassluis.* In: Lithostratigrafische Nomenclator van de Ondiepe Ondergrond. Retrieved from https://www.dinoloket.nl/formatie-van-maassluis

Iheanacho, P. C., Tiab, D., & Igbokoyi, A. O. (2012, January). Vertical-Horizontal permeability relationships for sandstone reservoirs. In *Nigeria Annual International Conference and Exhibition*. Society of Petroleum Engineers.

Isaaks, E. H., & Srivastava, R. M. (1989). An introduction to applied geostatistics: Oxford Univ. Press.

Kalkman, A., Veldkamp, J. G., Boxem, T., Koornneef, J. M., Halter, M.(2016). *Ultra-Diepe Geothermie, Casus Almere en Barendrecht*(Report nr. 060.20102). Dutch Institute for Applied Geosciences, TNO. Retrieved from the website: https://geothermie.nl/images/Handboeken/BIA_UDG_Eindrapport_Final%20v1.1%20(28.9.2016).pdf

Knotters, M., Brus, D. J., & Voshaar, J. O. (1995). A comparison of kriging, co-kriging and kriging combined with regression for spatial interpolation of horizon depth with censored observations. *Geoderma*, *67*(3-4), 227-246.

Koornneef, J. M., Hanegraaf, M.(2016). *Hoge temperatuur opslag*[Powerpoint slides]. Retrieved from https://www.slideshare.net/AmsterdamEconomicBoard/presentatie-hoge-temperatuur-opslag?from_action=save

Koornneef, J., Griffioen, J., Pluymaekers, M., & Boxem, T. (2015). Technische en Juridische belemmeringen Hoge Temperatuuropslag (HTO) (Report nr. R11616). Dutch Institute for Applied Geosciences, TNO.

Kramers, L., Pluymeakers, M.P.D. (2013). *ThermoGIS V1.2 User Manual*. Dutch Institute of Applied Geosciences, TNO. Retrieved from the ThermoGIS website: http://www.thermogis.nl/downloads/ThermoGISmanual_EN.pdf

Kwadijk, J. C., Haasnoot, M., Mulder, J. P., Hoogvliet, M., Jeuken, A., van der Krogt, R. A., ... & de Wit, M. J. (2010). Using adaptation tipping points to prepare for climate change and sea level rise: a case study in the Netherlands. *Wiley interdisciplinary reviews: climate change*, *1*(5), 729-740.

Lee, K. S. (2010). A review on concepts, applications, and models of aquifer thermal energy storage systems. *Energies*, *3*(6), 1320-1334.

Mottaghy, D., Pechnig, R., & Vogt, C. (2011). The geothermal project Den Haag: 3D numerical models for temperature prediction and reservoir simulation. *Geothermics*, *40*(3), 199-210.

NAM and RGD (Nederlandse Aardolie Maatschappij and Rijks Geologische Dienst) (1980). *Stratigraphic nomenclature of the Netherlands*.. In: Verh. Kon. Ned. Geol. Mijnbouwk. Gen., 32, 77 pp.

Paalvast, L., van Thienen-Visser, K. (2014) Handleiding geomechanische tool breukreactivatie en fracken bij aardwarmtewinning (Report nr. R11062). Dutch Institute for Applied Geosciences, TNO. Retrieved from http://nlog.nl/tools.

Pluymaekers, M. P. D., Kramers, L., Van Wees, J. D., Kronimus, A., Nelskamp, S., Boxem, T., & Bonté, D. (2012). Reservoir characterisation of aquifers for direct heat production: Methodology and screening of the potential reservoirs for the Netherlands. *Netherlands Journal of Geosciences*, *91*(4), 621-636.

Pluymaekers, M. P. D., van Wees, J. D. A. M., van der Kuip, M., Vandeweijer, V. (2013). *Hoge temperatuur opslag in de ondiepe ondergrond*(Report nr. R11694). Dutch Institute for Applied Geosciences, TNO. Retrieved from the website: http://www.kennisplatformbodemenergie.nl/wp-content/uploads/2016/03/HTO-Hoge-temperatuuropslag-in-de-ondiepe-ondergrond.pdf

Press, W. H., Teukolsky, S. A., Vetterling, W. T., & Flannery, B. P. (1988). *Numerical recipes in C: The art of scientific computing,* . Cambridge: Cambridge university press.

Romeo, E., Royo, C., & Monzón, A. (2002). Improved explicit equations for estimation of the friction factor in rough and smooth pipes. *Chemical engineering journal*, *86*(3), 369-374.

Salimi, H., Groenenberg, R., & Wolf, K. H. (2011, January). Compositional flow simulations of mixed CO2-water injection into geothermal reservoirs: geothermal energy combined with CO2 storage. In *36th Workshop on Geothermal Reservoir Engineering, Stanford University* (pp. 169-181).

Sanner, B., & Knoblich, K. (1999). Advantages and problems of high temperature underground thermal energy storage. *Bull. Hydrogeol*, *17*, 341-348.

Sommer, W., Rijnaarts, H., Grotenhuis, T., & van Gaans, P. (2012, April). The effect of soil heterogeneity on ATES performance. In *EGU General Assembly Conference Abstracts* (Vol. 14, p. 9724).

Van Adrichem Boogaert, H. A., & Kouwe, W. F. P. WFP 1993–1997. *Stratigraphic nomenclature of the Netherlands; revision and update by RGD and NOGEPA*. Retrieved from the Dinoloket website: www.dinoloket.nl

Van Buggenum, J.M., & Den Hartog Jager, D.G. (2007). Silesian. In: Wong, Th.E., Batjes,D.A.J. & De Jager, J. (eds): *Geology of the Netherlands*. Royal Netherlands Academy of Arts and Sciences (Amsterdam): 43-62.

van Lopik, J. H., Hartog, N., & Zaadnoordijk, W. J. (2016). The use of salinity contrast for density difference compensation to improve the thermal recovery efficiency in high-temperature aquifer thermal energy storage systems. *Hydrogeology Journal*, *24*(5), 1255-1271.

van Wees, J. D. A. M., Kramers, L., Kronimus, R. A., Pluymaekers, M. P. D., MijnLieff, H. F., & Vis, G. J. (2010). *ThermoGIS TM V1. 0 Part II: Methodology.* Dutch Institute for Applied Geosciences, TNO. Retrieved from ThermoGIS website: http://thermogis.nl/downloads/ThermoGISmanual_partII.pdf

Van Wees, J. D., Kronimus, A., Van Putten, M., Pluymaekers, M. P. D., Mijnlieff, H., Van Hooff, P., ... & Kramers, L. (2012). Geothermal aquifer performance assessment for direct heat production–Methodology and application to Rotliegend aquifers. *Netherlands Journal of Geosciences*, *91*(4), 651-665.

Veldkamp, J. G., Pluymaekers, M. P. D., & van Wees, J. D. A. M. (2015). *DoubletCalc 2D 1.0 User Manual*. Dutch Institute for Applied Geosciences, TNO. Retrieved from ThermoGIS website: http://www.thermogis.nl/downloads/TNO%202015%20R10216%20Manual%20DoubletCalc%202D%20v1.0_20151104.pdf

Vernes, R. W., Van Doorn, T. H., Bierkens, M. F. P., Van Gessel, S. F., & de Heer, E. (2005). *Van gidslaag naar hydrogeologische eenheid: toelichting op de totstandkoming van de dataset REGIS II*. Nederlands Instituut voor Toegepaste Geowetenschappen TNO.

Verruijt, A. (1970). Theory of Groundwater Flow. *Macmillan(London), 190.*

Westerhoff, W.E. (2003). *Formatie van Breda.* In: Lithostratigrafische Nomenclator van de Ondiepe Ondergrond. Retrieved from https://www.dinoloket.nl/formatie-van-breda

Wong, Th.E. (2007). Jurassic. In: Wong, Th.E., Batjes,D.A.J. & De Jager, J. (eds): *Geology of the Netherlands*. Royal Netherlands Academy of Arts and Sciences (Amsterdam):107-125.

Wong, Th.E., De Lugt, I.R., Kuhlmann, G., & Overeem, I. (2007). Tertiary. In: Wong, Th.E., Batjes,D.A.J. & De Jager, J. (eds): *Geology of the Netherlands*. Royal Netherlands Academy of Arts and Sciences (Amsterdam): 151-171.

Wu, Q., Xu, H., & Zou, X. (2005). An effective method for 3D geological modelling with multi-source data integration. *Computers & Geosciences*, *31*(1), 35-43.

APPENDIX A: ECONOMIC CALCULATIONS

The gross revenue is the sum of the discounted yearly expenses and the discounted yearly income. The income is set to zero so that an assessment can be made on the LCOE, where the LCOE represents the minimum selling price per unit heat to balance the costs of the HT-ATES system. The discounted yearly expenses are calculated by Eq. 37. The E_{power} in Eq. 38 is set to zero, because there is no power generated from the heat that is recovered from the HT-ATES. The $Opex_{pump}$ are the costs for replacing the pumps every 5 years. The $OM_{var,heat}$ is the operation and maintenance cost per unit heat produced and is defined by the ratio of the electricity price of the pumps and the COP (Eq. 39). The fixed OM costs are an assumed percentage of the calculated Capex for the subsurface facilities (see equation Eq. 40).

$$Gross\ revenue = \ Discounted\ yearly\ expenses\ = Opex_{total} \cdot (1 + Inflation)^{t-1} \quad \text{Eq. 37}$$

$$\begin{aligned} Opex_{total} &= Opex_{heat} + Opex_{pump} \\ &= OM_{fixed,power}E_{power} + E_{prod,t}\left(t_{load}OM_{var,heat} + OM_{fixed,heat}\right) \\ &\quad + Opex_{pump} \end{aligned} \quad \text{Eq. 38}$$

$$OM_{var,heat} = \frac{Electricity\ price\ pumps}{COP} \quad \text{Eq. 39}$$

$$OM_{fixed,heat} = OM_{fixed,rate}(Capex_{heat} + Capex_{subsurface})/E_{prod,total} \quad \text{Eq. 40}$$

The total loan charges of the project are the sum of all interest and payment (see Eq. 44). Where t_{loan} in this study is taken to be equal to the lifetime of the HT-ATES system and the loan rate is set at 6% (see Table 5 in section 3.5.1). The loan share represents the part of the investment on which a loan has been taken (Eq. 44).

$$\begin{aligned} Total\ loan\ charges &= Interest + Payment \\ &= \frac{Loan\ rate}{(1 + Loan\ rate)^{t_{loan}} - 1} \cdot -Loan\ share \cdot (1 + Loan\ rate)^{t_{loan}} \end{aligned} \quad \text{Eq. 41}$$

$$Loanshare = \ Total\ investment \cdot (1 - Equityshare\ in\ investment) \quad \text{Eq. 42}$$

As has been mentioned before in section 3.5.3, the total investment is the sum of all Capex. Because the recovered heat of the HT-ATES is directly used for a district heating network and no power is generated, the $Capex_{power}$ is set at zero. The $Capex_{subsurface}$ is the capital expenditure for wells, stimulation and pumps (Eq. 43). Because stimulation is not needed to achieve favourable storage conditions, this is set at zero. The $Capex_{heat}$ is the product of the amount of heat produced and the heat surface installation costs per unit of heat production (Eq. 44).

$$Capex_{surface} = Number\ of\ wells \cdot Well\ costs \cdot depth + Pump\ investment \quad \text{Eq. 43}$$

$$Capex_{heat} = E_{prod} * Heat\ plant\ investment\ costs \quad \text{Eq. 44}$$

APPENDIX B: MAPS OF THE INDIVIDUAL SAND MEMBERS

B.1 REGIS V2.2 LCOE P50 AND P10 MAPS OF INDIVIDUAL LAYERS

Note that some layers are missing. This is because the model requirements of depth and COP caused some maps to show no data at all and are therefore not added to these figures.

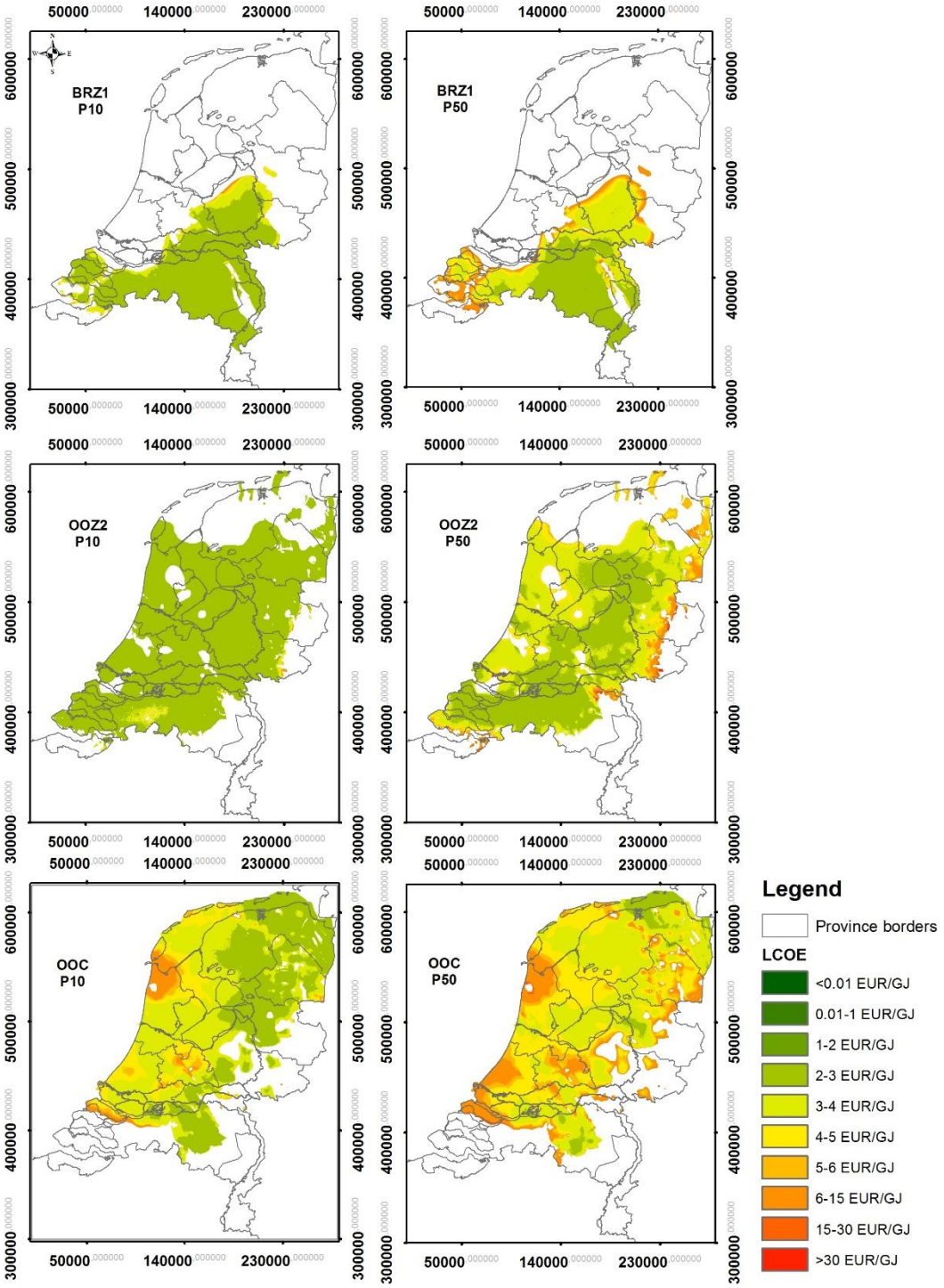

Fig. 25: These figures show the P50 and P10 LCOE maps of the top Breda sandstone layer(BRZ1), the Oosterhout sandstone layer (OOZ2) and the complex Oosterhout sandstone layer(OOC).

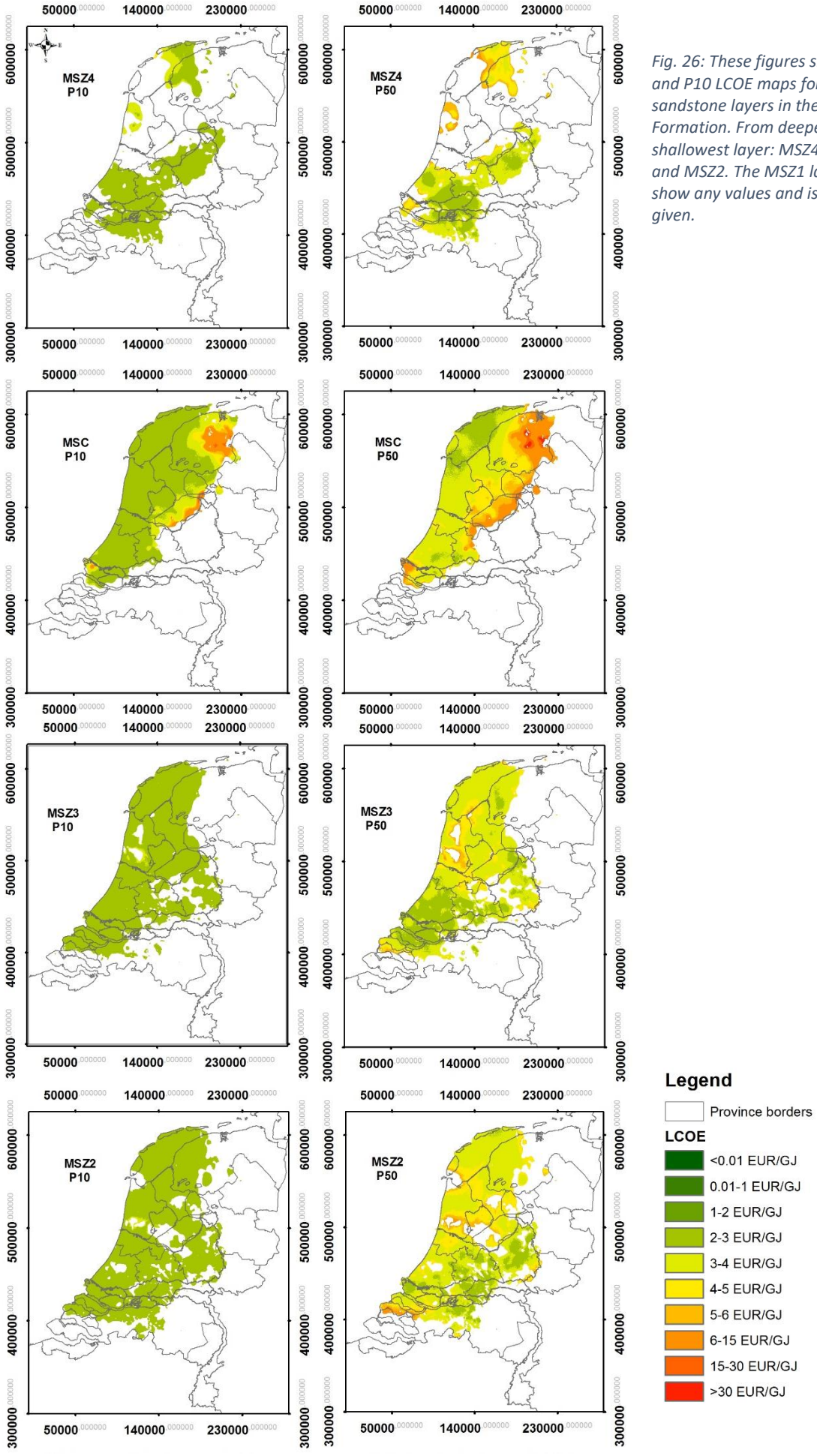

Fig. 26: These figures show the P50 and P10 LCOE maps for the individual sandstone layers in the Maassluis Formation. From deepest to shallowest layer: MSZ4, MSC, MSZ3 and MSZ2. The MSZ1 layer did not show any values and is therefore not given.

B.2 THERMOGIS LCOE P50 AND P10 MAPS FOR INDIVIDUAL LAYERS OF THE NORTH SEA GROUP

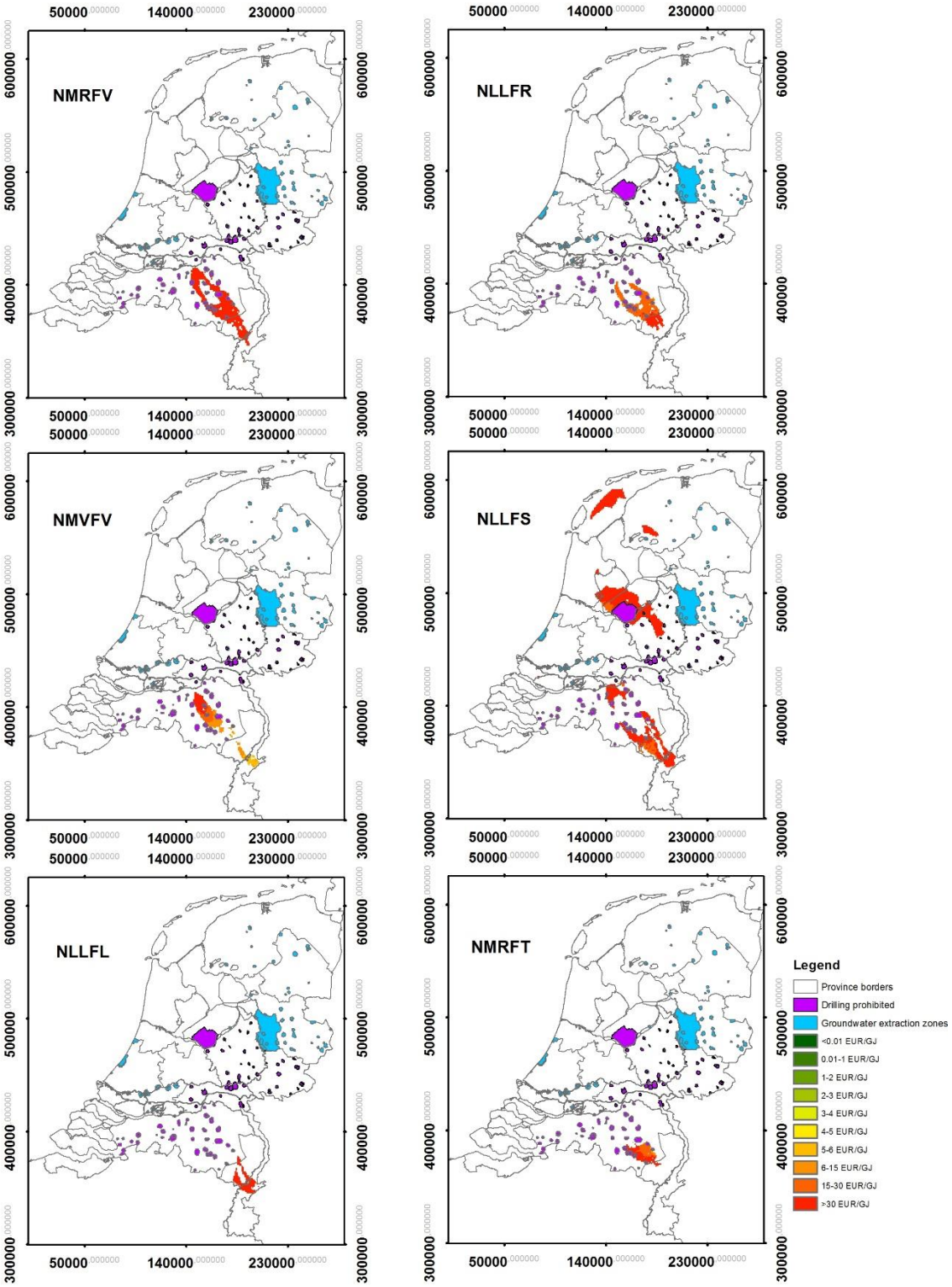

Fig. 27: These figure show the P50 LCOE maps of the following members in the middle and lower North Sea Group: the Voort member(NMVFV), the Steensel member(NMRFT), the Vessem member(NMRFV), the Reusel member (NLLFR), the Heers Sand member(NLLFS) and the Swalmen member(NLLFL. Note that the Basal Dongen Sand member is missing.

B.3 DEPTH MAPS OF THE STACKED LAYERS

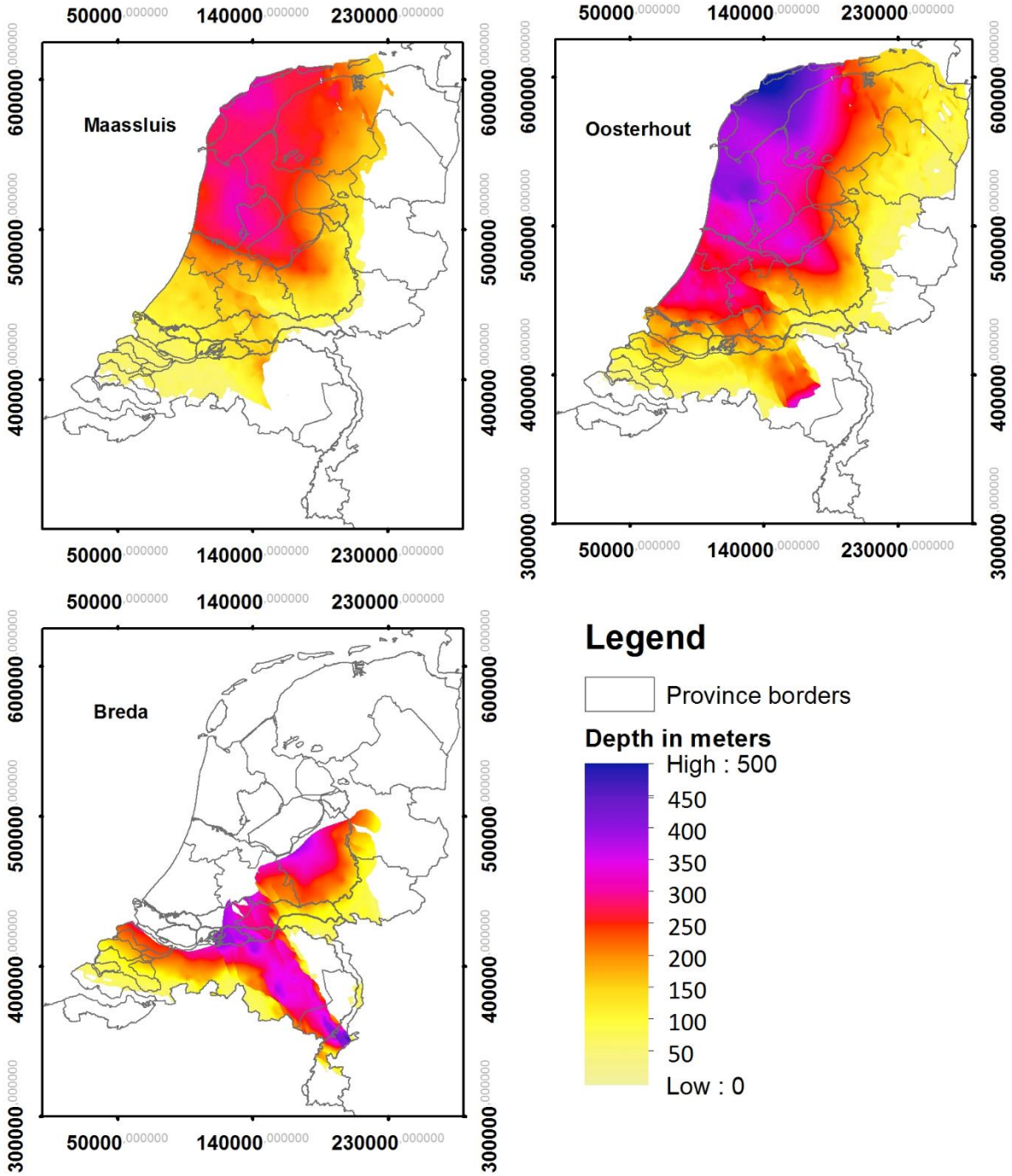

Fig. 28: These figures show the depths of the stacked Maassluis, Oosterhout and Breda formations.

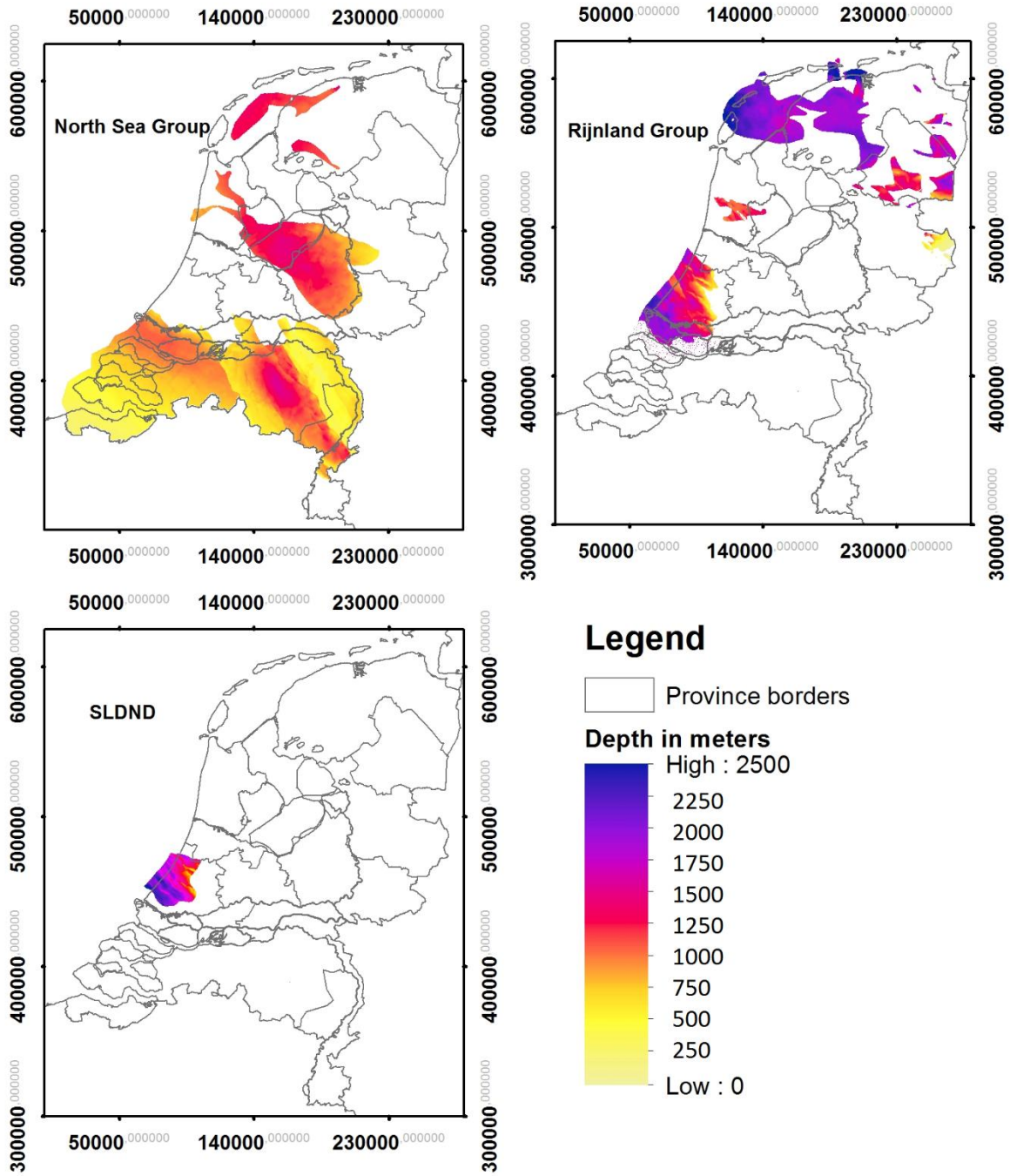

Fig. 29: These figures show the depth of the Delft Sandstone Member(SLDND) and the stacked Rijnland and Lower/Middle North Sea group reservoirs.

APPENDIX C: NOMENCLATURE FOR MODELS AND MAPS

This Appendix shows the figures 29 and 30.

Stratigraphic unit	Stratigraphic Group	ThermoGIS group code	Stratigraphic Formation	Stratigraphic Member	ThermoGIS member code
North Sea	Lower North Sea	N	Veldhoven	Voort	NMVFV
			Rupel	Steensel	NMRFT
				Vessem	NMRFV
			Dongen	Basal Dongen Sand	NLFFD
			Landen	Reusel	NLLFR
				Heers Sand	NLLFS
				Swalmen	NLLFL
				Swalmen, Heers Sand, Reusel, Basal Dongen Sand, Vessem, Steensel, Voort	N-Stacked
Lower Cretaceous	Rijnland	KN	Vlieland Sst.	Friesland Sst.	KNNSF
				Gildehaus Sst.	KNNSG
				Bentheim Sst.	KNNSP
				Rijswijk Sst., Berkel Sst., IJsselmonde Sst., De Lier Sst. stacked	KNWNB
Jurassic	Schieland	S	Nieuwerkerk	Delft Sst.	SLDND
				Jurassic & Lower Cretaceous	JK-Stacked
Triassic	Upper Germanic Triassic	TR	Röt	Röt Fringe Sst.	RNROF
	Lower Germanic Triassic		Hardegsen		RBMH
			Detfurth	Upper Detfurth Sst.	RBMDU
				Lower Detfurth Sst.	RBMDL
			Volpriehausen	Upper Volpriehausen Sst.	RBMVU
				Lower Volpriehausen Sst.	RBMVL
				Lower Volpriehausen Sst., Upper Volpriehausen Sst., Lower Detfurth Sst., Upper Detfurth Sst., Hardegsen Fm., Röt Fringe Sst.	TR-Stacked
Permian	Upper Rotliegend	RO	Slochteren	(Upper) Slochteren	ROSLU & ROSL
				Lower Slochteren	ROSLL
				(Upper) Slochteren and Lower Slochteren	RO-Stacked

Fig. 30: This figure shows the nomenclature that is used in ThermoGIS (Kramers & Pluymaekers, 2013).

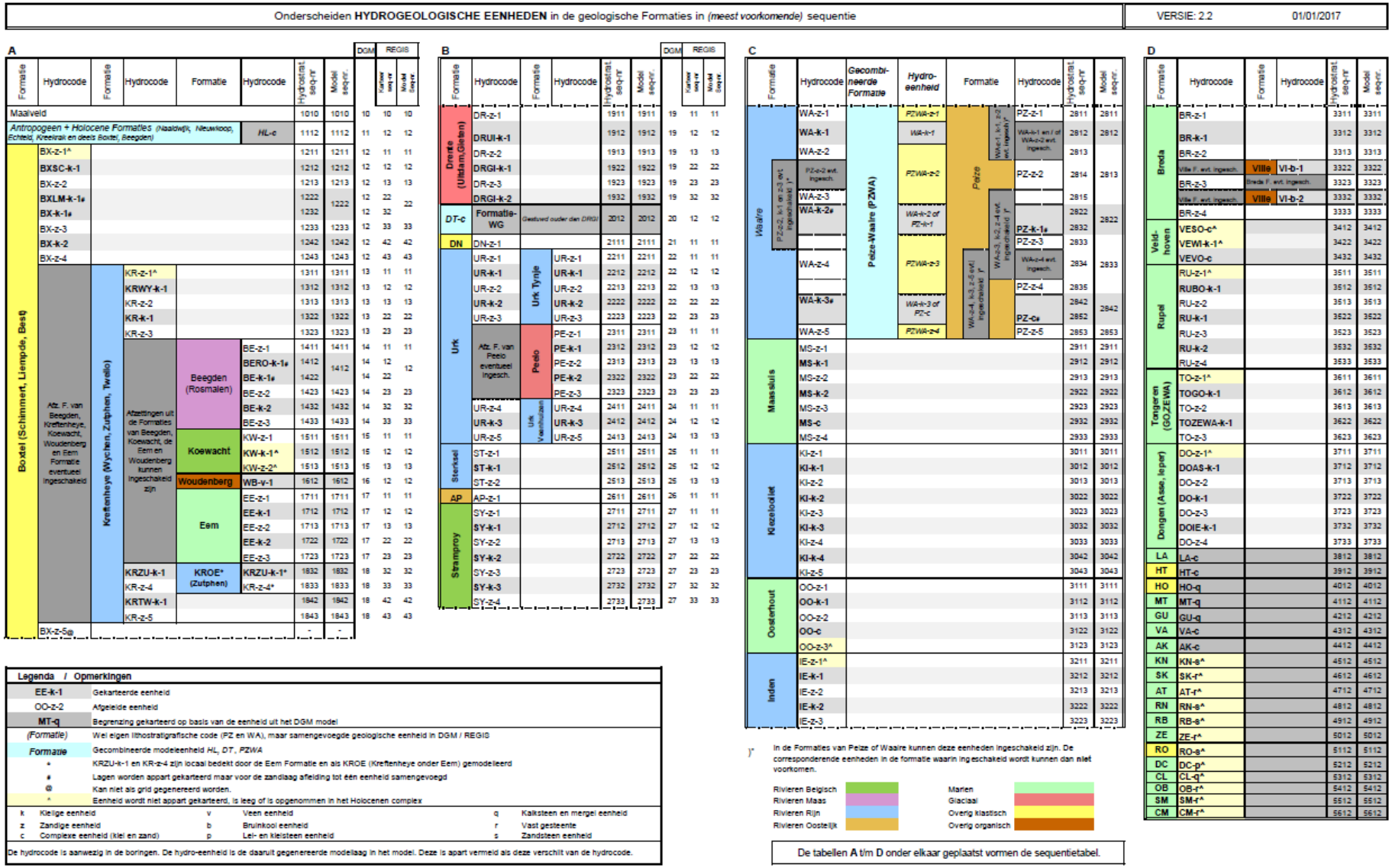

Fig. 31: This figure shows the table with the complete nomenclature used by REGIS v2.2

APPENDIX D: RELEVANT FIGURES AND MAPS

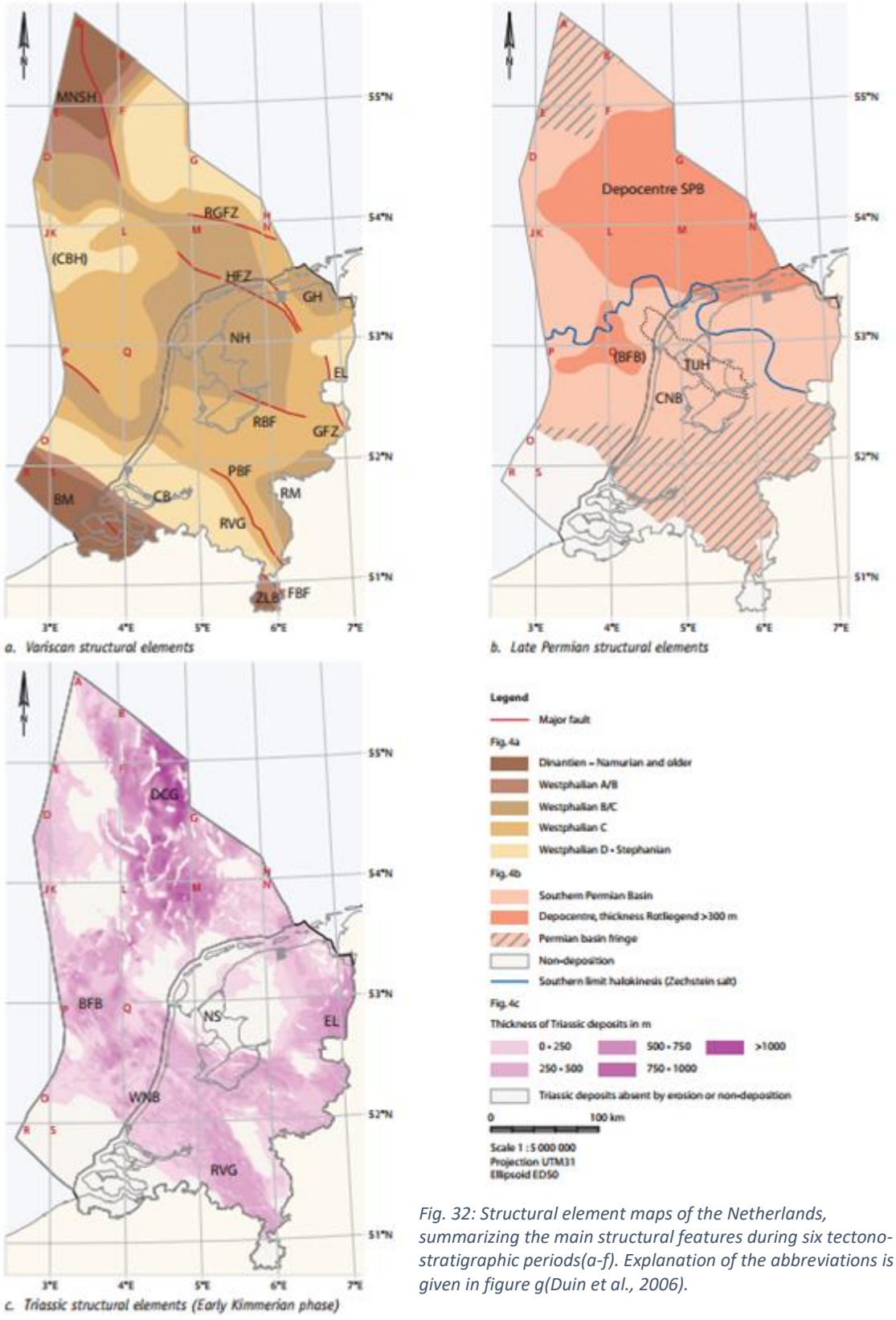

Fig. 32: Structural element maps of the Netherlands, summarizing the main structural features during six tectono-stratigraphic periods(a-f). Explanation of the abbreviations is given in figure g(Duin et al., 2006).

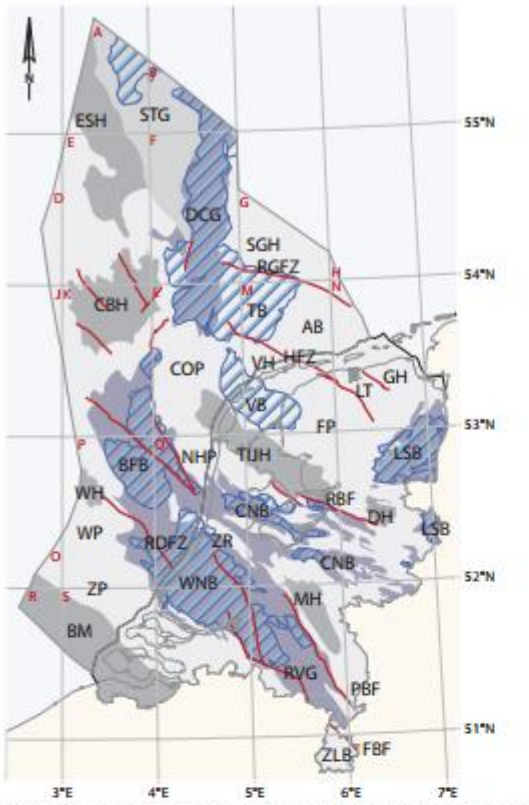

d. Late Jurassic - Early Cretaceous structural elements (Late Kimmerian phases)

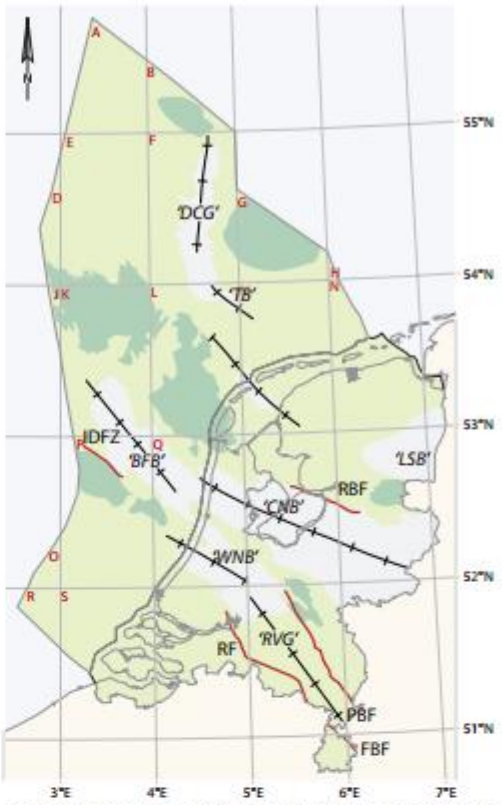

e. Late Cretaceous-Early Tertiary structural elements and basins (Subhercynian and Laramide phases)

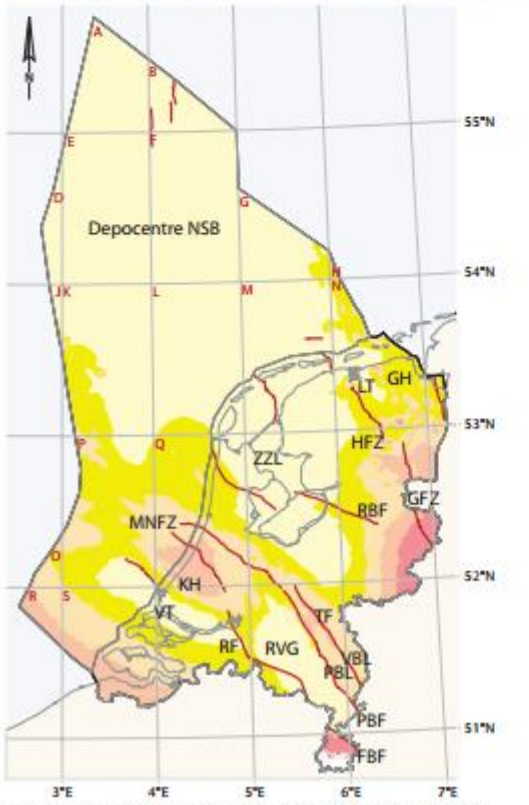

f. Cenozoic structural elements (Pyrenean and Savian phases)

Legend

Major fault

Fig. 4d

- Basin: Lower Jurassic present
- Basin: Upper Jurassic present
- Platform: Jurassic deposits absent
- Half graben: Lower Jurassic absent, Triassic partly
- High: Triassic absent, Rotliegend and/or Zechstein

Fig. 4e

- Thickness Chalk >1000 m
- Thickness Chalk <1000 m
- Subhercynian/Laramide inverted basins
- Tectonic axis

Fig. 4f

- Depth base North Sea Supergroup <250 m
- Depth base North Sea Supergroup 250 - 500 m
- Depth base North Sea Supergroup 500 - 750m
- Depth base North Sea Supergroup 750 - 1000 m
- Depth base North Sea Supergroup >1000 m

0 100 km

Scale 1 : 5 000 000
Projection UTM31
Ellipsoid ED50

Basins, platforms and highs	Abbreviation
Ameland Block	AB
Brabant Massif	BM
Broad Fourteens Basin	BFB
Campine Basin	CB
Central Netherlands Basin	CNB
Central Offshore Platform	COP
Cleaver Bank High	CBH
Dalfsen High	DH
Dutch Central Graben	DCG
Elbow Spit High	ESH
Ems Low	EL
Friesland Platform	FP
Groningen High	GH
Kijkduin High	KH
Lauwerszee Trough	LT
Lower Saxony Basin	LSB
Maasbommel High	MH
Mid North Sea High	MNSH
Netherlands High	NH
Netherlands Swell	NS
Noord-Holland Platform	NHP
North Sea Basin	NSB
Peel Block	PBL
Rhenish Massif	RM
Roer Valley Graben	RVG
Schill Grund High	SGH
Southern Permian Basin	SPB
Step Graben	STG
Terschelling Basin	TB
Texel-IJsselmeer High	TIJH
Venlo Block	VBL
Vlieland Basin	VB
Vlieland High	VH
Voorne Trough	VT
West Netherlands Basin	WNB
Winterton High	WH
Winterton Platform	WP
Zandvoort Ridge	ZR
Zeeland Platform	ZP
Zuiderzee Low	ZZL
Zuid-Limburg Block	ZLB
Faults and fault zones	
Feldbiss Fault	FBF
Gronau Fault Zone	GFZ
Hantum Fault Zone	HFZ
Indefatigable Fault Zone	IDFZ
Mid-Netherlands Fault Zone	MNFZ
Peel Boundary Fault	PBF
Raalte Boundary Fault	RBF
Rifgronden Fault Zone	RGFZ
Rijen Fault	RF
Rotterdam Fault Zone	RDFZ
Tegelen Fault	TF

g. List of abbreviations

APPENDIX E: P90 LCOE MAPS OF THE STACKED BR, OO AND MS FORMATIONS

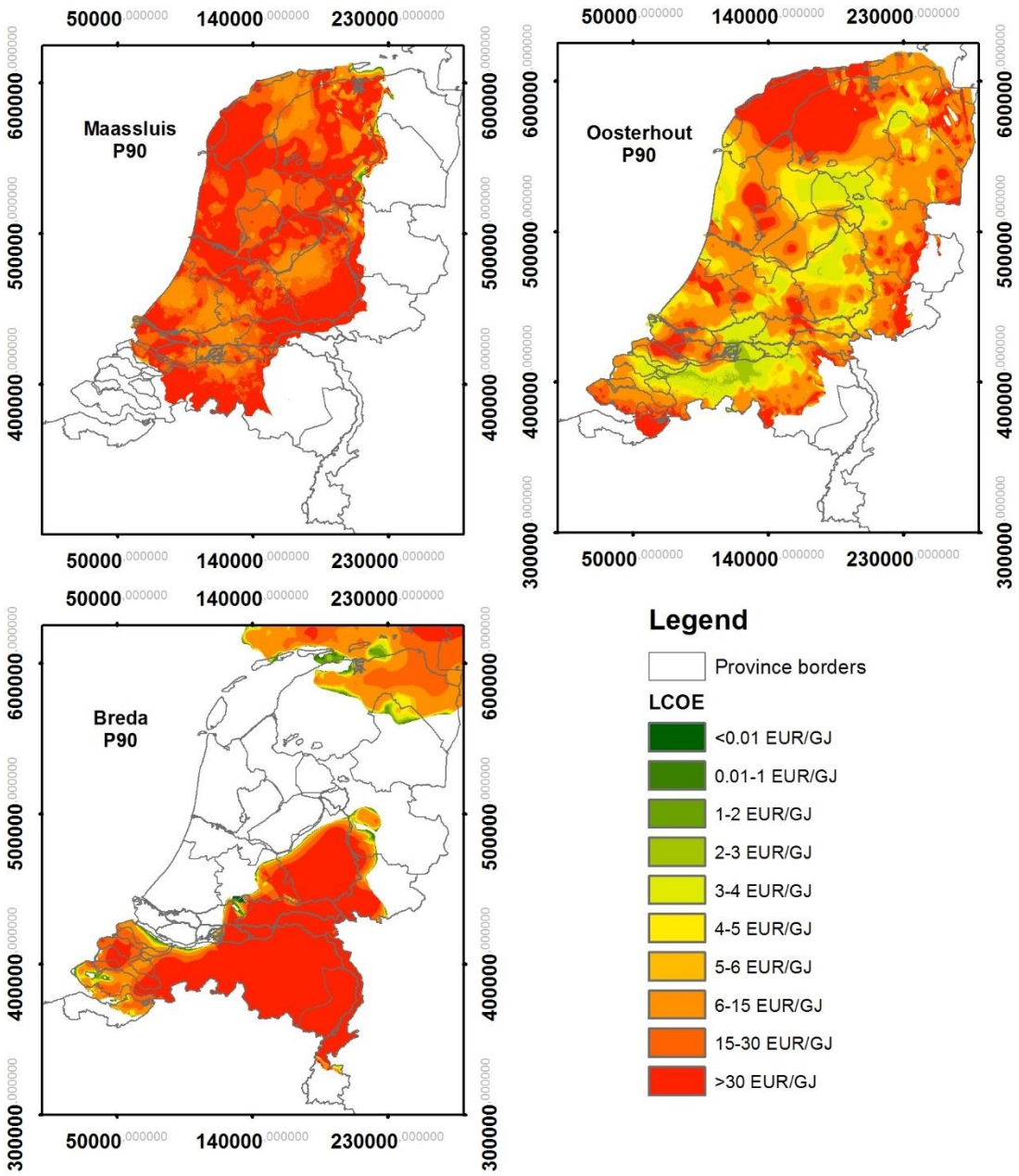

Fig. 33: These figures show the P90 LCOE maps of the stacked Maassluis, Oosterhout and Breda formations